
Politecnico di Torino

# Politecnico di Torino

Master of Science in Mechanical Engineering

December 2021

## Master thesis

## Spark plug geometry effects on flame propagation and displacement in an optical DISI engine

**Academic Supervisor:**

Prof. Federico Millo

**CNR - STEMS Supervisors:**

Dr. Simona Silvia Merola

Dr. Eng. Adrian Irimescu

**Candidate:**

Salvatore Pontillo

ID number s254962

# Abstract

In a historical moment in which the automotive sector is asked to improve its efficiency in terms of fuel economy and polluting emissions in order to mitigate the emerging climate crisis, the investigation and in-depth understanding of the flow phenomena and flame-fluid interactions occurring in the combustion process becomes fundamental. The basis of this analysis, aimed at the development of new combustion concepts of better efficiency, lies in the experimental activity that is providing over the years detailed studies of in-cylinder processes supported by the development of predictive CFD numerical models. The purpose of this thesis is to contribute to research by building up a wide thermodynamic and optical database concerning CCV phenomena, flame kernel formation and flame front propagation. The analysis was conducted on a Direct Injection Spark Ignition (DISI) engine featuring a Bowditch design, characterized by an extended piston combined with a quartz window mounted within the piston crown, that allowed optical access. The focus was on the effect of spark plug geometry and orientation under different engine operating conditions in terms of AFR, Spark Advance, engine load and speed. Two different types of spark plugs, respectively double-electrode J-type spark plug (in uniflow and crossflow orientations) and concentric-electrode spark plug, were examined by means of in-cylinder pressure measurements which allowed the analysis of thermodynamic parameters (IMEP, $COV_{IMEP}$, Pmax, $COV_{Pmax}$, NHRR, MFB, VFB etc..) combined with results from optical measurements. The optical analysis of images, acquired through cycle-resolved digital imaging using a high-speed camera, allowed a spatial characterisation of the combustion process through the study of kernel displacement and flame expansion speed. One of the main findings is the significant role in flame kernel development played by spark plug orientation and its influence on the direction of propagation of the flame front.

# Contents

# List of Figures

## Chapter 1 Figures



## Chapter 2 Figures



## Chapter 3 Figures

## Chapter 4 Figures

# List of Tables

# Acronyms and Symbols

## Acronyms

**AFR** Air Fuel Ratio

**AG** Air Guided

**AST** After Spark Time

**ATDC** After Top Dead Center

**BDC** Bottom Dead Center

**BTDC** Before Top Dead Center

**CAD** Crank Angle Degree

**CCV** Cycle-to-Cycle Variability

**CDM** Crank Degree Medium

**CFD** Computational Fluid Dynamics

**COV** Coefficient of Variation

**DISI** Direct Injection Spark Ignition

**DOI** Duration of Injection

**EV** Electric Vehicle

**EVO** Exhaust Valve Opening

**FCEV** Fuel Cell Electric Vehicle

**FID** Flame Ionization Detector

**GDI** Gasoline Direct Injection

**GHG** Greenhouse Gas

**HC** Hydrocarbons

**HEV** Hybrid Electric Vehicle

**HRR** Heat Release Rate

**ICE** Internal Combustion Engine

**IMEP** Indicated Mean Effective Pressure

**MFB** Mass Fraction Burned

**NDIR** Non-Dispersive Infrared

**PFI** Port Fuel Injection

**PHEV** Plug-in hybrid Electric Vehicle

| | |
|---|---|
| **PM** | Particulate Matter |
| **RON** | Research Octane Number |
| **SA** | Spark Advance |
| **SG** | Spray Guided |
| **SOI** | Start of Injection |
| **ST** | Spark Timing |
| **TDC** | Top Dead Center |
| **UEGO** | Universal Exhaust Gas Oxygen |
| **UHC** | Unburned Hydrocarbons |
| **VFB** | Volume Fraction Burned |
| **WG** | Wall Guided |
| **WOT** | Wide Open Throttle |
| **3-D** | 3-Dimensional |

## Symbols

| | |
|---|---|
| $a$ | Crank Radius |
| $Anf$ | Normalized Flame Area |
| $B$ | Bore |
| $CO$ | Carbon Monoxide |
| $CO_2$ | Carbon Dioxide |
| $CR$ | Compression Ratio |
| $d_{Feret}$ | Feret Maximum Diameter |
| $dP$ | In-cylinder Pressure Instantaneous Variation |
| $dV$ | In-cylinder Volume Instantaneous Variation |
| $Dx$ | x-axis Average Displacement |
| $Dy$ | y-axis Average Displacement |
| $H_{CV}$ | Hydrogen to Carbon Atomic Ratio |
| $l$ | Connecting Rod Length |
| $K$ | Water Gas Equilibrium Constant |
| $K_1$ | FID/NDIR Conversion Factor |

| | |
|---|---|
| $n$ | Engine Speed |
| $NO_x$ | Nitrogen Oxides |
| $O_{CV}$ | Oxygen to Carbon Atomic Ratio |
| $O_2$ | Molecular Oxygen |
| $p$ | In-cylinder Measured Pressure |
| $P_{intake}$ | Intake Pressure |
| $P_{max}$ | Average Maximum In-cylinder Pressure |
| $Q$ | Net Heat Release |
| $Q_{EVO}$ | Net Heat Release at the exhaust valve opening |
| $Q_k$ | Net Heat Release at current crank angle |
| $Q_{ST}$ | Net Heat Release at spark timing crank angle |
| $R$ | Kernel Displacement |
| $s$ | Crank-Piston Axis Distance |
| $V$ | Instantaneous In-cylinder Volume |
| $V_C$ | Cylinder Clearance Volume |
| $V_D$ | Displacement |
| $V_{Feret}$ | Flame Expansion Speed |
| $W_{c,i}$ | Indicated Work per Cycle |
| $\gamma$ | Specif Heats Ratio |
| $\lambda$ | Air Fuel Ratio |
| $\mu_{IMEP}$ | Average IMEP |
| $\rho_b$ | Burned Mixture Density |
| $\rho_u$ | Unburned Mixture Density |
| $\sigma_{IMEP}$ | IMEP Standard Deviation |
| $\theta$ | Crank Angle |

# Chapter 1 – Introduction

## 1.1 Background

Internal combustion engines (ICE) have dominated the transportation sector for more than a century and they currently consist of a main and fundamental part of road transport in Europe, the USA, and China. The growth of the road propulsion sector has, however, resulted in increasing negative impacts on the environment, as a result of emissions of hydrocarbons (HC), nitrogen oxides ($NO_x$), particulate matter (PM), carbon monoxide (CO), and carbon dioxide ($CO_2$), congestion and noise. For these reasons, beginning in 2016, European countries and cities began to make commitments to ban the future sale of ICE vehicles. Countries like France, Norway, and the UK have set dates for these bans [1]. Many of these new regulations are already being phased in, with full effect expected to be by 2030 or 2035. At the same time, governments are helping or rewarding citizens that convert to hybrid electric or fully electric vehicles. These assumptions lead to general ideas about the imminent "death" of ICE vehicles, but the reality turns out to be different. According to BP (British Petroleum) Statistical Review of World Energy 2021 [2], oil consumption fell by a record 9.1 million barrels per day (b/d) in 2020, or 9.3%, to its lowest level since 2011. However, as shown in figure 1.1, this energy resource holds the largest share of the global energy mix (31.2%), followed by coal (27.2%).

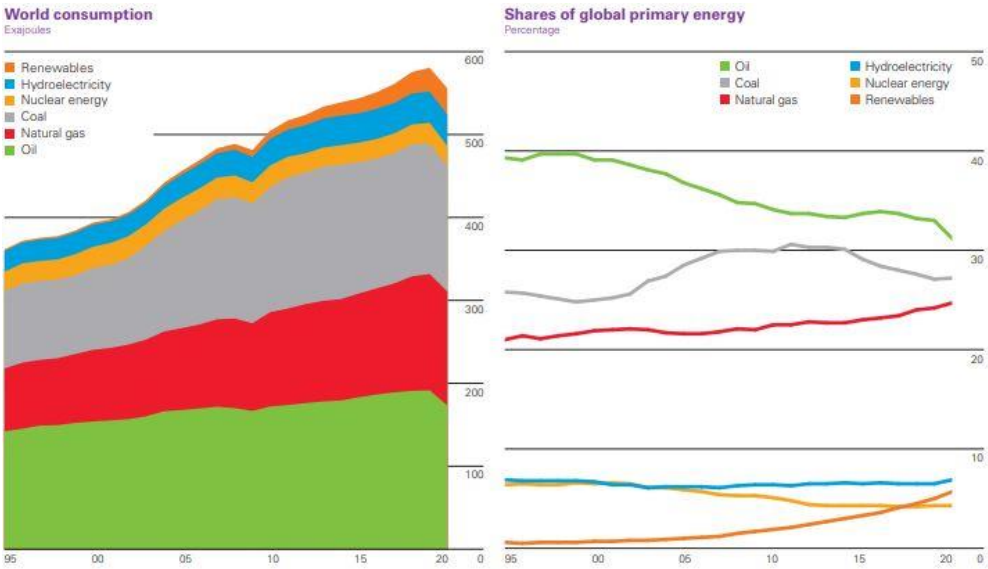


*Figure 1.1, World energy consumption by source (1995-2020) [2]*

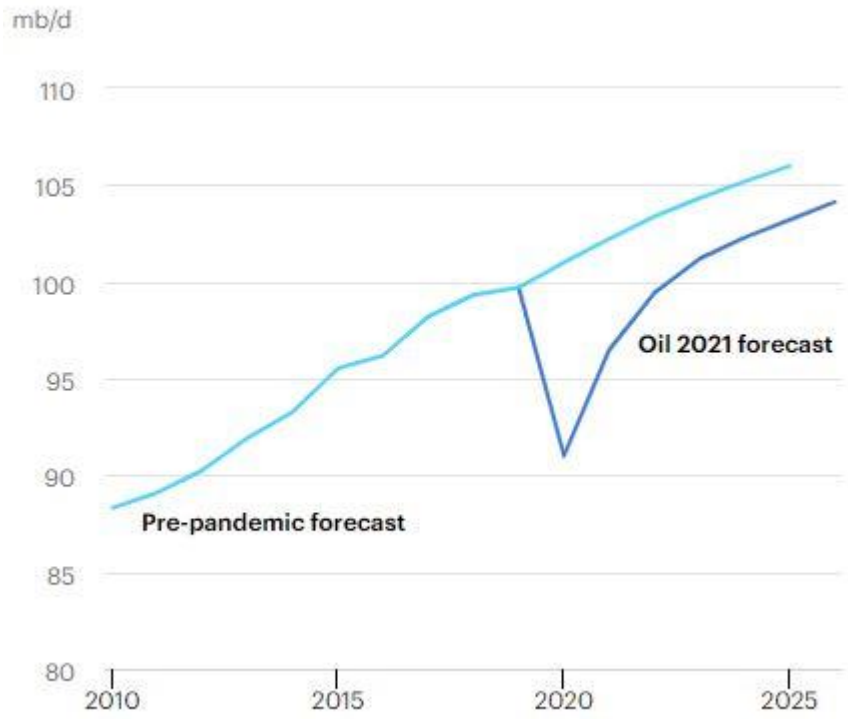


*Figure 1.2, Oil demand forecast (2010-2026) [3]*

Moreover, despite the negative influence that the COVID-19 crisis has had on the oil demand forecasts, as can be seen from figure 1.2, an increase in demand is still expected for the next few years. Currently, there are around 1.2 billion light-duty vehicles and 380 million heavy-duty vehicles, and the daily demand for liquid fuels exceeds 11 billion liters. Global powertrain forecasts describe a reduction in ICE vehicles sales from 88.1% in 2020 to 45.5% in 2030. The projected percentage will be, following the data provided, characterized by 39.7% of gasoline engine vehicles. In contrast, the electric (EV), hybrid (HEV), plug-in hybrid (PHEV), and fuel cell electric (FCEV) vehicles industry will increase sales by up to 54.5% [4]. Despite this negative trend, the predominant role that internal combustion engines will continue to play in the coming decades can be noted, especially regarding the gasoline engines also used in hybrid electric architectures.

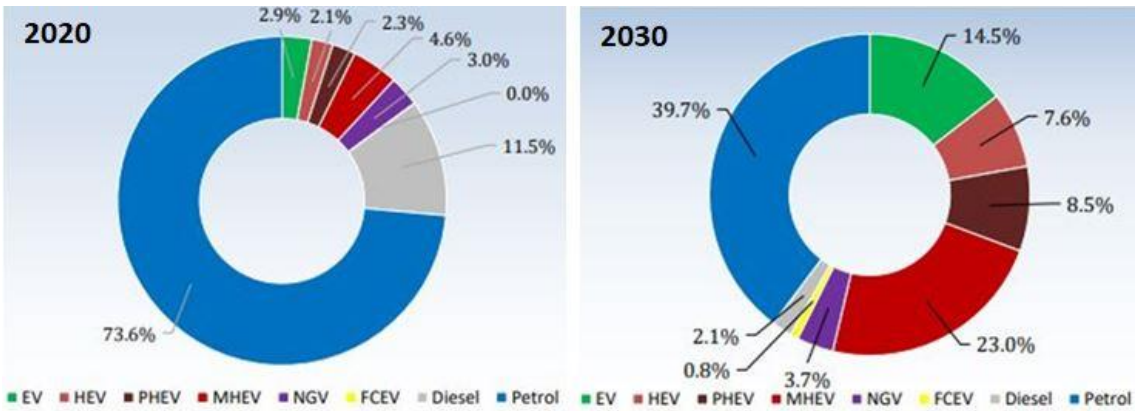


*Figure 1.3, Global automotive forecast by type 2020-2030 (%sales) [4]*

Another critical advantage of internal combustion engines is the higher energy density of the fuels compared to lithium-ion batteries. Gasoline and diesel contain about 80 times

more energy per unit of weight than the best lithium-ion batteries. Even assuming that EVs are twice as efficient as ICE automobiles, the energy density of gasoline and diesel remains still 40 times better than that of batteries. Reasoning in terms of GHG emissions characteristic of internal combustion engines, the stringent standards imposed by European regulations have allowed a reduction of 20% since 1990, as can be seen from the following figure 1.5 taken from statistical studies of the European Environment Agency.

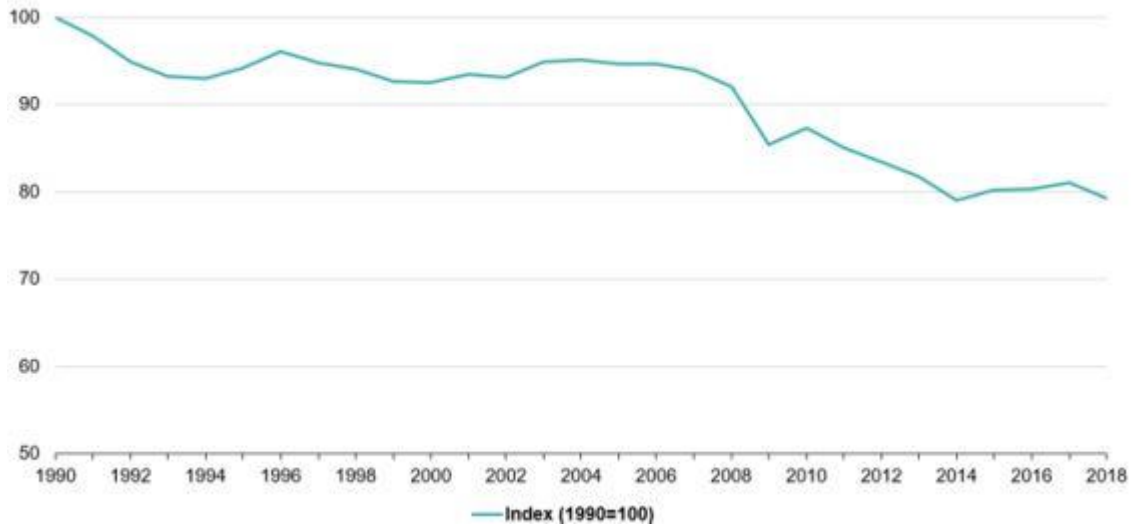


*Figure 1.4, GHG emissions evolution for EU (1990-2018) [5]*

From these advances in terms of emissions, the importance of the researches conducted on ICE's technologies can be noted, under which it has been possible to achieve in the last three decades an evolution and improvement in the engine's efficiency and related after-treatment systems. It is also necessary to specify that the conversion to fully electric road transport would only involve the delocalization of emissions, not their complete elimination in an ideal concept of "zero emissions level". The spread of EVs would increase the worldwide electricity demand, currently compensated, as seen, by an industrial sector highly dependent on fossil fuels. In addition to these considerations, there are disadvantages related to higher selling prices for electric vehicles rather than ICE vehicles (with the same dimension, neglecting the battery autonomy and consequently limited range) due to increasing demands for materials used in battery production. This can be seen in figure 1.5, showing projected metals demand growth by 2030. According to the above considerations, the fundamental role that internal combustion engines have played in the last century and will continue to play in the near future remains unquestionable. The progress in terms of emissions, efficiency and therefore consumption is the result of the introduction of advanced technologies resulting from uninterrupted research activity. One of the above-mentioned technological innovations that is recently experiencing its market diffusion is the direct injection spark ignition (DISI) or gasoline direct injection (GDI) engine.

| Metal | Expected Demand Growth Increase to 2030 in the EV Industry |
|---|---|
| Nickel | 14x |
| Aluminum | 14x |
| Phosphorus | 13x |
| Iron | 13x |
| Copper | 10x |
| Graphite | 10x |
| Lithium | 9x |
| Cobalt | 3x |
| Manganese | 3x |

*Figure 1.5, Expected demand growth increase to 2030 in the EV industry [6]*

DISI engine has been pursued for several decades as an alternative to premixed SI engine. The earliest systems include the TCCS (Texaco controlled combustion system developed in the 1950s) with a high-pressure diesel-like injection system and the Ford PROCO (programmed combustion engineered in the 1970s) with a low-pressure-injection system (~20 bar). Both systems, however, produced high $NO_x$ and HC emissions at light load, and engine output was soot limited [7]. The techologial advances in fuel injection equipment have generated a renewed worldwide interest in the DISI engine, with the first commercially avaible DISI powered vehicle made by Mitsubishi in 1996 and just over 45% of model year 2015 light-duty vehicles in US equipped with gasoline direct injection [8]. In a DISI engine, the fuel is directly injected into the combustion chamber, near the end of the compression stroke, to form a stratified air/fuel mixture for ultra-lean combustion and to reduce the engine pumping loss at part load. Furthermore, these systems employ a higher compression ratio to provide greater thermal efficiency. To achieve the proper mixture in the combustion chamber of a GDI engine, various injection and airflow strategies have been implemented, such as the multiple-injection and spray-guided techniques. The advantages of direct injection engines in the homogeneous operation mode are likewise noticed. The volumetric efficiency can in fact be increased injecting during the intake phase directrly into the combustion chamber (during the vaporization phase the overall mixture temperature decreases); this involves the introduction of a higher quantity of air into the engine from which derives an increased power output. In addition, various emission after-treatment devices, such as a gasoline particulate filter and lean $NO_x$ trap have been used to reduce exhaust emissions. Major injector manufacturers recently embarked on the development of a piezo-outwardly type injector and a multi-hole type injector to improve engine performance and reduce exhaust emissions. Additionally, researches are actively pursuing alternative fuels, such as bioethanol and biobutanol, eco-friendly alcohol fuels, for use in GDI engines [9], [10].

In the following experimental study, performed on an optically accessible single-cylinder DISI engine, the results obtained from laboratory tests concerning different levels of Air-Fuel ratio (AFR), Spark Advance (SA), load ($P_{intake}$) and engine speed (n) are reported. The analysis includes the employment of a double electrode spark plug, kept in the Uniflow and Crossflow configuration, and a concentric electrode spark plug. In the first geometry the ground electrodes are in line with the intake air flow (respectively parallel and opposite to the tumble motion), while in the Crossflow configuration the spark plug is rotated by 90 angle degrees with respect to the previous orientation. In such a context, the aim of this work is the study of the effect on the flame kernel formation and flame front propagation for the aforementioned operative conditions.

## 1.2 Optical Accessible Engine History and Evolution

Optically accessible engines are nowadays an indispensable tool in the investigation of the combustion process in internal combustion engines through optical and laser optical methods. These methods can be indeed applied to analyze the mixing formation, injection, combustion, and emission formation in situ for a better understanding of the combustion process [11]. Probably the earliest example of the use of an optical engine to better understand flow and mixing phenomena in reciprocating engines was provided by Nicolaus Otto himself in 1872. Since then, visualizing the mixing process in the cylinder and the resulting combustion process has been essential to deepening our understanding of how these devices work and to gain insights into how efficiency and emissions can be improved [12]. With the development and parallel diffusion of the first simulation software, it has been therefore possible to use both research methodologies in the comparison between experimental and simulated data regarding phenomena such as kernel growth, flame front propagation and burning turbulent velocity. A virtuous circle has been triggered for research about the evaluation of in-cylinder phenomena, which over the years has acquired greater efficiency and accuracy thanks to the boost coming from experimental and numerical methodologies combined in a mutual improvement.

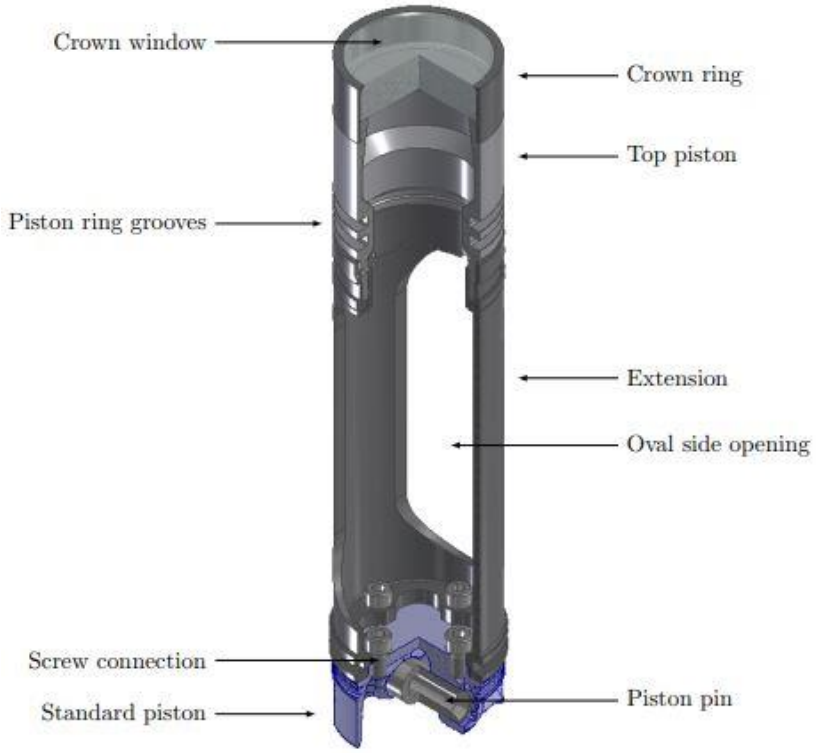


*Figure 1.6, Bowditch-piston 3/4 isometric section view*

The current optical engines available are often based upon Bowditch-piston design (figure 1.6) introduced in 1958, consisting of an elongated piston with an extension bolted on top of a standard piston that provides optical access from below the combustion chamber

through a transparent window in the piston roof. A stationary 45° tilted mirror is inserted into an oval side opening of the piston extension, which transfer the image to the side of the engine. The extended piston is usually combined with a transparent liner or a transparent segment of the liner that provides optical access from the side of the combustion chamber. The transparent components are often made of synthetic quartz glass or clear sapphire due to their abilities to transfer light in an relevant spectrum, their mechanical properties and heat resistance. The quartz is attached on the piston using a high-temperature epoxy resin adhesive which guarantees a strong adherence to the metal parts and a high resistance to the high thermal stress due to the combustion process [13]. In fact the major problem related to Bowditch-piston concerns the excessive oil leakage past the valve guides and from the crankcase, that can eventually lead to quartz fouling accordingly degrading the quality of visualization of the combustion chamber. This issue can be solved using specific valve stem seals and special ring-pack. Obviously, each optically accessible engine of this kind has a unique design due to specific modifications that unfortunately result in difficulties in comparing experimental results.

## 1.3 Cycle to Cycle Variability and Flame Kernel Growth

Combustion stability is a prerequisite for more efficient spark ignition (SI) engine operation and reduced engine-out emissions. Indeed, the cycle-to-cycle variations (CCV) negatively affect output engine power; it is estimated that output power and fuel consumption reduction can be improved by about 10% with a radical decrease of CCV [14]. This phenomenon becomes predominant for lean air-fuel mixtures [15] and a significant increase in vibration and noise can also be observed. However, the reduction of cycle-to-cycle variations by design or control measures is challenging due to the complex multi-physics and multi-scale nature of the in-cylinder processes, which are not completely understood [16]. The stochastic nature of cycle-to-cycle variability results from several causes such as the turbulence related to the intake flow, Air-Fuel Ratio (AFR), the recirculated quantity of exhaust gas, spark plug orientation and many others of minor entity. Furthermore the available information coming from several studies and regarding the causes of CCV are relatively limited and difficult to compare due to the differences between the optical research engines used or varying methodology. The key factors that determine the levels of CCV can be identified by applying a 0D/1D modelling approach [17]. The main influence is related to the in-cylinder turbulence which results in the mixture flow variation across the combustion chamber; CCV can be actually reduced by up to 66% through the optimization of tumble and swirl motions. The second most important factor is linked to the equivalence ratio and thus to the mixture composition variability in whose absence the CCV may be reduced by up to 13.7%. The latter cause is related to the flow angle whose impact on the CCV is reduced to 3.8%. The above factors are moreover closely connected to the kernel growth responsible of more than 50% of the CCV [18,19]. Many research studies have investigated the influence of spark plug orientation instead [20,21]. Wang et al. analysed three spark plug orientation with two different electrode designs (Double Fine Wire and Oval-J designs) and their effects on the kernel growth and consequently the CCV in an optically accessible single-cylinder engine. Results has been divided in two groups in which initial flame kernels were respectively located to the exhaust side (group A) and to the intake side (group B). In particular, the results of group A showed that for the counter-flow configuration the flame kernel propagation is slower for each spark plug design while the crossflow is the “faster” configuration. The effect on the flame kernel displacement and dimension of the arc between the two electrodes were moreover examined by Schirru et al. for many operative conditions including the variation of engine speed and AFR. In this study, a double electrode spark plug was fitted in the crossflow orientation into an optically accessible engine. It was observed that during a normal cycle the flow field between the electrodes tends to transport the arc deforming it. Because of that, the kernel growth phase takes place away from the electrodes and the flame propagates with a preferential

direction dictated by the flow field. The results in terms of IMEP and $COV_{IMEP}$ obtained for the aforementioned configuration were compared with those related to a default orientation (figure 1.7). Varying AFR, the crossflow orientation showed higher IMEP values and lower $COV_{IMEP}$ compared to the default one; however the influence of the spark plug orientation seemed to be less important compared to the other operative condition effect. Among the main conclusions, in the papers [21,22], the authors noted the possibility to use leaner mixture for low engine speed which featured higher stability of the combustion process. Another evidence is given by the analysis of linear correlations between mean piston speed and $COV_{IMEP}$ that revealed a determining role of the chemical kinetics part in this sense.

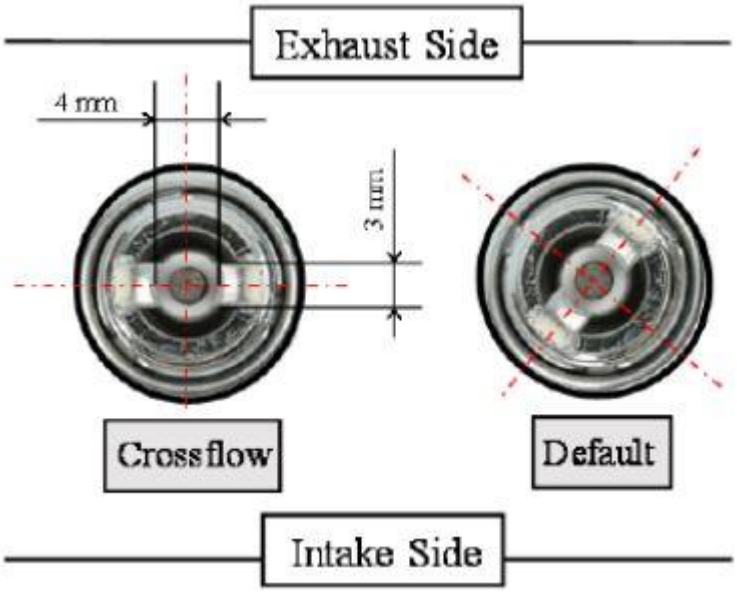


*Figure 1.7, Double J-type electrode spark plug [21]*

The relationship between cycle-to-cycle variations and Air-Fuel Ratio was deepened in [23] using a crank angle resolved method. A strong correlation has been demonstrated between the IMEP and the first phases of combustion process (the range examined was up to 5% of MFB), practically when the flame kernel is taking form. In view of these considerations, it is clear that further study of the phenomena influencing cyclical variability is needed to increase the efficiency of the combusiton process. In particular, the present experimental work, similar in purpose to the studies performed in [21], aims to the enrichment and comparison of data already obtained in this specific research field.

## 1.4 Homogeneous Charge Injection Strategy

In a spark-ignition (SI) engine the fuel and air are mixed together in the intake system (PFI) or in the combustion chamber (GDI), where mixing with residual gas takes place, and then compressed. Following inflammation, a turbulent flame develops, propagates through this essentially premixed fuel, air, burned gas mixture until it reaches the combustion chamber walls, and then extinguishes [15]. The combustion process can therefore be summarised as a pre-mixed turbulent combustion with a heat release rate (HRR) strongly related to the turbulent burning velocity; the latter is a function of the laminar burning velocity which in turn depends on the AFR, as seen in figure 1.8.

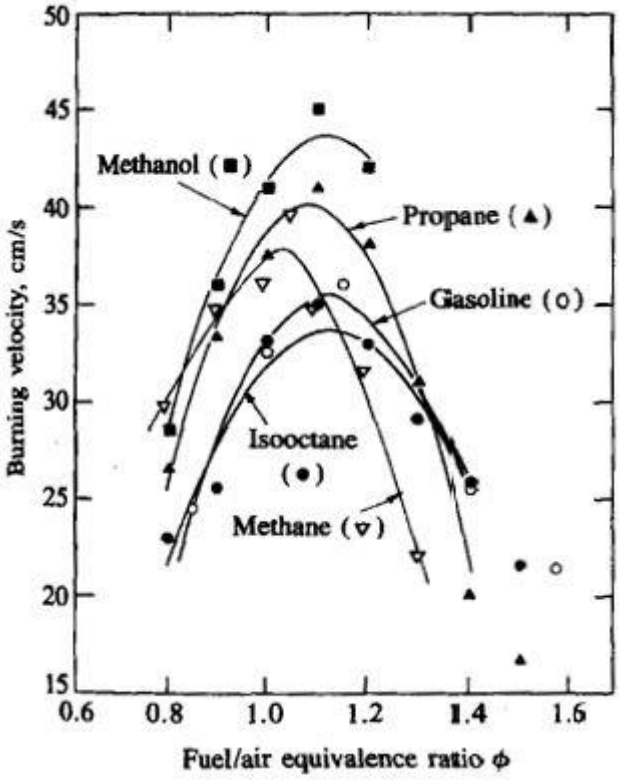


*Figure 1.8, Laminar burning velocity for several fuels as function of equivalence ratio [15]*

Various injection strategies have been implemented over the years, especially since the development of GDI technology; this research work will be focused on the homogeneous charge injection strategy. To obtain a homogeneous mixture in a SI engine, it is necessary to start injection well in advance of reaching firing top dead centre (TDC) to give the injected fuel time to completely breakup, vaporise and mix with the air flow coming from the intake manifold [10]. High speed and turbulence are ensured by a fuel delivery that takes place during the intake stroke. This injection strategy is actually used for mid or high load operation due to emission issues related to the stratified charge injection strategy which could promote the formation of UHC in overmized zones and PM in undermixed ones [24]. The disadvantage of this approach is a long fuel injection duration, required for high load operation, that may cause over-penetration of the fuel, thus the impingement on the piston crown [25]. Delaying the injection event until near bottom dead centre (BDC) will reduce

wall wetting, with the trade-off of reducing mixture formation time [26]. However, since the possibility of using lean air-fuel mixtures is limited, the homogeneous strategy does not seem to have margins of improvement in terms of fuel consumption. In spite of the above-mentioned drawbacks, current research is pushing towards optimising this operating conditions by exploiting the advantage of reduced charge temperature during the vaporisation phase and the possibility of splitting the injection [10]. The effect of split and delayed injection on the cycle-to-cycle variation, PM, CO and UHC emissions has been accurately analysed in [25,27] maintaining a single injection event per cycle approach. In this study, a homogenous mixture was achived at the spark timing angle setting the start of injection at 300 CAD before top dead center (BTDC).

## 1.5 DISI Mixture Formation and Control

Three different combustion systems are used to form an ignitable mixture near spark plug at the instant ignition in a DISI engine. These are the spray-guided (SG), wall-guided (WG) and air-guided (AG) combustion systems, shown in figure 1.9. The distinction between the different concepts is the used method with which the fuel spray is transported near the spark plug.

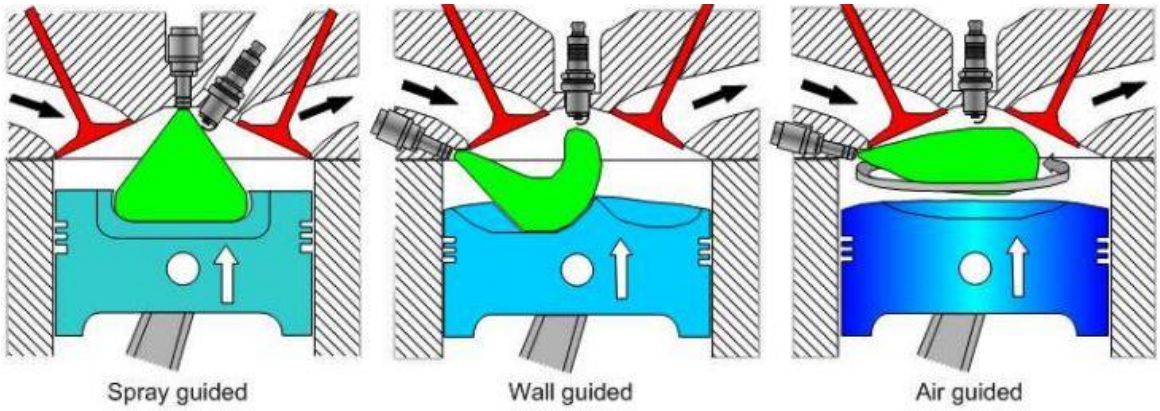


*Figure 1.9, Different types of DISI combustion system [28]*

In the SG technique fuel is injected near spark plug where it also evaporates. The spray-guided combustion system theoretically has the highest efficiency thanks to a series of advantages: reduced wall wetting, less sensitive to in-cylinder air flow, less sensitive to cylinder to cylinder variation and reduced raw HC emissions. Reported disadvantages are spark plug reliability (fouling) and poor robustness (high sensitivity to variation in ignition and injection timing); however the spray-guided injection achieves better combustion and fuel efficiency (especially adopting the stratified charge injection strategy) than conventional wall-guided direct injection systems. In this latter combustion system, the fuel is indeed transported to the spark plug by using a specially shaped piston surface; this may involve the incomplete vaporisation of injected fuel on the piston surface resulting in increased HC and CO emissions, and fuel consumption. For these reasons, the WG combustion system is generally used in combination with the air-guided one, as both feature injectors located remotely to the spark plug. In the AG combustion system the fuel is injected into air flow, which moves the fuel spray near the spark plug; the air flow is obtained by inlet ports with special shape and air speed is controlled with air baffles in the manifold. In this technique, fuel does not wet the piston and cylinder. Therefore a combined WG-AG combustion system is less sensitive against the cyclic variations of air flow and less affected by impingement, as well in the stratified and in the homogenous mode [28]. According to these considerations, the optically accessible engine used for this work features a wall-guided combustion system, representative of a large segment of the automotive engine design.

## 1.6 Motivation and Research Goal

Nowadays numerical simulation is taking a significant role in the development of new powertrains; hence the importance of collecting and analyzing experimental data useful in the implementation and validation of CFD models. The current thesis is therefore motivated by the need for in-depth analysis and knowledge of in-cylinder processes, with particular attention to the kernel formation and flame front propagation. The main objective was to characterise the possible influence that spark plug geometry and orientation could have on the aforementioned phenomena in terms of flow, thermal and chemical engineering. The numerous tests carried out under different engine operating conditions in an optically accessible GDI engine have also allowed a large database to be built up, enabling a comparison of results with previously carried out studies characterised by the same main target [21,22]. Moreover, thermodynamic and optical data collected will be fundamental for the numerical modelling and simulation of the combustion process aimed, in particular in this present work, at improving the process stability in lean conditions with the evaluation of cycle-to-cycle variability and related parameters, with a view to achieving increased engine performances and better fuel economy.

# Chapter 2 – Experimental Setup

## 2.1 Engine System Setup

The present research work is based on the measurements carried out in one of the laboratories of the "Istituto di Scienze e Tecnologie per l'Energia e la Mobilità Sostenibili" (STEMS-CNR) in Naples, on an optically accessible DISI single-cylinder four-stroke engine. The engine head, originally built for a 1.4 litres Fiat 4-Cylinder turbo-charged unit in line, was appropriately modified for the optical investigations. The system is equipped with four-valve pent-roof head, while the crankcase features two balancing shafts which significantly reduce vibrations normally occurring for a common single-cylinder engine. A Bowditch extended piston design, in combination with the quartz section on the piston top, allows the combustion chamber to be visible through the piston crown. The engine specifications and the valves timing setup are disclosed in Table 2.1, while figure 2.1 shows the schematic configuration [21]. The experimental apparatus is equipped with two balancing shafts in the crankcase which significantly reduces vibrations, normally occurring for a common single-cylinder engine.

| | |
|---|---|
| **Displacement** | 399 $cm^3$ |
| **Stroke** | 81.3 mm |
| **Bore** | 79 mm |
| **Connecting Rod** | 143 mm |
| **Compression Ratio** | 10:1 |
| **Number of Valves** | 4 |
| **Exhaust Valves Open** | 153 CAD ATDC |
| **Exhaust Valves Close** | 360 CAD ATDC |
| **Intake Valves Open** | 363 CAD BTDC |
| **Intake Valves Close** | 144 CAD BTDC |
| **Fuel Injection System** | DI-WG |
| **Start of Injection** | 300 CAD BTDC |

*Table 2.1, Engine specifications*

The engine speed was set by regulating the electrical motor speed with a feedback control loop capable of switching between motor – generator regimes. This was also maintained constant, at different load levels, with an error of ±20 rpm by exploiting a 50 kW dynamometer. Synchronization of various control triggers for ignition, injection and camera recording start was achieved using the optical encoder mounted on the crankshaft as an external clock connected to an AVL Engine Timing Unit (AVL, Graz, Austria).

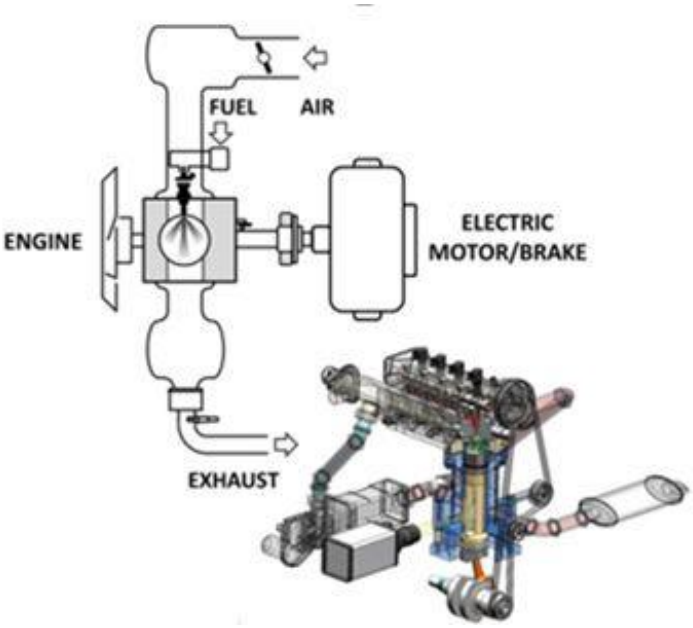


*Figure 2.1, Schematic representation of the experimental setup [21]*

This pulse generator (figure 2.2) synchronizes the encoder with the engine cycle, using the Trigger and CDM (Crank Degree Medium) from the encoder itself as input command for this operation. They respectively indicate the TDC position and the pulses for each angle. The injection system is controlled by an additional electronic control unit (figure 2.3), where the start and duration of the injection event are fixed using the digital input signal coming from the ETU. Apart from the output signal that drives the injector, this control unit also maintains a constant injection pressure (100 bar) monitored using a piezoelectric transducer flash-installed at one of the rail's extremities.


*Figure 2.2, AVL ETU pulse generator*


*Figure 2.3, Injection control unit*

The common-rail pipeline for the injection system was modified to enable only one of the four injectors and subsequently tested to ensure that there were no leaks through the seals. A six-hole injector manufactured by Magneti Marelli (diameter of holes of 0.140 mm and solenoid actuation, figure 2.4) is fitted between the two intake valves, thus ensuring fuel delivery and mixture formation according to the wall-guided mode. The fuel used is a common gasoline with a RON (Research Octane Number) of 95 [29].

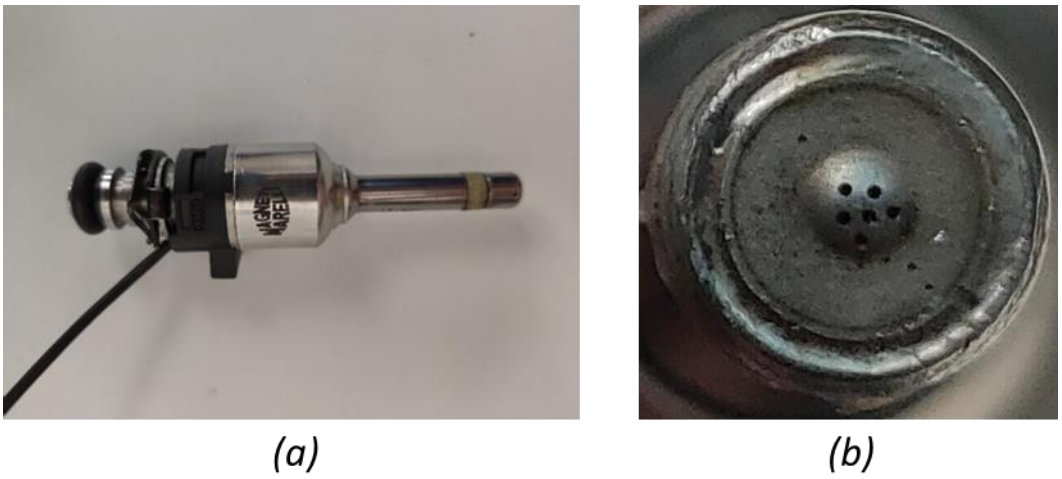


*Figure 2.4, (a) Magneti Marelli Injector, (b) Injector nozzle*

The fuel supply system features a continuous-delivery system; therefore, it includes a low-pressure pump which feeds the high-pressure pump. Regarding the Start of Injection (SOI), for all the cases the value reported in the Table 2.1 was used to guarantee the condition of homogeneous charge. This latter has been verified by monitoring Air-Fuel Ratio with two different devices. The first one consist of a UEGO (Universal Exhaust Gas Oxygen) sensor with an accuracy of $\pm 1\%$ and a measurement range of 0.55-1.2 $\lambda$, fitted close to the exhaust manifold. The second device is located further down the exhaust line; it is an AVL DITEST GAS 4000, also needed to study the composition of the combustion gas. The AVL device is not influenced by the exhaust backpressure (mainly due to the fact that it features a sampling pump, [30]) and it measures the Air-Fuel Ratio by applying the Brettschneider's equation [31];

$$\lambda = \frac{CO_2 + \frac{CO}{2} + O_2 + \left( \frac{H_{CV}}{4} \cdot \frac{K}{K + \frac{CO}{CO_2}} - \frac{O_{CV}}{2} \right) \cdot (CO_2 + CO)}{\left( 1 + \frac{H_{CV}}{4} - \frac{O_{CV}}{2} \right) \cdot (CO_2 + CO + K_1 \cdot HC)},$$

where λ is the relative Air-Fuel Ratio and, $CO_2$, CO, $O_2$ and HC the species concentrations with the same unit (only HC needs to be converted from ppm to percentage using the relation [ppm/10000]). $H_{CV}$ is the hydrogen to carbon atomic ratio (1.73 for gasoline), K water gas equilibrium constant, $O_{CV}$ the oxygen to carbon atomic ratio and $K_1$ the flame ionization detector FID/NDIR conversion factor. Regarding emissions measurement, the principle is based on the non-dispersive infrared (NDIR) for CO, $CO_2$ and HC concentrations, and electro-chemical for $NO_x$ and $O_2$. The AVL equipment features an overall accuracy of around 3% [32], the error may increase with the measured value, but in any case, not more than 5%. Experimental tests were carried out using two different types of spark plug, mounted in the combustion chamber: a concentric electrode spark plug (NGK 6839 R2349-10 Racing plug) and a double J-type electrode spark plug (NGK DCPR8EKC), shown in figure 2.5. The orientation of the latter was studied in two different configurations: Crossflow [21] and Uniflow, where for the first the ground electrodes act as "shield" for the flow coming from the intake valves. The second one features the ground electrodes rotated by 90 angles degree respect to the previous position. In figure 2.6 these analysed spark plug geometries are showed.


*Figure 2.5, (a) Double J-type electrode spark plug, (b) Concentric electrode spark plug*

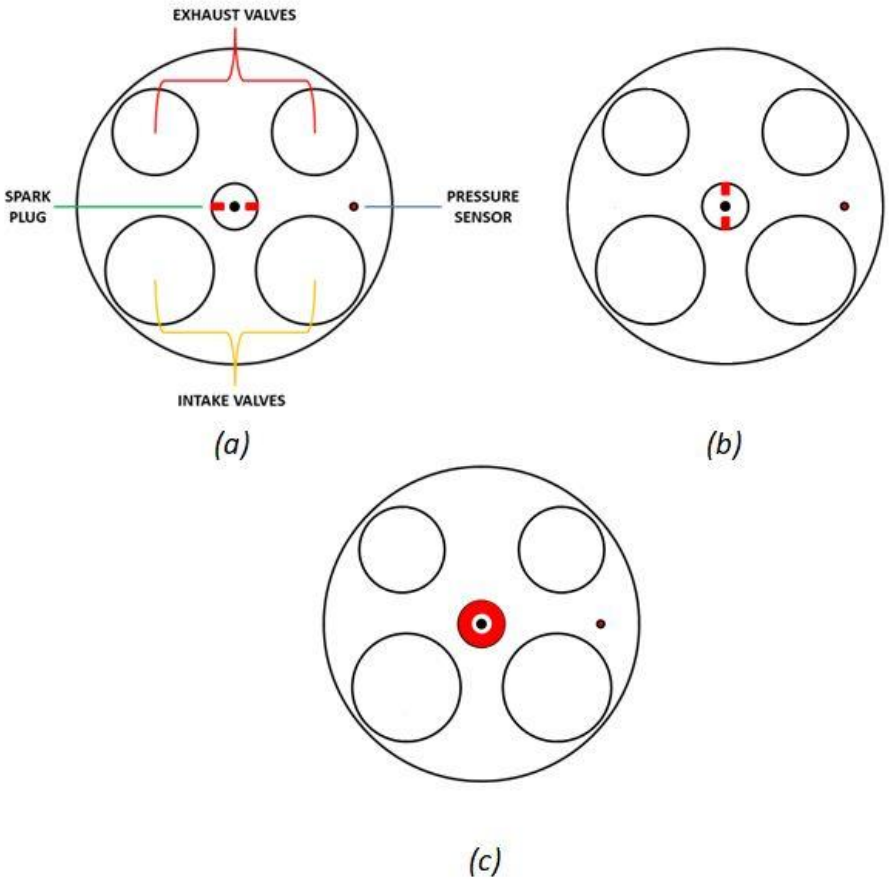


*Figure 2.6, (a) Crossflow, (b) Uniflow, (c) Concentric electrode spark plug*

Acting on the throttle valve opening level it was possible to set different intake pressures, while for the variation of AFR the (DOI) was increased or reduced. The intake air temperature was around 300K and monitored by a thermocouple placed in the intake manifold. A Bosch absolute pressure sensor was used for measuring the intake pressure with an accuracy of ±1%. Oil and water temperatures were managed and regulated by a thermal conditioning system comprehensive of an electric heater and a heat exchanger. It permitted to maintain a wall of the cylinder liner temperature between 330-335K. Under normal conditions for the engine, it was necessary to maintain a moderate temperature to protect the elongated piston-bore assembly that features high tolerance specific for optical engines. Finally, a transducer (AVL GH12D) was used to measure the in-cylinder pressure with an accuracy of ±1% and resolution of 0.2 CAD. Piezoelectric pressure sensor working principle is based on the electrical charge output of quartz crystal under mechanical load. Therefore, the output charge is proportional to the pressure difference applied, and it is converted to a voltage signal by a charge amplifier (AVL FI Piezo-Amplifier). The pressure trace used for the thermodynamic analysis, for the different cases, was obtained as an average of 200 recorded cycles. Figures 2.7 and 2.8 show the different components of the experimental setup.

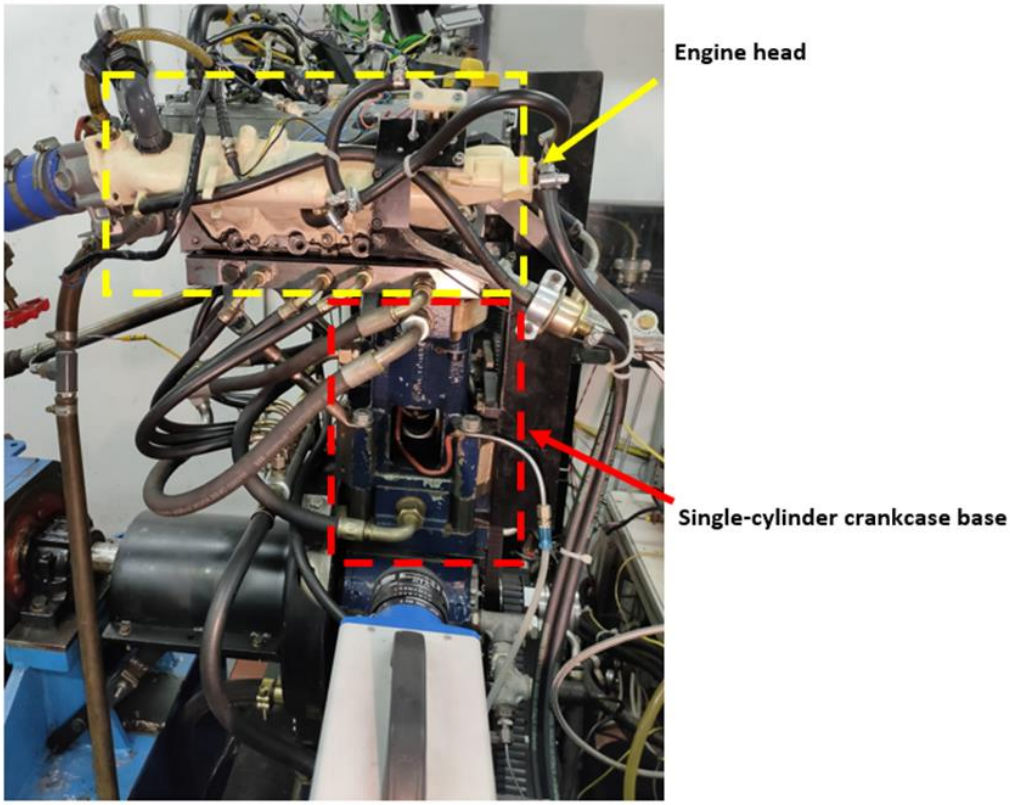


*Figure 2.7, Engine experimental setup*

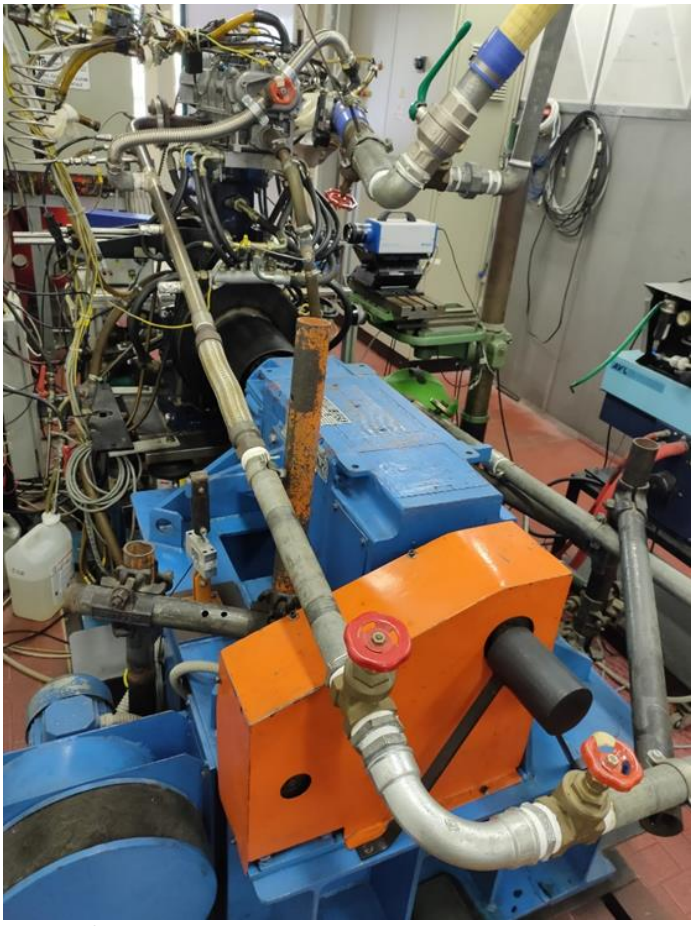

*Figure 2.8, Electric motor/brake coupled with the engine (49.7 kW power, 230 Nm maximum torque)*

## 2.2 Optical Setup

For this experimental engine, the original metal piston has been replaced by a Bowditch extended piston to allow the observation and study of the phenomena inside the combustion chamber during all the firing phases. In order to achieve this purpose, a 45° tilted mirror is fitted at the base of the elongated piston whose head section is moreover replaced by a quartz window. The last-mentioned ensured a field of view of 62 mm in diameter, corresponding to 60% of the piston cross section. The strong influence that its degree of cleaning has on the quality of recorded images stands consequently evident; therefore it is recommended to acquire the necessary optical data with the minimum number of operational tests, but even with these precautions the piston top needs to be removed and cleaned after a certain number of tests performed. To avoid excessive thermal expansion of the piston top, the housing of quartz window is made of steel (ck45); furthermore the heat transfer to the quartz, and consequently its overheating, is reduced since laboratory tests last no longer than a few minutes. The Bowditch piston, characterised by a flat bowl, produces a lower effective compression ratio and, compared to the original piston used in the four in-line engine, the resulting geometry can be considered as representative of automotive applications. The extended piston involves the use of three stock slotted graphite piston rings (figure 2.9) to provide oil-less lubrication with uninterrupted bronze-Teflon rings used for sealing. Due to these numerous mechanical limitations, laboratory tests have sometimes been repeated for a more accurate analysis of data. A schematic representation of a Bowditch extended piston design is reported in the figure 2.10 [33].


*Figure 2.9, 3D render visualization of piston crown*

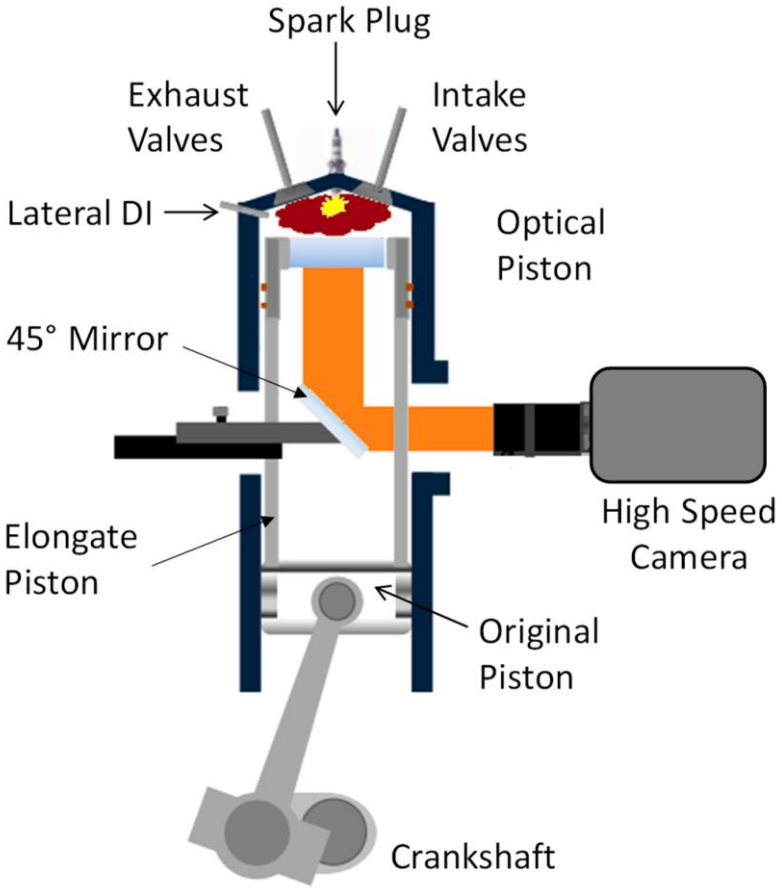


*Figure 2.10, Schematic representation of a Bowditch extended piston [33]*

Flame front propagation was investigated through cycle resolved digital imaging carrying out the acquisition of images with a high-speed CMOS camera (CamRecord 5000, 8-bit, 16 µm x 16 µm pixel size by Optronis, Kehl, Germany, figure 2.11 [34]) equipped with a 50 mm Nikon objective. The camera was set in full chip configuration with a resolution of 512x512 pixel and acquisition speed of 5000 frames per second, with an exposure time of 167 µs. The f-stop of the objective was set at 2.8 to improve the signal-to-noise ratio without extensive saturation effects. Therefore, for the set-up allowed the images were recorded with a dwell time of 2.4 CAD at 2000 rpm and a spatial resolution of 0.19 mm per pixel.

*Figure 2.11, High-speed camera CMOS, CamRecord 5000 by Optronis [37]*

A statistical analysis was carried out in order to establish the minimum number of consecutive cycles, recorded by the high-speed camera, required for optimal representation

of the sample of 200 acquired cycles for each condition. For full load operations, the aforementioned sample is well represented by 10 sequences, while for throttled and low engine speed operations the optimal solution turns out to be 20. Each sequence featured 25 consecutive frames with an interval of 2.4 CAD (0.2 ms) starting from the spark timing as reported in figure 2.12.

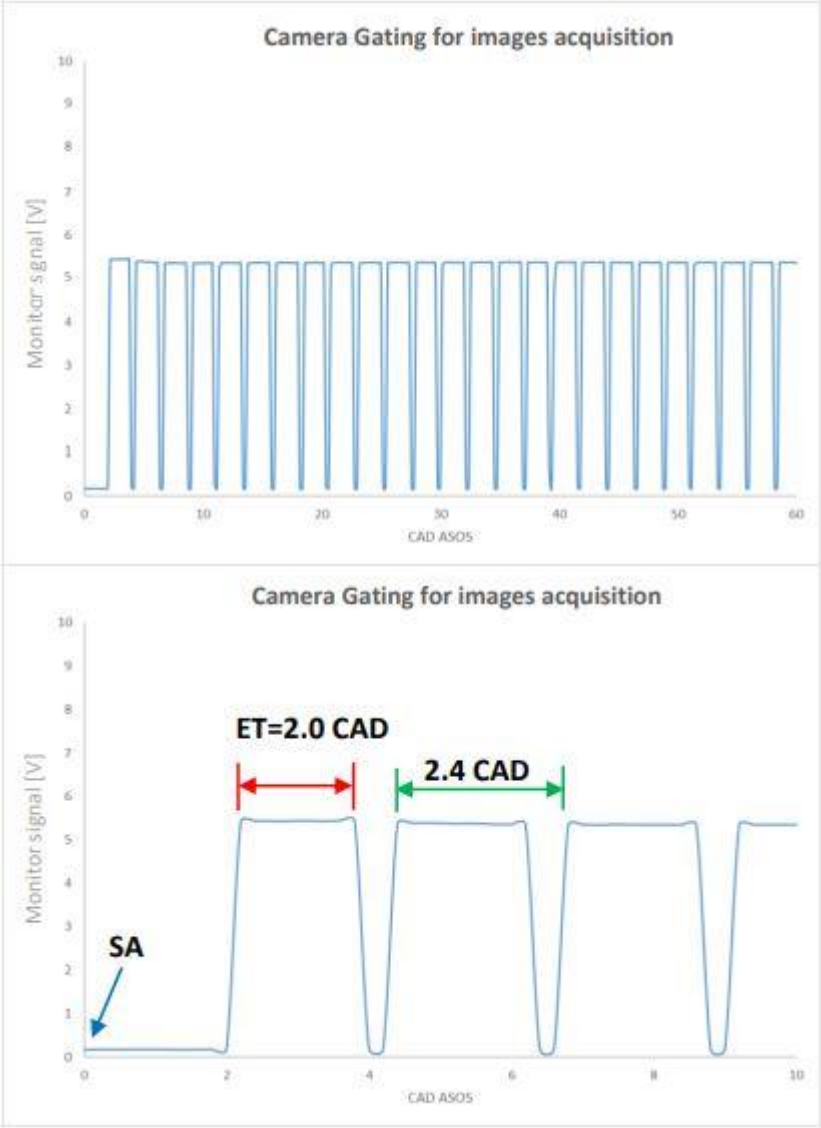


*Figure 2.12, Camera gating for acquiring 25 images per cycle*

The acquisition of quantitative kernel information from cycle resolved images could be negatively affected by two factors: the presence of the spark plug and highly lean air-fuel mixtures. Firstly, the actual flame kernel could be hidden by the ground electrodes, so the software returns a frame with no object visualized. Excessive mixture leaning could, on the other hand, result in reduced brightness and brilliance of the acquired images, thus complicating kernel analysis. Therefore, it is intuitive to note the importance of the subjective sensibility imposed during this type of analysis and the subsequent choice of parameters when using the NI Vision software to optimize the recorded images.

# Chapter 3 – Procedure and Measurement Methodology

## 3.1 Pressure Related Data Acquisition

During the experimental tests the following signals were acquired and recorded: in-cylinder pressure, intake pressure, equivalence ratio, signals of primary and secondary current of the ignition system. The first step of the thermodynamic analysis was the in-cylinder pressure analysis performed through a dedicated script built in National Instrument LabView software. The latter was necessary to summarize the information coming from 200 cycles in a single average signal with the steps reported in figure 3.1.

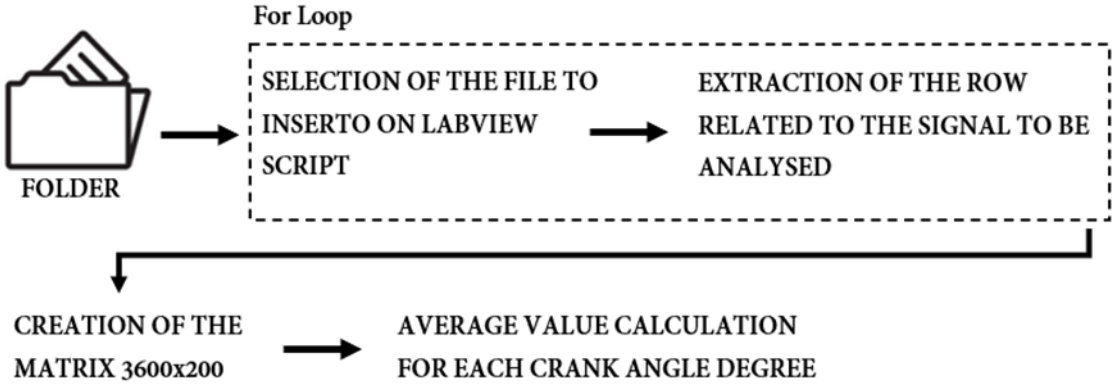


*Figure 3.1, LabView script for in-cylinder pressure analysis*

A correction had first to be made on the acquired data to plot the average in-cylinder pressure signal. Since the latter is calculated incrementally, it is necessary, due to the measurement principle, to define a referring point by equalizing the average in-cylinder pressure value to the average intake pressure signal at 180 CAD BTDC. After this step, it is possible to study and compare the average pressure traces for each case that was analysed. The work carried out in this phase provides the comparison of the results for different values of AFR, spark plug orientations, Spark Advance (SA), load ($P_{intake}$) and engine speed to investigate these parameters effect on CCV.

## 3.2 Thermodynamic Analysis

One of the first parameters investigated was the Indicated Mean Effective Pressure value, IMEP. The cylinder clearance volume, required to calculate these parameters, has been calculated with the compression ratio and displacement values.

$$V_C = \frac{V_D}{(CR - 1)}$$

The equation reported above is simplified as it neglects the crevices volume and the variation of the compression ratio due to the elongated piston. For this reason, a thermal analysis was carried on the engine to verify the expansion levels of components during the motored and firing operative conditions. Therefore, the in-cylinder free volume for every crank angle degree can be obtained with the relation:

$$V = V_C + \frac{\pi B^2}{4} * (l + a - s)$$

where B is the bore, l the connecting rod length, a the crank radius and s the distance between the crank axis and piston axis, this last is given by:

$$s = a\cos\theta + (l^2 - a^2\sin^2\theta)^{\frac{1}{2}}$$

A schematic representation of cylinder geometry is showed in figure 3.2 [15].

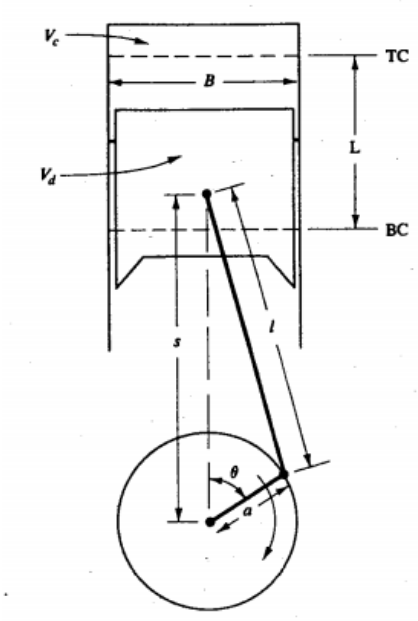


*Figure 3.2, Simplified cylinder geometry [15].*

From the estimated data, it is possible to calculate the $W_{c,i}$ (Indicated Work per Cycle) for each set of 200 cycles with the following relation [15] using a loop block in LabView,

$$W_{c,i} = \oint p dV$$

where p is the in-cylinder pressure measured expressed in Pa and dV the instantaneous variation of the in-cylinder volume. The following equation allows to consequently calculate the IMEP,

$$\mathrm{IMEP} = \frac{\mathrm{W_{c,i}}}{\mathrm{V_D}}$$

where $V_D$ is the displacement of single-cylinder engine, reported in the Table 2.1. Consequently, it has been possible to estimate the stability of combustion process, for the recorded series of data, with the evaluation of the related $COV_{IMEP}$ which gives an overview of engine output. The latter was calculated for population of 200 values of IMEP with the relation below,

$$\mathrm{COV_{IMEP}} = \frac{\sigma_{\mathrm{IMEP}}}{\mu_{\mathrm{IMEP}}} * 100$$

where the $\sigma_{IMEP}$ indicates for the Standard Deviation, while $\mu_{IMEP}$ is the average value for the 200 cycles under analysis. A similar procedure is used for calculating the pressure peak reached in the combustion chamber and relative $COV_{Pmax}$, more closely related to the actual variability of combustion. With the referenced and averaged pressure signals, it is possible to calculate the Mass Fraction Burned values (MFB), and subsequently the Volume Fraction Burned (VFB). Heat release rate analysis was performed with a simplified approach of the first law of thermodynamics, using the equation:

$$\mathrm{dQ} = \frac{\gamma}{\gamma - 1} * \mathrm{p} * \mathrm{dV} + \frac{1}{\gamma - 1} * \mathrm{V} * \mathrm{dP}$$

where Q is the net heat release rate measured in Joule for crank angle, p the in-cylinder pressure in Pa, V is the instantaneous in-cylinder free volume in $m^3$, dP the instantaneous variation of the in-cylinder pressure, and the ratio of specific heats γ was set to 1.35. MFB was calculated based on the integral of heat release,

$$\mathrm{MFB} = \frac{\mathrm{Q_k} - \mathrm{Q_{ST}}}{\mathrm{Q_{EVO}} - \mathrm{Q_{ST}}}$$

where subscript k is related to the current crank angle position while ST stands for spark timing crank angle and EVO for the exhaust valve opening. With the MFB trend it is possible to divide the combustion into several stages and recognize the fundamental points of the process. The CA window that corresponds to 0–10% MFB is related to the flame development angle, 10–90% MFB corresponds to the rapid burning angle, and 0-90% MFB consists of the overall duration of the process. Finally, with the $MFB_{50\%}$ point is possible to understand if, for the parameters set, the engine is close to working at the Maximum

Brake Torque (MBT) condition. Once MFB was known, it was possible to calculate the evolution of the burned volume fraction using the relation:

$$\mathrm{VFB} = \frac{1}{\left[\frac{1}{\mathrm{MFB}} - 1\right] * \frac{\rho_b}{\rho_u} + 1}$$

where the density ratio between the burned and unburned mixture is set to 0.25 as representative of most of operative conditions of a SI engine [15].

## 3.3 Image Processing

Flame kernel displacement and flame morphology have been evaluated from the recorded optical data through a script built in NI Vision. For each considered case, the procedure starts with the use of “Measure” processing function, needed to convert pixels in millimetres (the ratio is about 5.2 pixels per millimetre) and define the position of the centre of the spark plug for subsequent considerations on flame kernel velocity, displacement and flame front propagation direction. After this initial step, a circular mask was applied to the images coming from the sequences to limit the investigated area to the quartz window fitted on the piston top and to cut light from reflections at the boundaries of the optical access. Note that the parameters used for these first two steps can change from a series of cases to another due to possible variations of the position of the high-speed camera with respect to the crankcase (e.g., for working on the engine). Next step the “Color Plane Extraction” function was used. In this way, by selecting the HSI command, it is possible to extract the three color properties: hue, saturation and intensity. After this phase it is possible proceed with improving image quality by employing the “Brightness” and “Look up table” functions. The first one, combined with the second, was used two times to obtain improved contrast, gamma, brightness and subsequently a reduction of signal-noise ratio. Finally, a threshold level was applied to obtain binary images. The choice of the latter parameter is strongly linked to the user sensibility; in fact, defining a grey level on a scale of 1 to 256, it is possible to tell the software when a particular pixel needs to be "seen" or not. Therefore, it is intuitive that setting a lower value of grey on the scale can be helpful for the analysis of the first stage of combustion process but not for fully developed flames; in fact for the latter many small objects not being part of the flame front would form during the visualization phase, with the risk that the software confuses one of these with the main flame area. This is a situation to be avoided because, during the results export stage, the software would save the objects from the signal-to-noise first and not the main flame, resulting in errors on subsequent analyses. Therefore, for the operative conditions with $\lambda$=1.00-1.15, the threshold was fixed at higher values compared to the ones used for the cases with leanest AFR to improve the image processing quality. Finally, using the “FFT filter” and “Advanced morphology” functions, it is possible reduce the signal-noise ratio and fill any eventually holes in the foreground figures. Further clarifications are required for the FFT filter function, with respect to the “error” that occurs with the original frame parameters. The modality of filtration was set on “low pass” with a truncation level of 20% and an error of less than 2% between the flame area morphology parameters (before and after the correction) was observed. In the final steps of the procedure, the “Particle Analysis” function was used to save the information on flame kernel morphology. The sequence of steps applied for performing the analysis is illustrated in figure 3.3.

However, as previously said, the optical analysis is strongly dependant on user sensibility in setting the required parameters for running the NI Vision script; therefore, a further validation measure was performed to ensure that the greyscale parameter (which directly influences the flame detection sensitivity of the software) was correct and not over- or underestimated. For each analysed case, the average Volume Fraction Burned trace obtained from the thermodynamic analysis of 200 consecutive cycles was compared with the closest VFB trace among those obtained from the recorded cycles; then the evolution of the normalized flame area ($A_{nf}$) from this chosen sequence was examined. This simplified method allows a rapid check of the correct settings for greyscale value, given that the evolution of the flame area is directly related to the sensitivity of the NI Vision script.

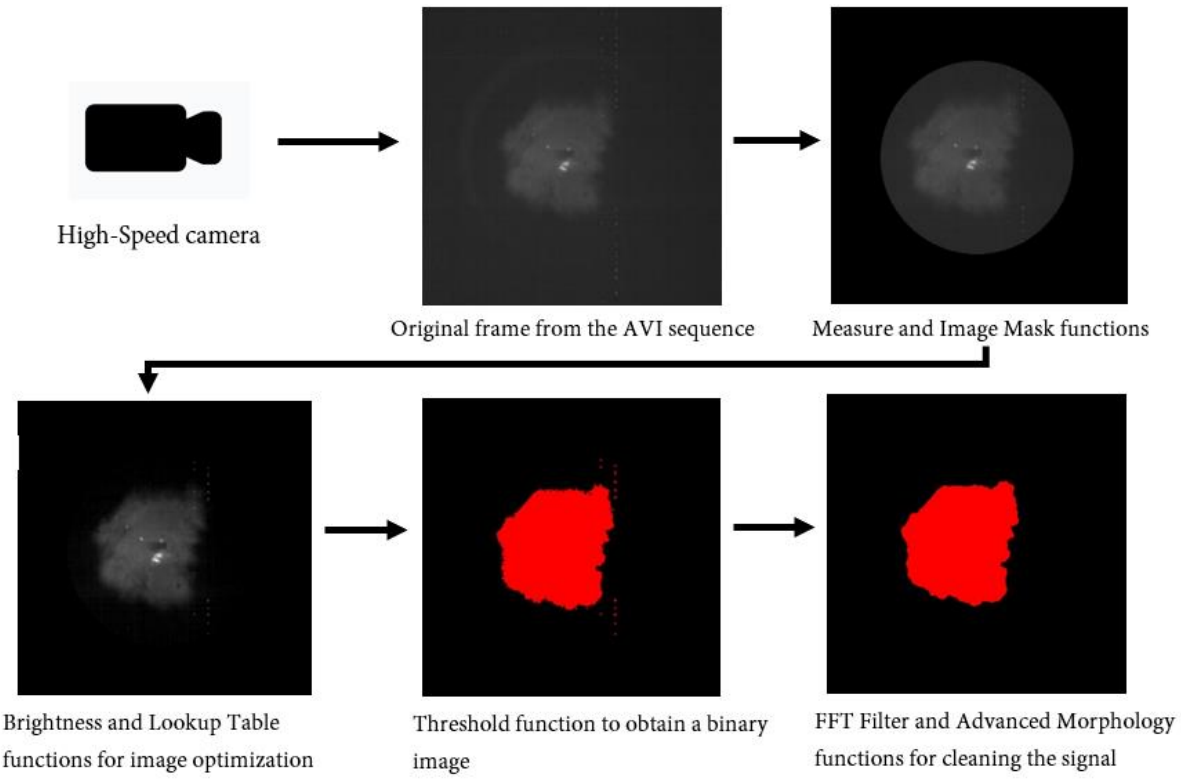


*Figure 3.3, Steps of the NI Vision script used for image processing*

## 3.4 Statistical Analysis

As formerly mentioned, a statistical analysis was carried out to establish the minimum number of consecutive sequences, recorded by the high-speed camera, which composes a representative sample required for an optimal verification of the greyscale parameter, described in the previous paragraph. Optical acquisitions of 10, 20, 40 and 80 sequences were performed for a specific reference case (Concentric electrode spark plug, 2000 rpm, WOT, $\lambda$=1.15±1%, ST 16 CAD BTDC). For each acquisition, the correct setting of the threshold parameters was previously verified through the aforementioned comparison of the VFB and normalized flame area traces, as can be seen in the following figure 3.4.

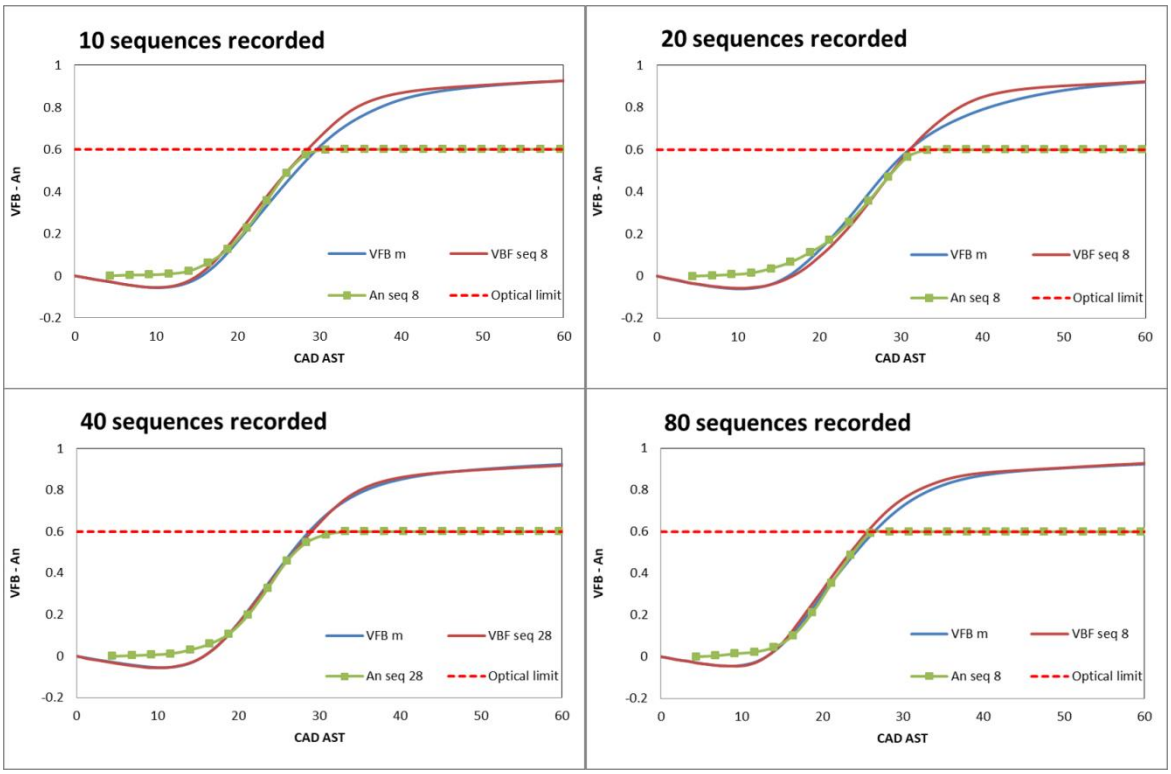


*Figure 3.4, VFB and normalized flame area traces comparison for 10, 20, 40 and 80 recorded sequences*

Subsequently, the COVs for the above quantities were estimated for each acquisition and confronted. The $COV_{Anf}$ was calculated at 16.4 and 23.6 CAD AST (1.4 ms and 2.0 ms after spark time) to ensure that the optical limit was not yet reached by the flame, as shown in the above figure. Regarding the Volume Fraction Burned, the estimation was instead carried out exclusively at 23.6 CAD AST in order to guarantee purely positive calculation values. In the obtained results, summarised in the figures 3.5 and 3.6, It can be seen that the optimal choice is 20 recorded sequences for which the lowest COV values are obtained. However, the group of 10 sequences does not differ significantly in terms of the coefficients of variation from the others (especially 40 and 80 sequences, which present comparable values); for this reason, 10 sequences were recorded for WOT tests and 20 for throttled and low engine speed operation, which tend to be more prone to cyclic dispersion phenomena.

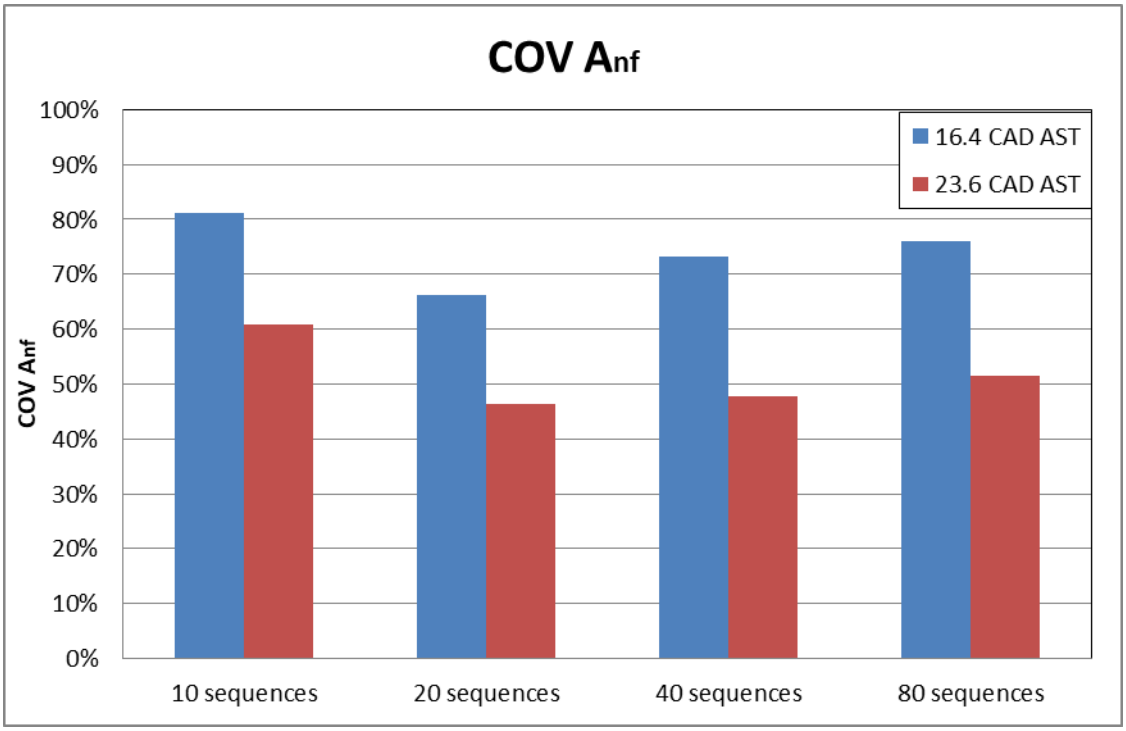


*Figure 3.5, Normalized flame area COVs comparison*

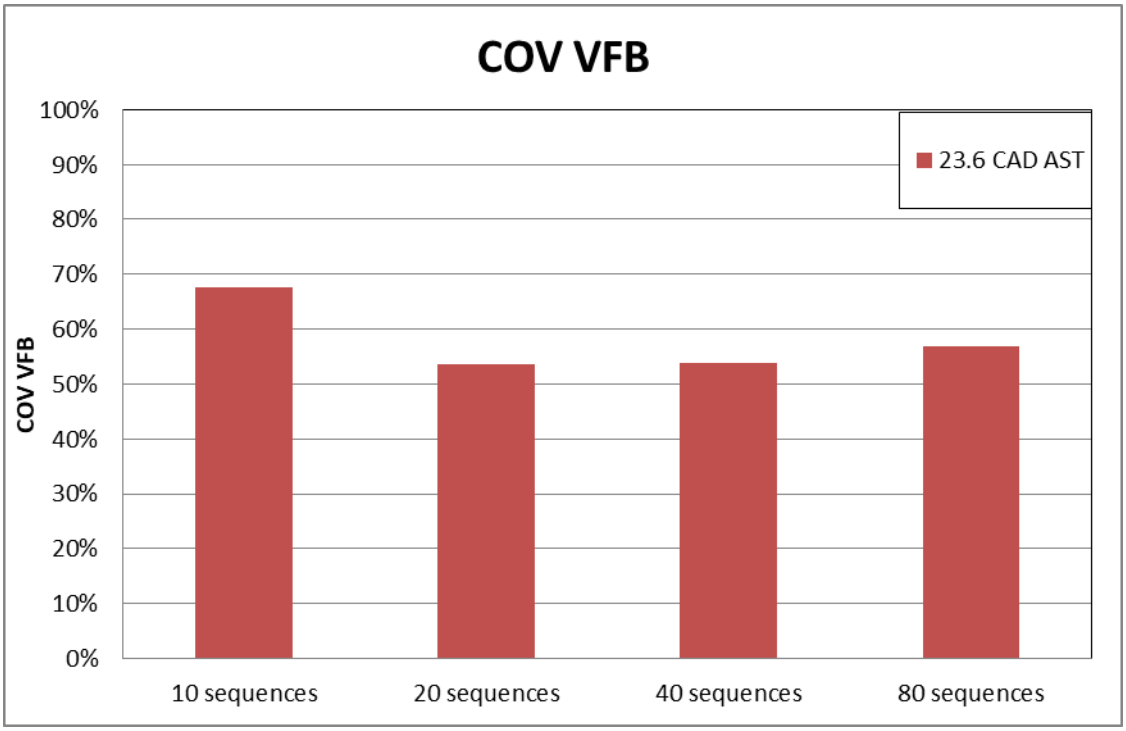


*Figure 3.6, Volume Fraction Burned COVs comparison*

## 3.5 Optical Investigation

From image processing and specifically through the "Particle Analysis" function, different data on the morphology of the flame kernel were saved: coordinates of the centre of mass, perimeter, maximum Feret diameter ($d_{Feret}$) and area. The Feret diameter, in particular, is defined as the distance between the two parallels tangent to the perimeter of the area projected by the particle. Since an infinite number of $d_{Feret}$ values can ideally be determined for a single particle, a maximum value is used. With regards to the figure 3.7, average displacements along the horizontal and vertical axis of the flame area were calculated using the following equations,

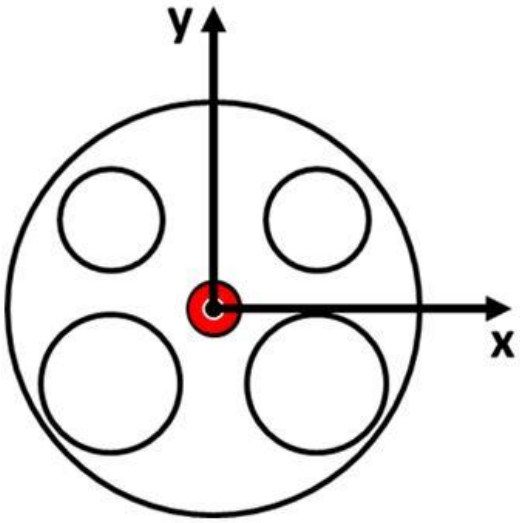


*Figure 3.7, Combustion chamber axes configuration*

$$Dx = \left(x_{flame\ center\ of\ mass} - x_{spark\ plug\ center}\right) * 0.187$$

$$Dy = -\left(y_{flame\ center\ of\ mass} - y_{spark\ plug\ center}\right) * 0.187$$

$$R = \sqrt{Dx^2 + Dy^2}$$

where 0.187 is referred to conversion from pixels to millimeters and R is the kernel dislocation resultant. Moreover, through the optical data collected it was possible, from the aforementioned maximum Feret diameter of the flame front area, to define the expansion speed. The succeeding equation was used,

$$V_{Feret} = \frac{\left|d_{Feret_{n-1}} - d_{Feret_n}\right|}{5.2} * \left(\frac{1}{2}\right) * \left(\frac{1}{0.2}\right)$$

Where 5.2 is related to conversion from pixels to millimeters, while 0.2 to the time distance in seconds between each frame.

# Chapter 4 – Results

## 4.1 Operative Conditions

In the current experimental work, investigations were focused on CCV and the correlation between in-cylinder thermodynamic parameters and flame characteristics. Operative conditions entailed a sweep of Air-Fuel Ratio (AFR), Spark Advance (SA), intake pressure ($P_{intake}$), engine speed (n) and spark plug configuration. Tables 4.1 lists the fixed operating conditions for each case analysed consisting of injection pressure, start of injection (SOI) and coil charge duration. This latter was set at 40 CAD since its effect on flame kernel formation and front propagation is not appreciable and does not show a well-defined trend in their variation, as proved by previous studies [35]. The case-specific settings are summarised in the Tables 4.2-4.3.

| | |
|---|---|
| Injection Pressure [bar] | 100 |
| Coil Charge Duration [CAD] | 40 |
| SOI [CAD BTDC] | 300 |

*Table 4.1, Fixed operative conditions*

| λ | Engine Speed [rpm] | Intake Pressure [bar] | Spark Advance [CAD] |
|---|---|---|---|
| 1.00 | 2000 | 1.00 (WOT) | 12 |
| 1.15 | | | 8<br>12<br>16<br>20 |
| 1.30 | | | 12<br>20 |

*Table 4.2, Engine operative conditions for WOT operations*

| λ | Engine Speed [rpm] | Intake Pressure [bar] | Spark Advance [CAD] |
|---|---|---|---|
| 1.00 | 1000 | 1.00 (WOT) | 12 |
| | 2000 | 0.75 | 12 |
| | | 0.50 | 12<br>24 |

*Table 4.3, Engine operative conditions for throttled and low speed operations*

During the tests, provided in several sessions, different thermal parameters were monitored to ensure a steady thermal regime of the engine and results' uniformity from each measurement operation. Firstly, the intake air temperature (equal to the ambient one,

therefore the tests were carried out in the same period to avoid the problem related to appreciable variations in its value) was kept around 300K. A second monitored variable consists of the exhaust gas temperature, maintained approximately at 690K; finally the coolant system temperature was held in a range between 330-335K, for the input/output water-flow respectively. Another important step in data acquisition was related to the continuous evaluation of piston seals wear to ensure that blow-by leaks were kept in a narrow range. In addition, for each series of tests performed, the cycle acquisition under the same conditions of motion and fire was carried out at the beginning and at the end of each session in order to further confirm the validity of the recorded data. A final and fundamental analysis was conducted on the in-cylinder pressure values at spark timing to prove that the latter remained in a narrow range for all configurations characterized by the same advance setting. For this purpose, the average pressure traces (figure 4.1) obtained from the LabView script were compared and cases where the abovementioned range was not achieved were discarded.

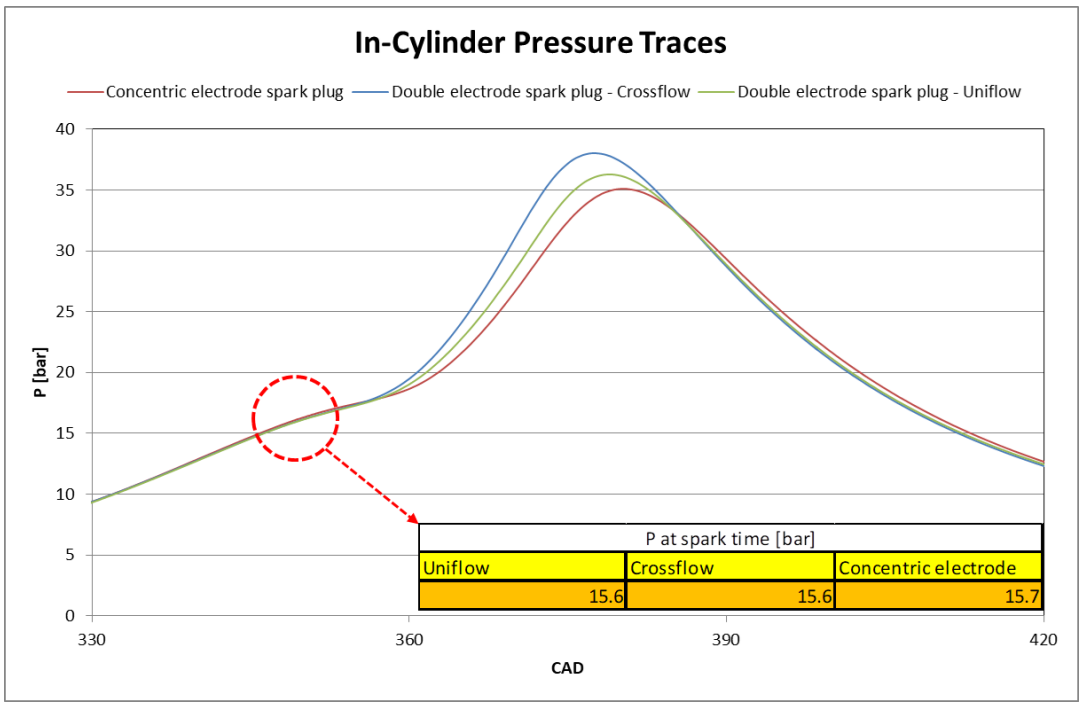


*Figure 4.1, In-Cylinder pressure traces, n=2000 rpm, WOT, λ=1.00, SA 12 CAD*

For the example shown in figure 4.1, obtained with stoichiometric air-fuel mixture (λ=1.00) and fixed Spark Advance (SA) of 12 CAD in WOT operations, it is possible to note a gap at spark timing of less than 0.1 bar, a negligible difference.

## 4.2Thermodynamic and Optical Results

The results extracted from both the thermodynamic and optical analysis will be presented to obtain a comparison, in these terms, between different spark plug configurations. The data presented are organized by parameters settings; specifically in the following sections will be examined the separated effects of Spark Advance, AFR, load and engine speed on the combustion process. During the analysis of each of them, the remaining operating conditions will be fixed to quantify each effect under conditions involving a certain cause, with other influences reduced as much as possible.

The first part of each section will include, as anticipated, a thermodynamic analysis carried out by comparing the average pressure cycles, specifically examining the values obtained in terms of IMEP, maximum in-cylinder pressure and respective COVs in order to quantify potential CCV phenomena. This will be followed by the average VFB traces analysis aimed at a more in-depth characterisation of the combustion related phenomena and supported by a subsequent optical investigation. The sequences of images acquired with the high-speed camera will be indeed post-processed and analysed to have a better understanding of the spatial behaviour of the combustion process; after a preliminary check of the greyscale parameters previously described in paragraph 3.3, the data obtained in terms of flame expansion speed ($V_{Feret}$) and kernel displacements will be examined for each case of interest.

## 4.3Effect of Spark Advance

### 4.3.1 Effect of Spark Advance for λ=1.15

The following results are related to the operative condition for a fixed Duration of Injection (DOI) of 34 CAD corresponding to λ=1.15 and variable Spark Advance (SA) from 8 to 20 CAD with a step of 4 CAD between each case. Starting from the average signal of in-cylinder pressure traces, these one are compared for the three examined spark plug geometries, figures 4.2-4.5, for each SA value.

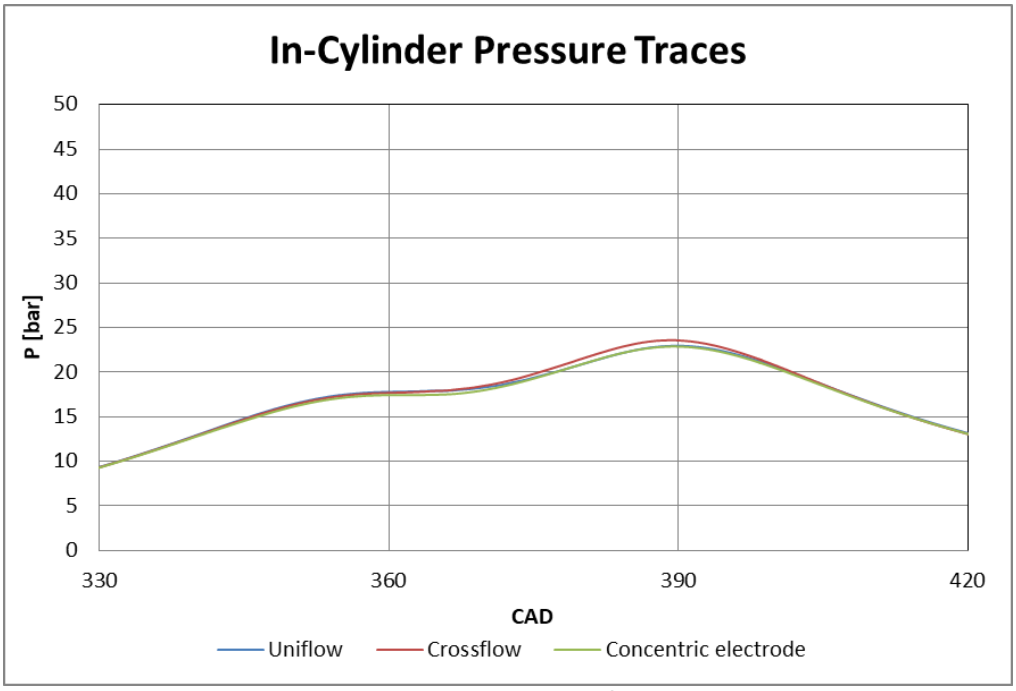


*Figure 4.2, In-cylinder Pressure traces for λ=1.15 and SA 8 CAD*

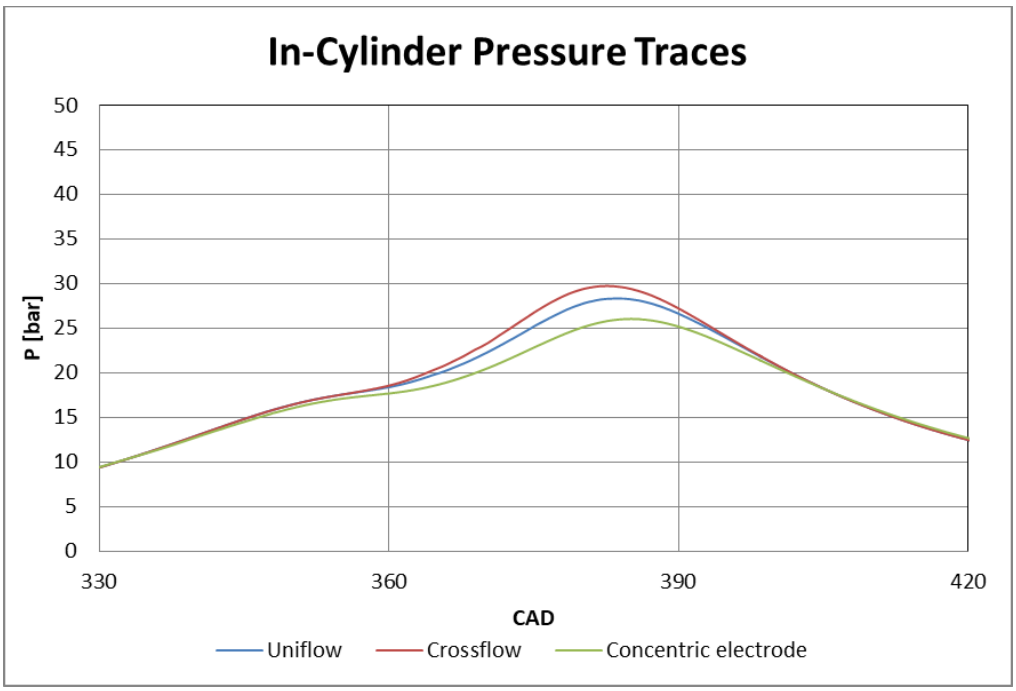


*Figure 4.3, In-cylinder Pressure traces for λ=1.15 and SA 12 CAD*

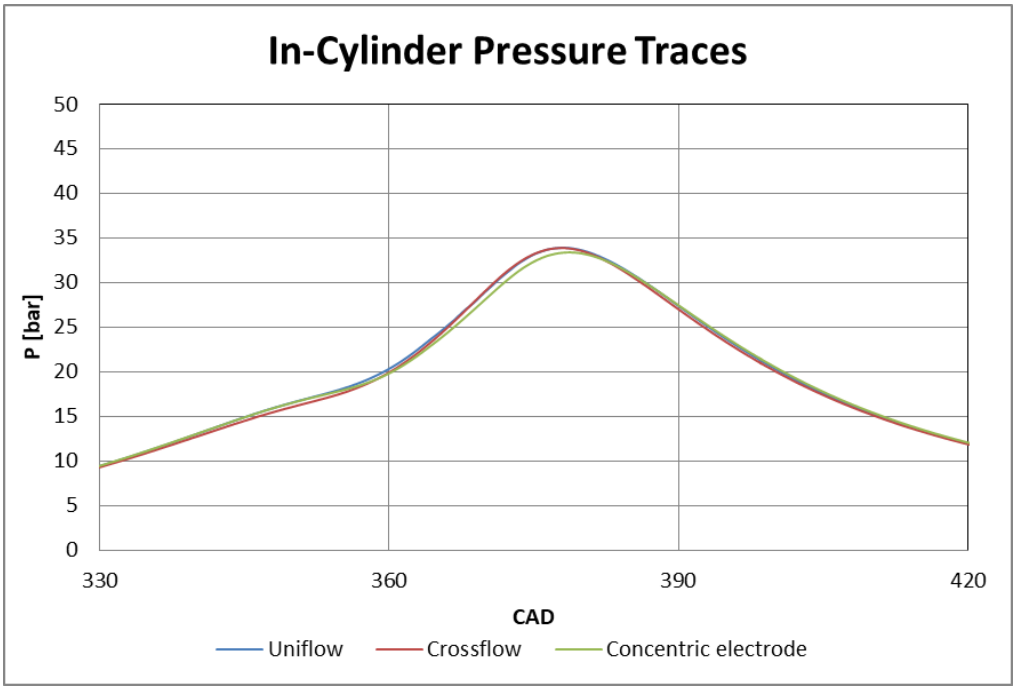


*Figure 4.4, In-cylinder Pressure traces for λ=1.15 and SA 16 CAD*

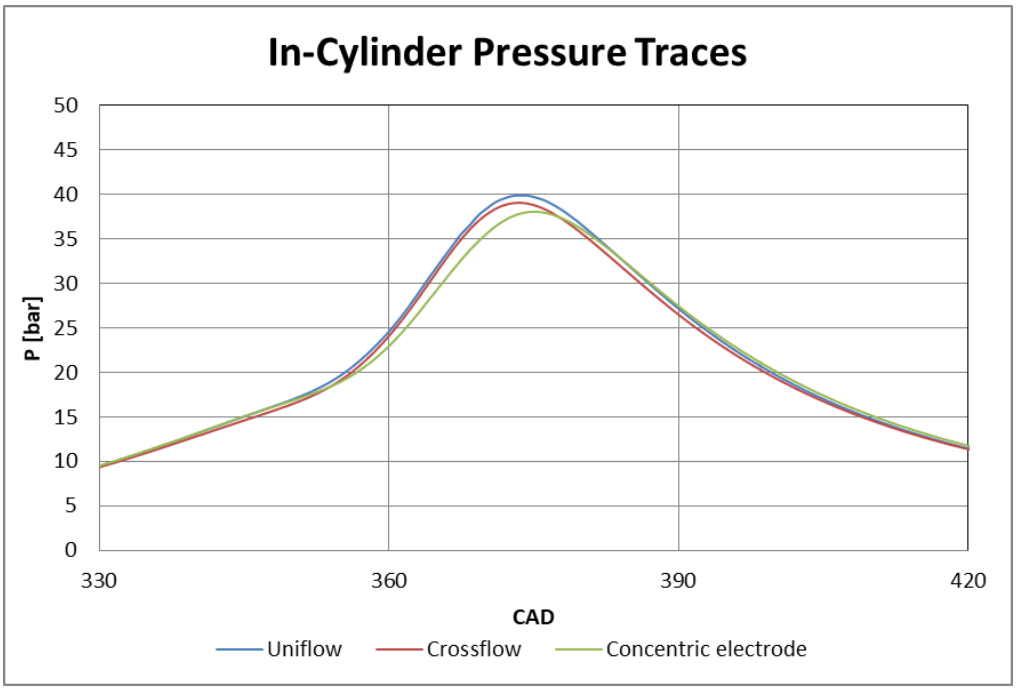


*Figure 4.5, In-cylinder Pressure traces for λ=1.15 and SA 20 CAD*

As expected, anticipating the spark timing angle, the in-cylinder peak pressure reached higher values due to an earlier start of combustion during the compression stroke; therefore the compression related to the flame front propagation added to that due to the piston returns an increasing value of it. Nevertheless, as ignition advances, compression work tends to increase, thus leading to increased counter torque on the crankshaft.

The crossflow configuration shows the highest values for each case examined (the only exception is for SA 20 CAD) while on the other hand the lowest peak pressures are reached by the concentric electrode spark plug geometry. It is interesting to observe how the three signals feature a visible gap between them for the SA operating condition of 12 CAD. This

gap tends to reduce with an anticipated Spark Advance timing since the combustion process begins in a part of the cycle with more stable organized flow (i.e. tumble) and consequently a lower CCV value (strongly related to the $COV_{IMEP}$ values obtained). However, when spark timing occurs at 20 CAD, a new increase in discrepancy between in-cylinder pressure traces was noted. In order to more deeply analyse this phenomenon, it may be useful to observe, in comparison in the following histograms in the figures 4.6-4.7, the trend of IMEP, maximum pressure and respective COVs.

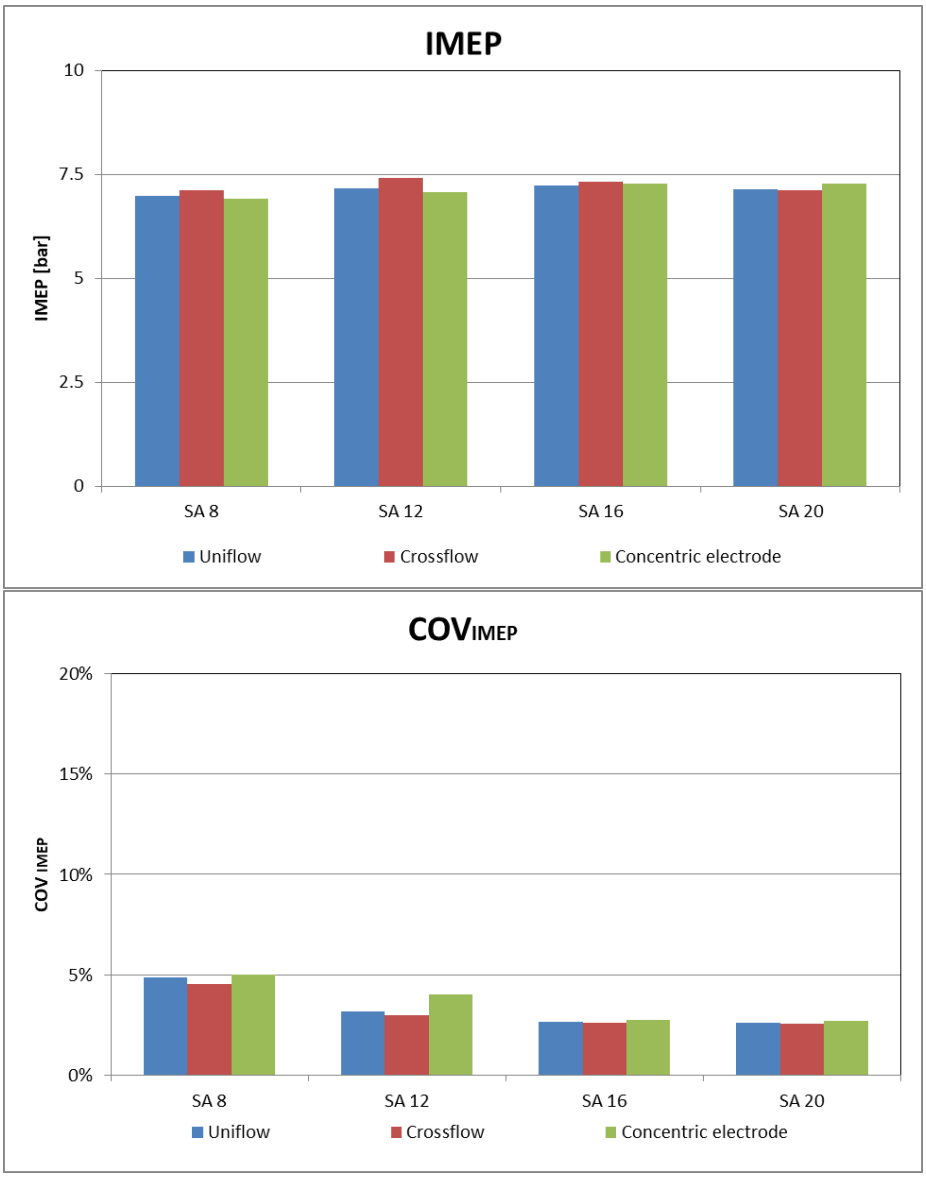


*Figure 4.6, IMEP and $COV_{IMEP}$ values for the Spark Advance sweep, λ=1.15*

Looking at the IMEP, it can be noted that the highest values, with the exception of the concentric electrode configuration, corresponding to the SA operating conditions of 16 CAD; this condition also returns a reduced cyclic variability and comparable $COV_{IMEP}$ values to the ones obtained for the SA set to 20 CAD (around 2.5%). The high stability and repeatability of the results, in these operative conditions, is due to the concomitance of these effects in the above case, in accordance with the definition of Maximum Brake Torque

operative condition (corresponding to the higher value of IMEP and acceptable level of $COV_{IMEP}$). The latter is reached for a SA of 16 CAD for the uniflow and crossflow configuration, while for concentric electrode spark plug at SA 20 CAD.

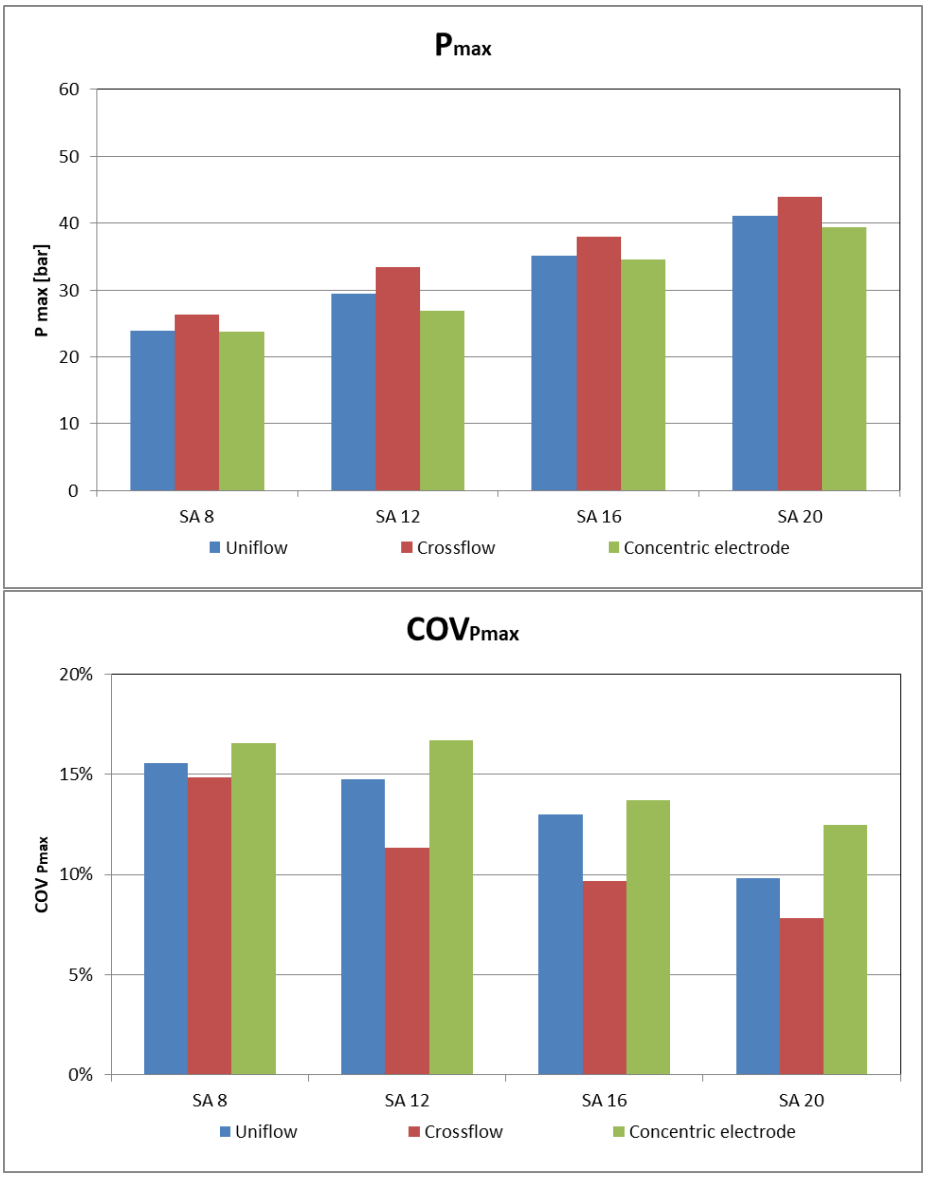


*Figure 4.7, Maximum pressure and $COV_{Pmax}$ values for the Spark Advance sweep, λ=1.15*

The maximum in-cylinder pressure reached by the three configurations shows that the concentric electrode and crossflow configurations returns respectively the highest and lowest values, as spark timing varies. However, for each spark plug geometry, the lowest cyclic variability is observed to be achieved at the Spark Advance timing of 20 CAD (9.8% for uniflow, 7.8% for crossflow and 12.6% for concentric electrode spark plug).

Figures 4.8 to 4.11 show calculated VFB traces of the three plug configurations for each spark timing. Negative VFB values are due to the simplified approach that was employed. A more complex analysis that includes heat transfer and blow-by modelling would have resulted in more plausible results. In fact, calculating the VFB from the MFB (note that the $MFB_{50\%}$ corresponds around the $VFB_{80\%}$, applying the conversion between this two

parameters reported in paragraph 3.2) the intent was of correlating the thermodynamic (i.e. the cycle most representative for an average in-cylinder evolution) and optical data; the latter category provides much more valuable information on the spatial distribution of the reacting and burned gas, as well as insight into the interaction with the working fluid. As expected, the evolution results "slower" for the most delayed Spark Advance (SA).

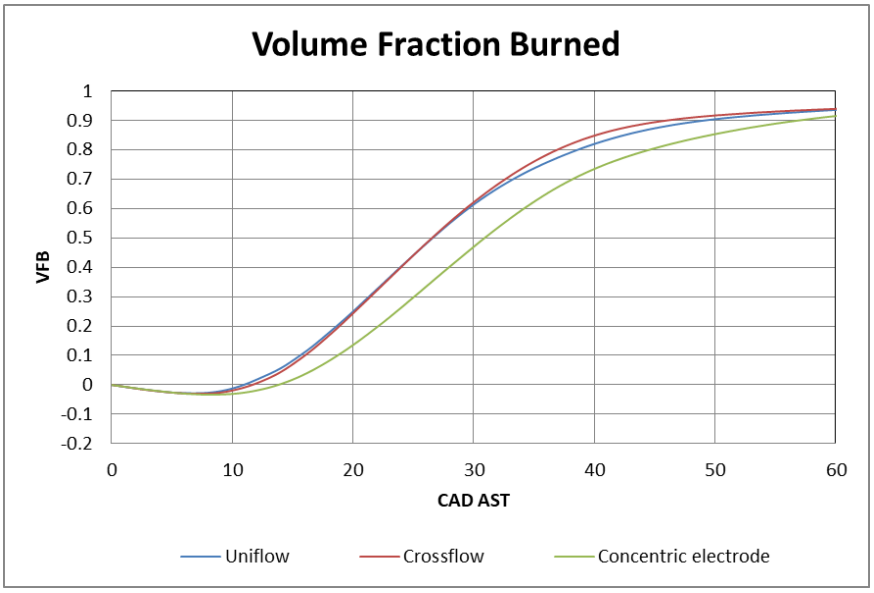


*Figure 4.8, VFB traces for λ=1.15 and SA 8 CA*

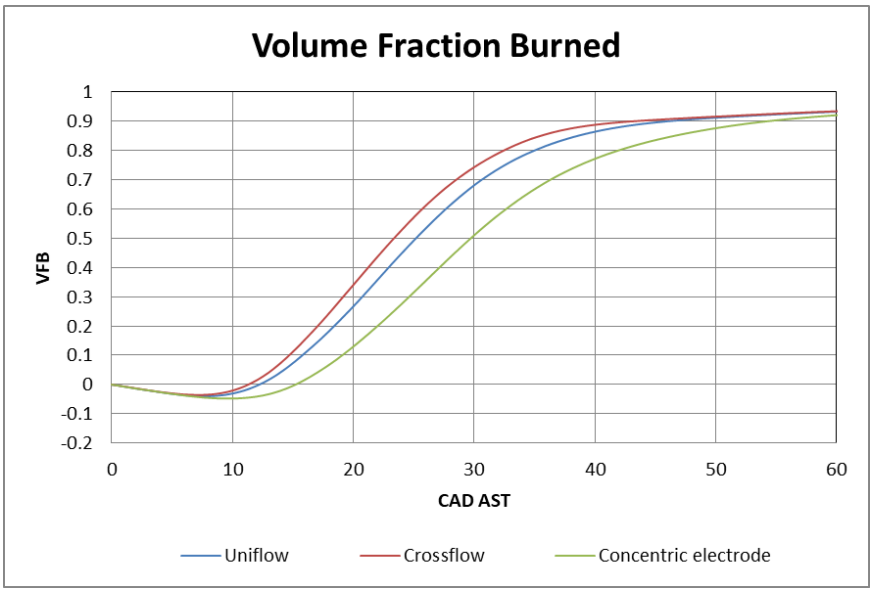


*Figure 4.9, VFB traces for λ=1.15 and SA 12 CAD*

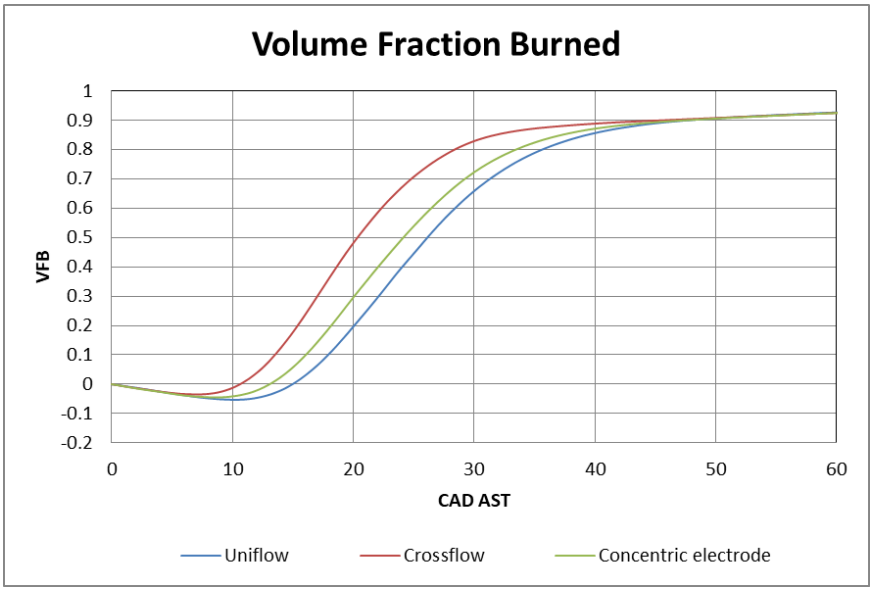


*Figure 4.10, VFB traces for λ=1.15 and SA 16 CAD*

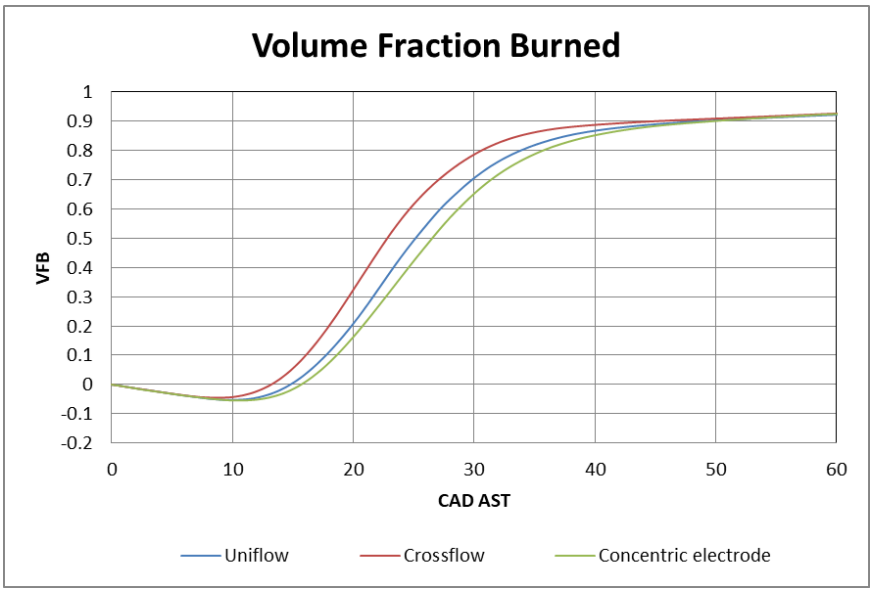


*Figure 4.11, VFB traces for λ=1.15 and SA 20 CAD*

However, as can be seen, with an SA of 20 CAD the combustion process slightly slows down compared to the previous condition (SA 16 CAD) for the three geometries. As the spark timing varies, it can be noted that the crossflow configuration evolution is in general the fastest especially in comparison to the concentric electrode VFB trace which shows a slower combustion process (except for SA 16 CAD).

Particularly interesting are the results obtained from the optical analysis in terms of the kernel displacement. From the data shown in the figure 4.12, it can be seen that the uniflow and crossflow layouts present opposite R trends as the SA varies, in accordance with an opposite orientation in the combustion chamber.

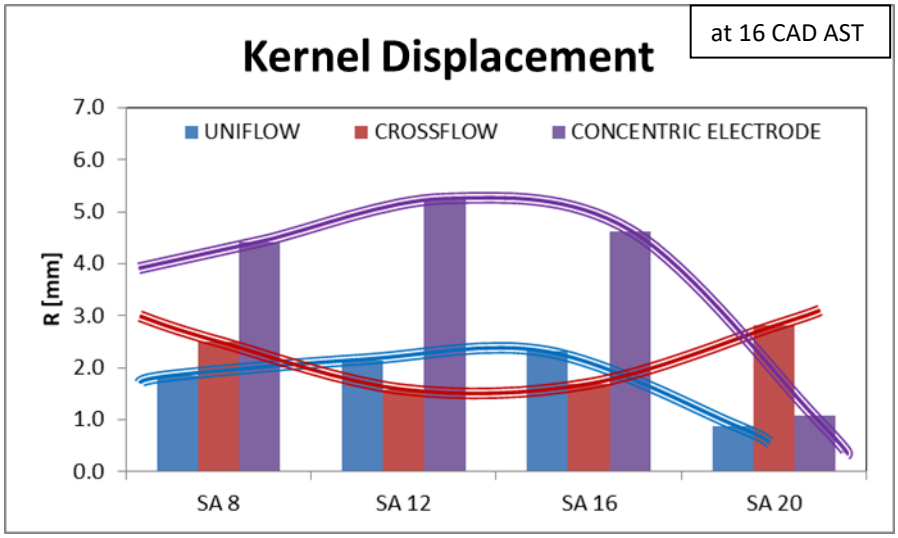


*Figure 4.12, Kernel displacement values for the Spark Advance sweep, λ=1.15*

Finally, regarding the flame expansion rate, the three configurations describes an average increasing trend as spark ignition advances, with punctual exceptions for concentric electrode spark plug and SA 8 CAD, for crossflow and SA 12 CAD.

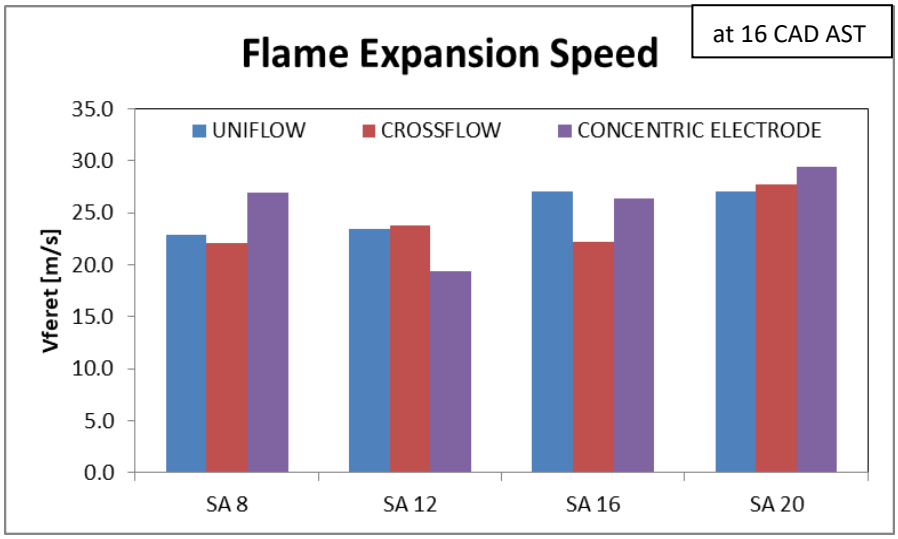


*Figure 4.13, Flame expansion speed values for the Spark Advance sweep, λ=1.15*

### 4.3.2 Effect of Spark Advance for λ=1.30

In the following chapter the analysis of the operative condition for fixed λ=1.30, obtained through a DOI of 30 CAD is reported. The ignition setting range is reduced with respect to the previous cases seen, due to stability issues, similar to the effects observed in [36]. In fact, under these AFR conditions, only two Spark Advances, 12 and 20 CAD, will be analysed.

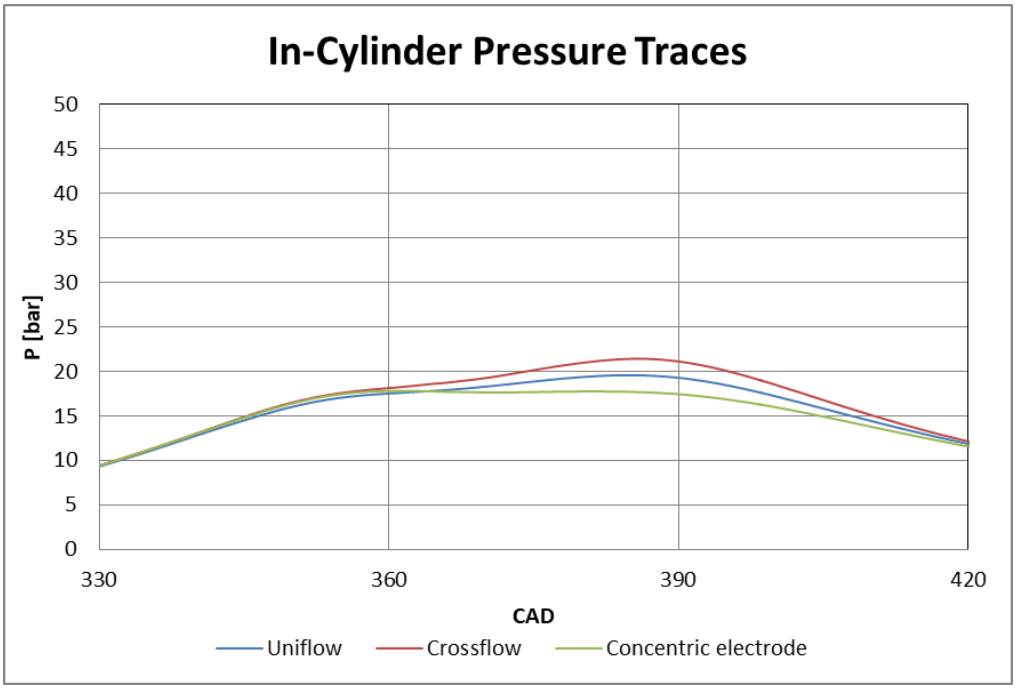


*Figure 4.14, In-cylinder Pressure traces for λ=1.30 and SA 12 CAD*

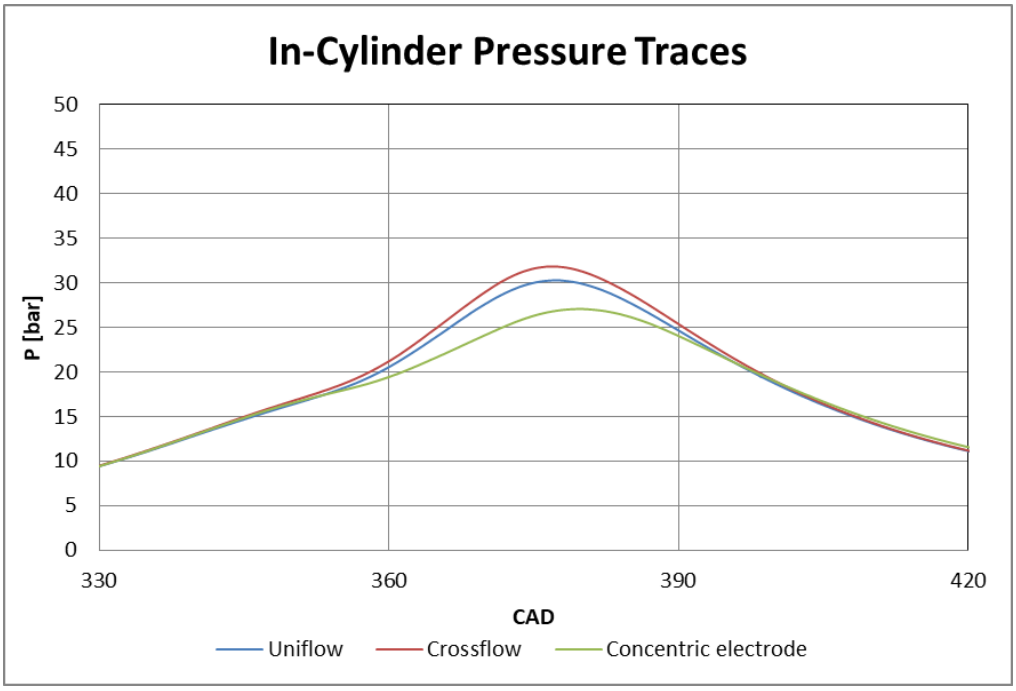


*Figure 4.15, In-cylinder Pressure traces for λ=1.30 and SA 20 CAD*

Observing the in-cylinder pressure traces reported in figures 4.14 and 4.15, it can be seen that, as SA varies, the considerations made in the previous subparagraph are also verified in the present case of analysis. In particular, the pressure peaks are higher for the crossflow configuration while the concentric electrode spark plug presents the lowest pressure levels among the three geometries. The IMEP values, considering an ignition advance of 12 and 20 CAD, undergoes an increase for each spark plug setting, more evident for the concentric geometry (from 5.57 bar with SA 12 CAD to 6.50 bar with SA 20 CAD), as can be seen from figure 4.16. Furthermore, this configuration returns higher $COV_{IMEP}$ values for the most delayed ignition condition (15.7% against 10.4% and 7.6% respectively for uniflow and crossflow configuration); however, cyclic variability generally tends to reduce as ignition is advanced.

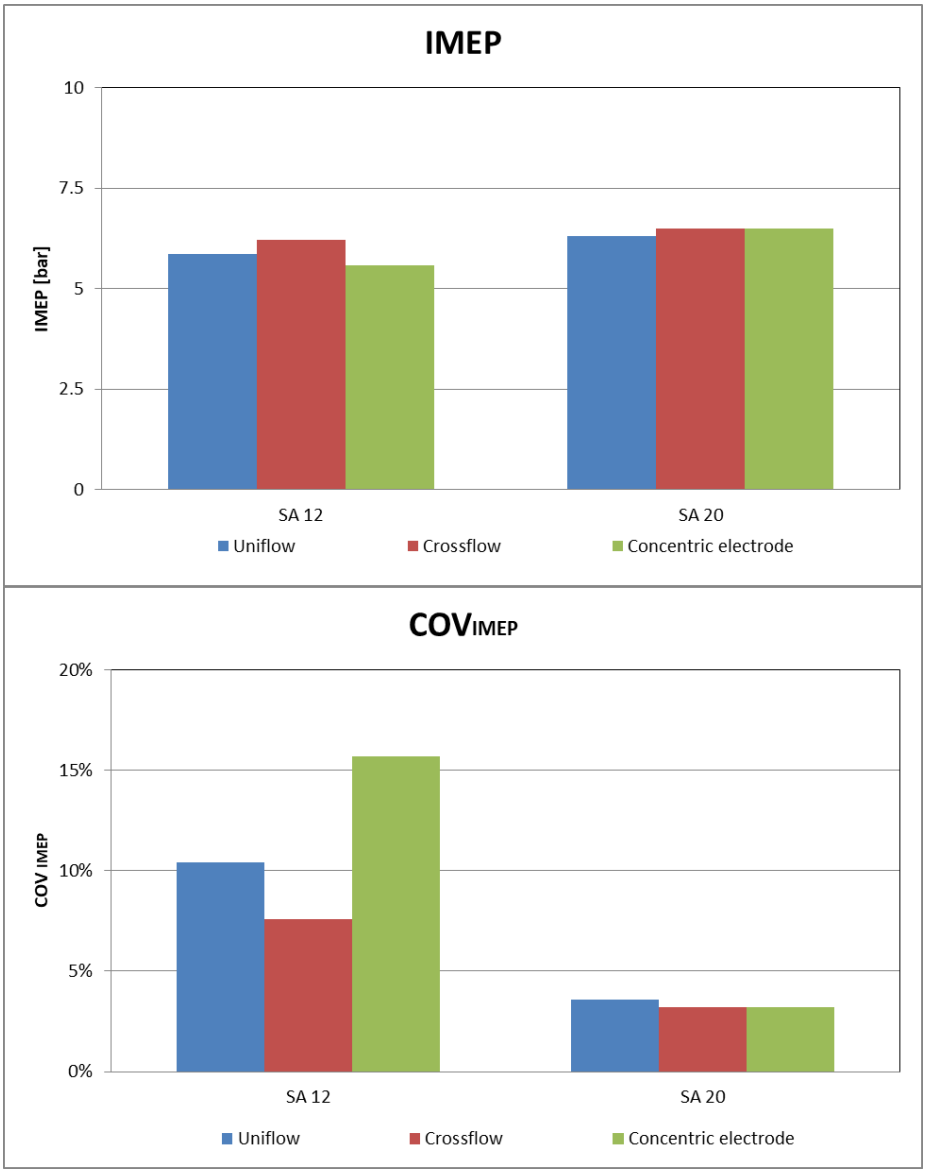


*Figure 4.16, IMEP and $COV_{IMEP}$ values for the Spark Advance sweep, λ=1.30*

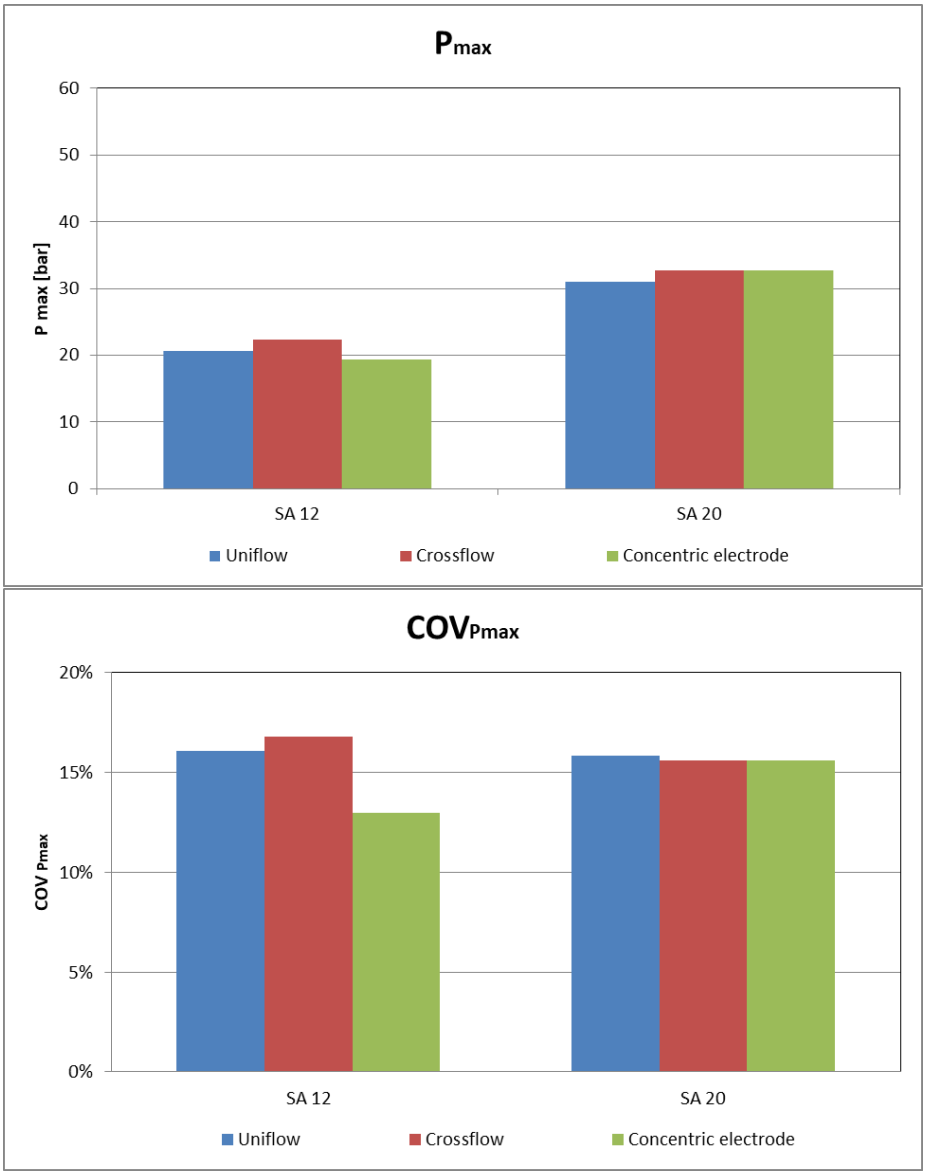


*Figure 4.17, Maximum pressure and $COV_{Pmax}$ values for the Spark Advance sweep, λ=1.30*

It can be seen from figure 4.17 that under the same advance settings, the average maximum pressure is comparable for the three configurations. In terms of $COV_{Pmax}$, a reduction for the uniflow and crossflow geometries from SA 12 to SA 20 CAD BTDC was noted, unlike the concentric configuration for which the cyclic variability tends to increase for anticipated spark ignition timing (passing from $COV_{Pmax}$ 13% to 15,6%).

The VFB traces reported in the figures below shown that for the concentric configuration the combustion rate result to be slower if compared to the other two during all the phases of the combustion process (for example, with a spark timing of 12 CAD, $VFB_{80\%}$ is reached 56.4 CAD AST, while for the uniflow and crossflow geometries this condition occurs respectively 50.8 and 47.2 CAD AST). As expected, the combustion process tends to be faster as the SA increases, as also seen in the previous setting of operating conditions.

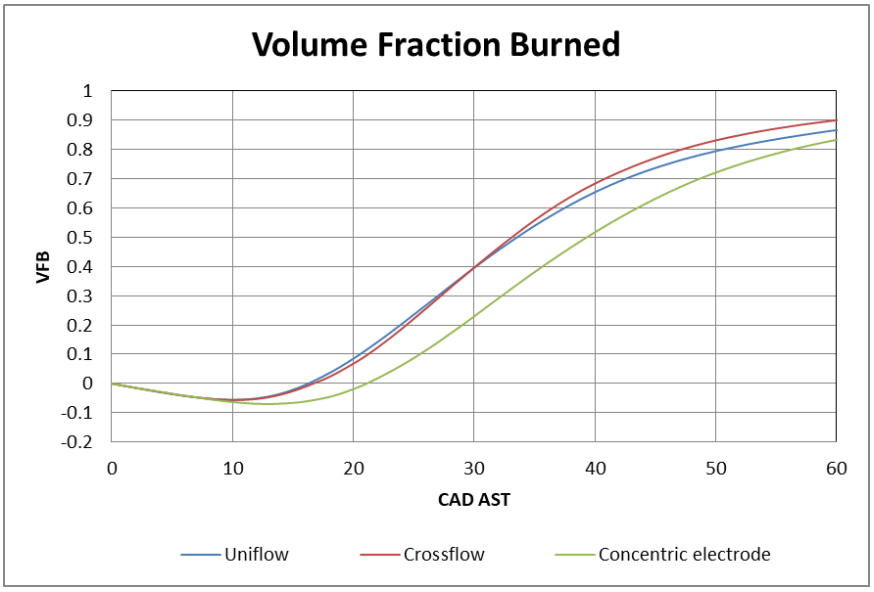


*Figure 4.18, VFB traces for λ=1.30 and SA 12 CAD*

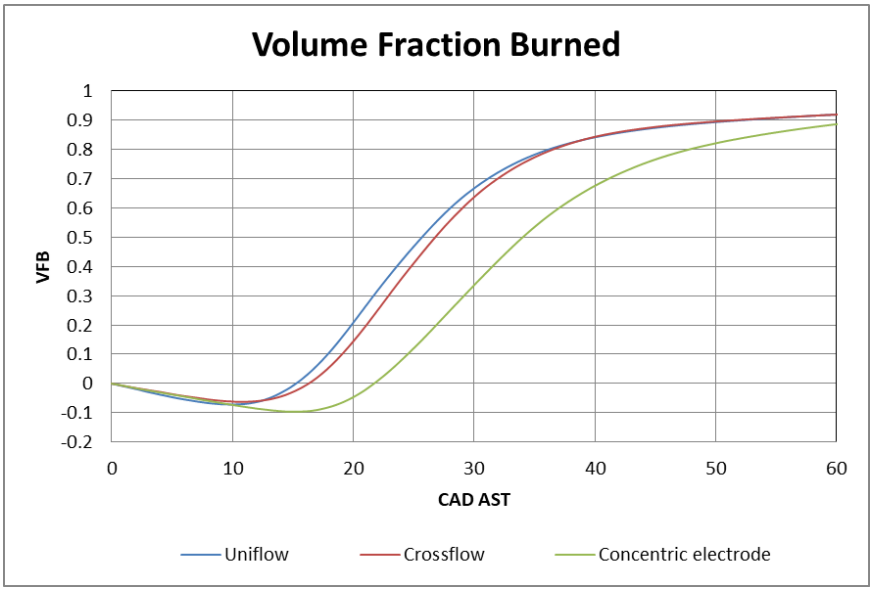


*Figure 4.19, VFB traces for λ=1.30 and SA 20 CAD*

In terms of spatial behaviour of the flame front and kernel formation process, it can be noted looking at the kernel dislocation values reported in the figure 4.20 that it increases considerably with the ignition advance for the concentric electrode spark plug. A slight increase was recorded for the J-type double electrode spark plug in crossflow position; opposite to these trends, the uniflow configuration shows a decreasing evolution of the displacement. The expansion speed also tends to slightly and comparably grow with SA for the three different ignition geometries, as shown in figure 4.21.

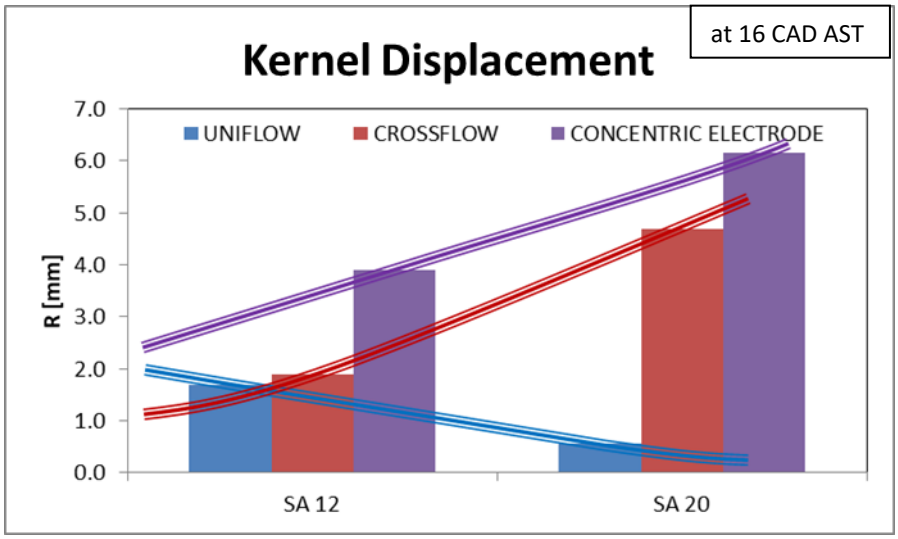


*Figure 4.20, Kernel displacement values for the Spark Advance sweep, λ=1.30*

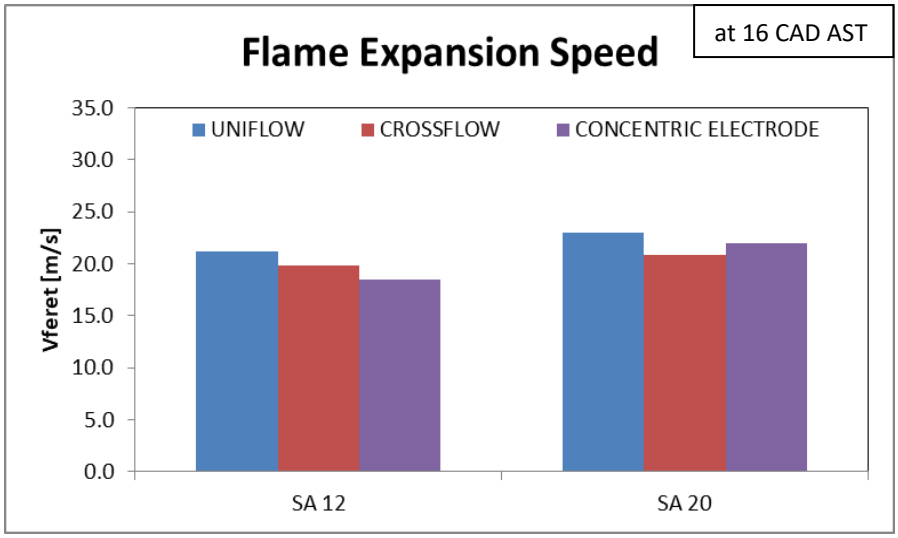


*Figure 4.21, Flame expansion speed values for the Spark Advance sweep, λ=1.30*

## 4.4Effect of Air-Fuel Ratio

### 4.4.1 Effect of Air-Fuel Ratio for SA 12 CAD

Starting from this chapter, the analysis will be focused on the influence of the Air-Fuel Ratio on engine performance and optical behaviour of combustion process. The cases examined regard a λ value varying from 1.00 to 1.30 with a sweep of 0.15 and a fixed SA 12 CAD. The main purpose at the base of fixing the ignition setting is to ensure that flame kernel initiation occurs in similar conditions with respect to tumble and turbulence intensity. This type of solution emphasizes the effects of the chemical composition, thus the reactivity of the mixture and time characteristics as well as the influence of spark plug orientation with respect to the interaction with fluid motion.

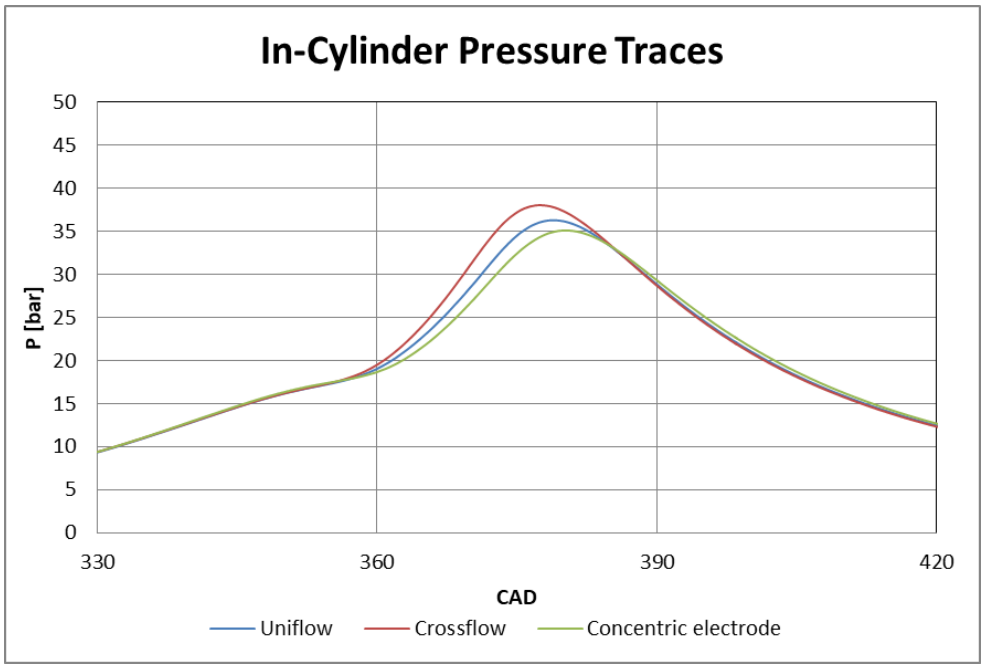


*Figure 4.22, In-cylinder Pressure traces for λ=1.00 and SA 12 CAD*

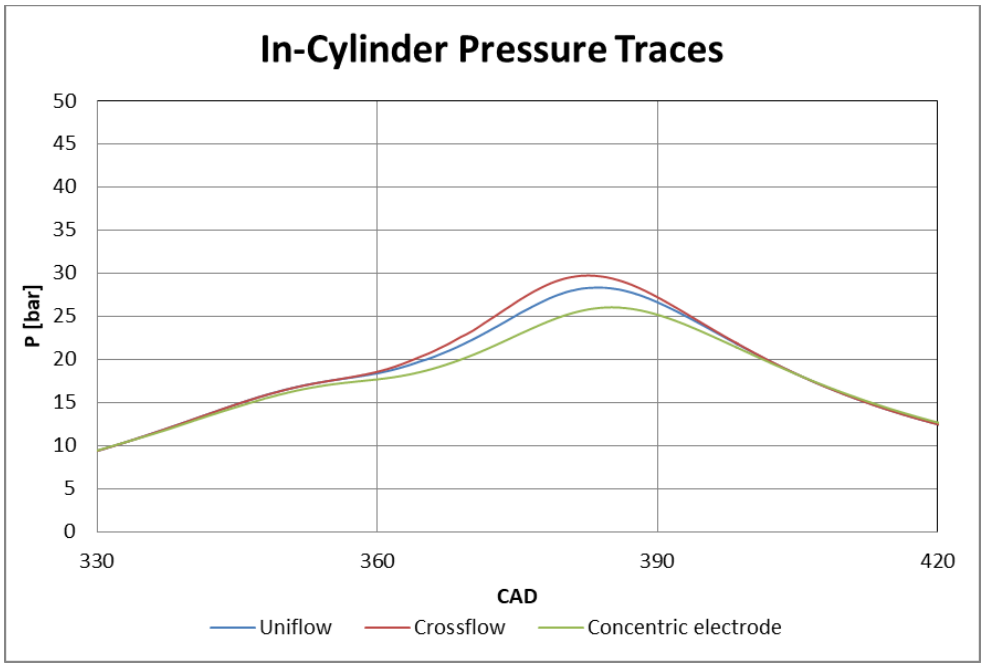


*Figure 4.23, In-cylinder Pressure traces for λ=1.15 and SA 12 CAD*

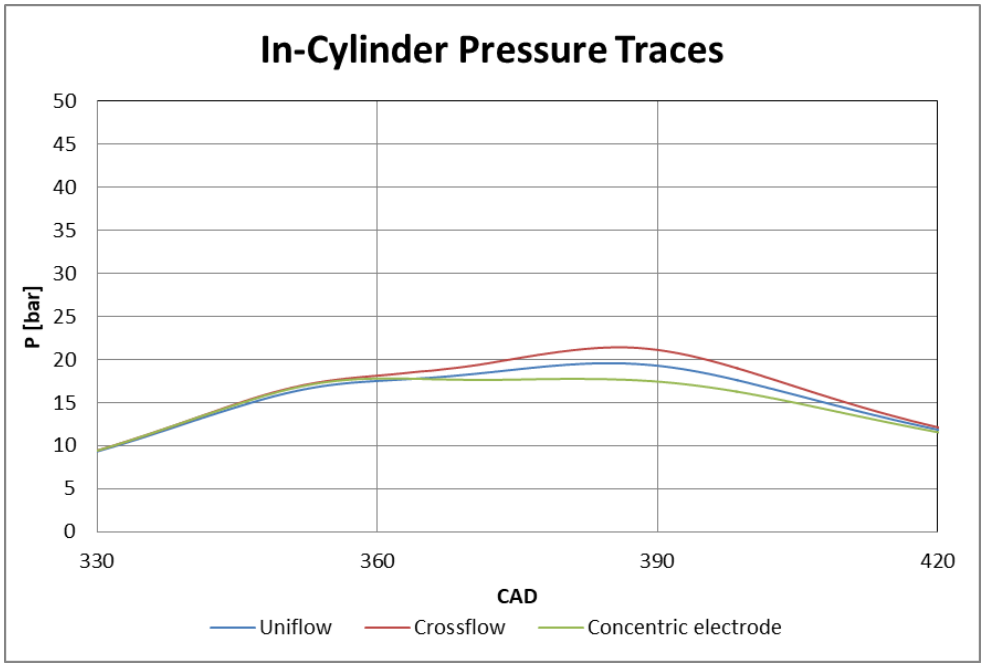


*Figure 4.24, In-cylinder Pressure traces for λ=1.30 and SA 12 CAD*

The average in-cylinder pressure traces (figures 4.22-4.23-4.24) show a well-defined trend, in fact, the crossflow configuration seems to feature the higher peak pressure for each case, followed by the uniflow orientation and finally the concentric electrode spark plug configuration, which achieves the most contained pressure level during all the cycle. As expected, with richer air-fuel mixtures the IMEP tends to increase (figure 4.25) as a direct consequence of larger quantity of injected fuel. Furthermore, for the leanest blend the $COV_{IMEP}$ tends to increase as a direct result of slower combustion process (longer chemical time scales characteristic for the cases with lean mixtures) with increased effects of turbulence-flame interactions. Looking at the reported values, it can be seen that for the operative condition with the leanest mixture the concentric electrode configuration shows the highest cyclic variability (around 15.7%) if compared with the other two (respectively 10.4% for uniflow and 7.6% for crossflow). For the Air-Fuel Ratio λ=1.15 and λ=1.00, a different situation is evident, in fact for the latter there is a comparable situation between the three configuration in terms of $COV_{IMEP}$.

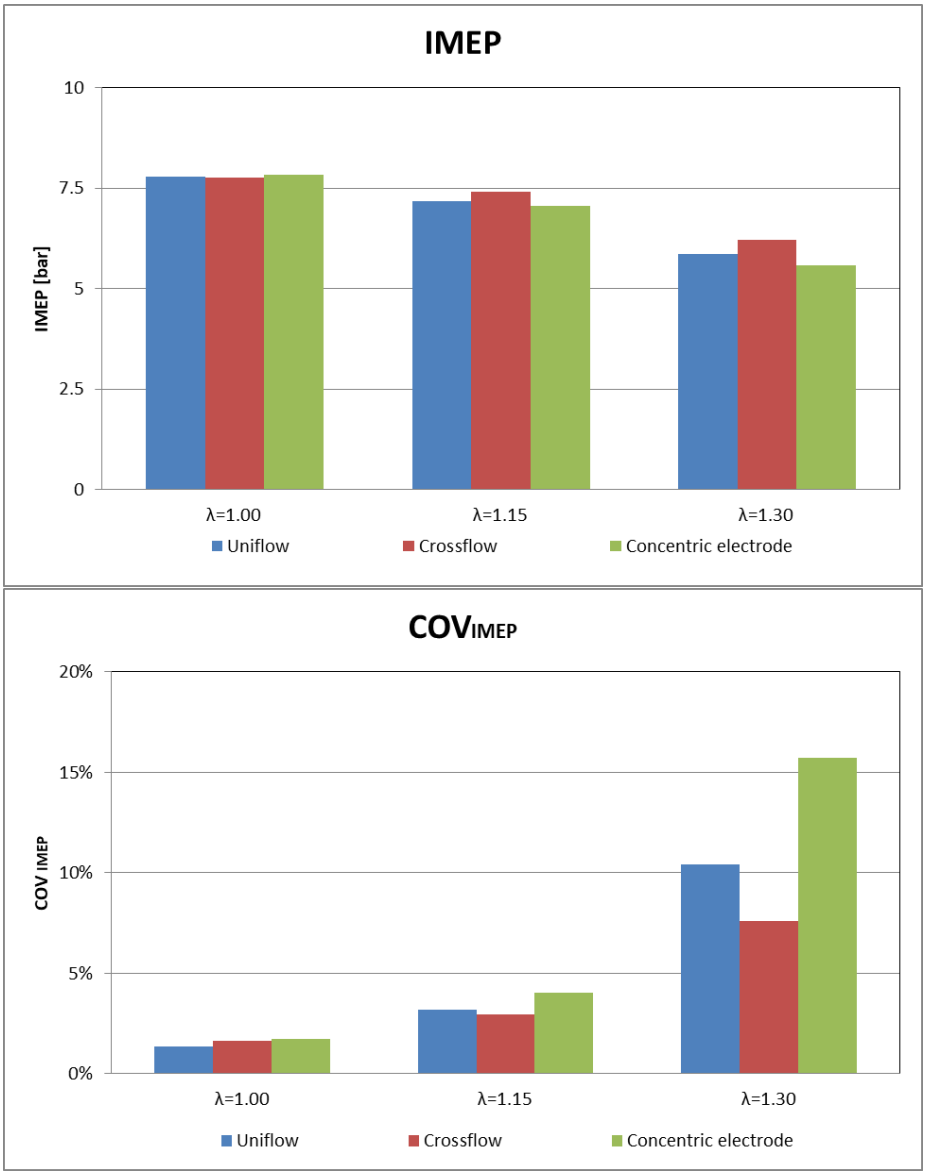


*Figure 4.25, IMEP and $COV_{IMEP}$ values for the AFR sweep, SA 12 CAD*

$COV_{Pmax}$ (figure 4.26) featured relatively higher values if compared to the $COV_{IMEP}$ parameter, this difference is strongly related to the different logic of calculation behind these two parameters (IMEP is integrated over 720 CAD, thus reducing the actual influence of combustion stability itself, while the $COV_{Pmax}$ is referred only to the single value of peak pressure on 200 cycles). Other phenomena related to the optical engine characteristics (listed in the Chapter 2 in the dedicated paragraph) can also contribute to variations in terms of cyclic repeatability (e.g. the large top-land region volume can significantly influence the final part of the combustion process). Looking at the absolute values, for the leanest blend this value stands at more than 12% (with a peak of almost 16.8% for the crossflow configuration) and decreases for λ=1.15 and finally for the stoichiometric operative condition. An overall trend of highest $COV_{Pmax}$ for the concentric electrode spark plug can be observed (the only exception is for λ=1.30).

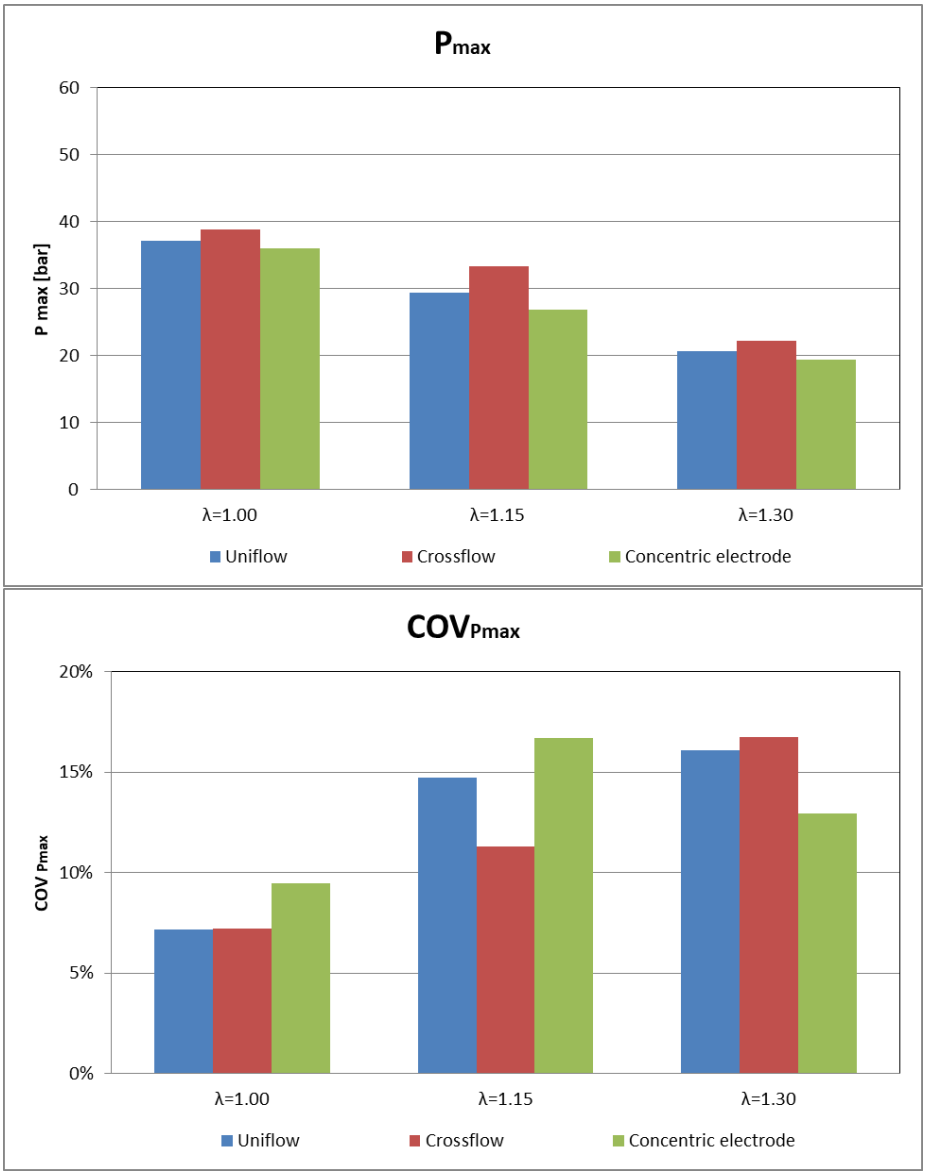


*Figure 4.26, Maximum pressure and $COV_{Pmax}$ values for the AFR sweep, SA 12 CAD*

The in-cylinder VFB traces show an increasing burning rate as the duration of injection was increased (figures 4.27-4.28-4.29). It is possible to observe a predominance of crossflow and uniflow configurations in terms of higher flame front propagation speed with respect to the concentric electrode geometry. In terms of burned volume, the location of 80% (representative of $MFB_{50\%}$) is reached in comparable times by the first two configurations (respectively around 50 CAD AST for λ=1.30, 35 CAD AST for λ=1.15 and 29 CAD AST for the stoichiometric operative condition) while the gap with the concentric electrode geometry tends to increase when moving from stoichiometric AFR to λ=1.15-1.30 conditions (from 3 CAD about to 6 CAD). Finally, as expected, with a leaner charge, the duration of the early stage of flame front development (0-30% VFB corresponding to 0-10% MFB) is extended from 27 CAD for λ=1.30 to 20 CAD for λ=1.15 and 17 CAD for the stoichiometric condition.

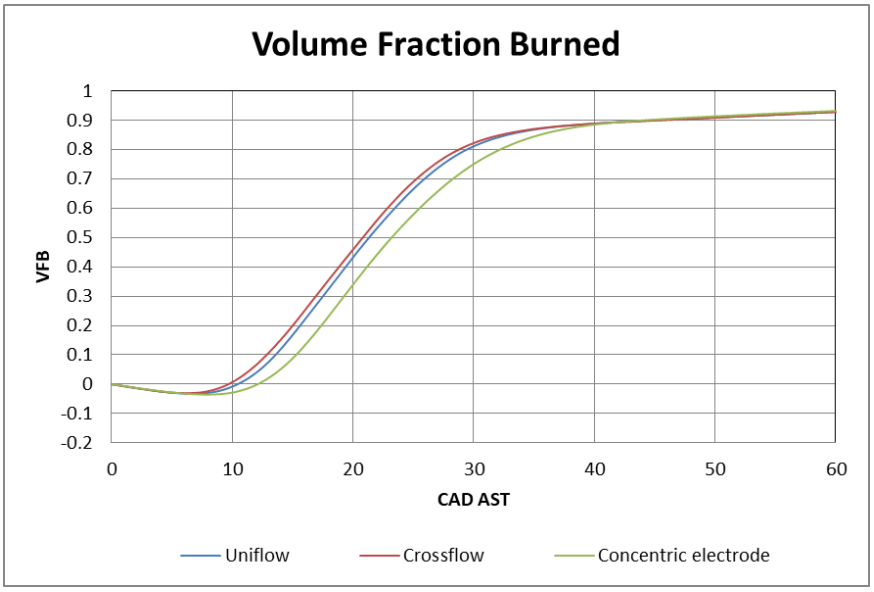


*Figure 4.27, VFB traces for λ=1.00 and SA 12 CAD*

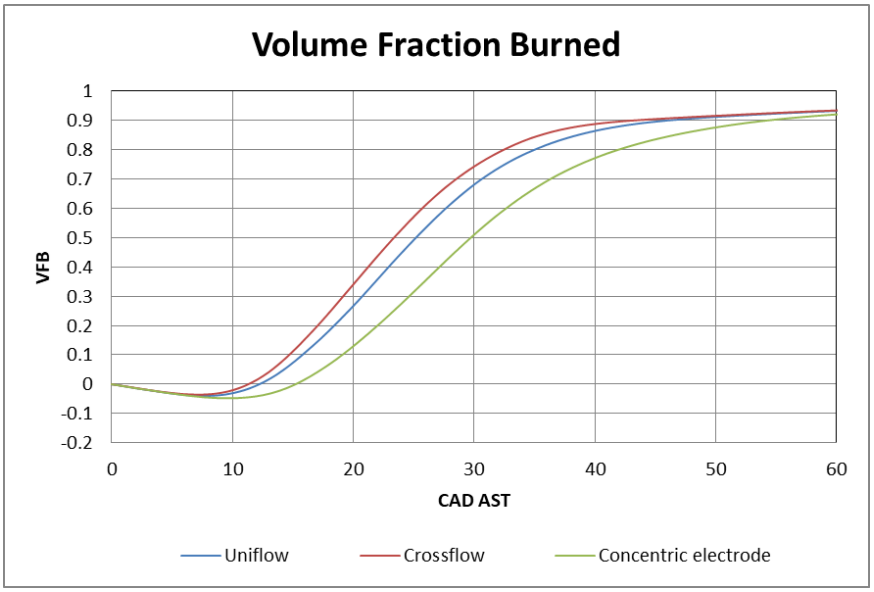


*Figure 4.28, VFB traces for λ=1.15 and SA 12 CAD*

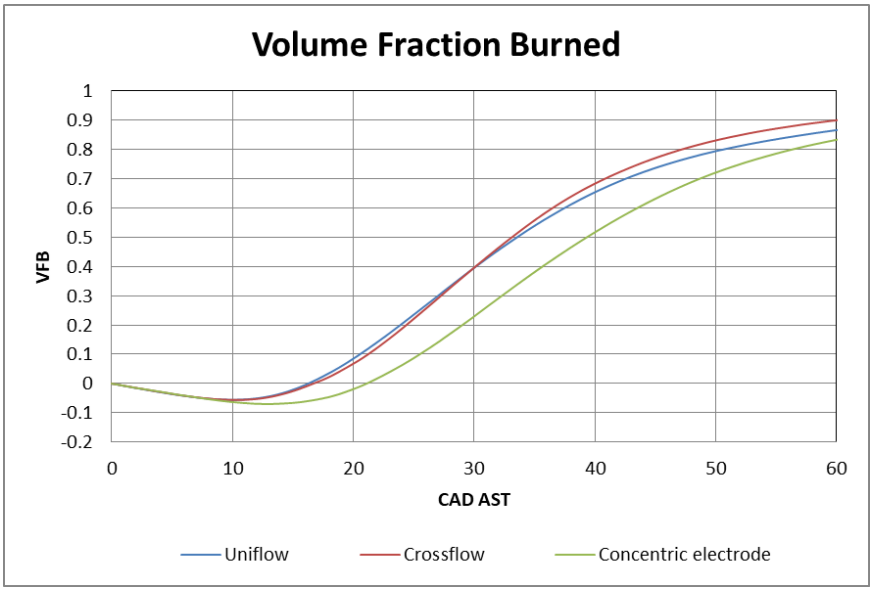


*Figure 4.29, VFB traces for λ=1.30 and SA 12 CAD*

By the figure 4.30, it can be noted that, with respect to the flame front propagation, the variation of the AFR generates a very similar influence to that previously seen for the effect of Spark Advance in the paragraph 4.3. In fact, the concentric electrode configuration shows a kernel displacement trend with a peak in correspondence with λ=1.15 setting; this situation can also be found in the uniflow geometry, although the values are more contained. On the contrary, for this charging condition, a minimum point is noted in the evolution of R for crossflow.

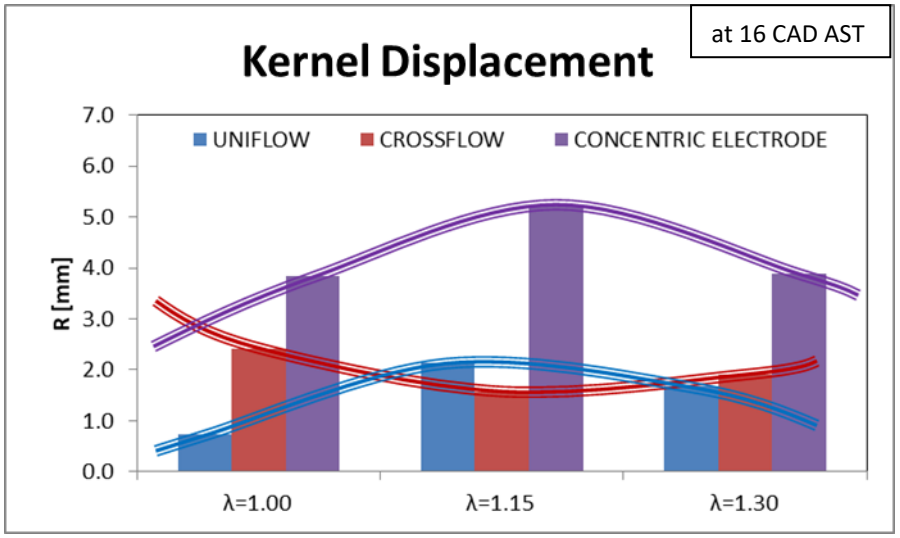


*Figure 4.30, Kernel displacement values for the AFR sweep, SA 12 CAD*

Flame expansion speed is maximised for λ=1.15 in the uniflow and crossflow configurations, while the concentric electrode spark plug exhibits a decreasing $V_{Feret}$ trend when switching from stoichiometric to leaning mixtures, as can be seen in figure 4.31.

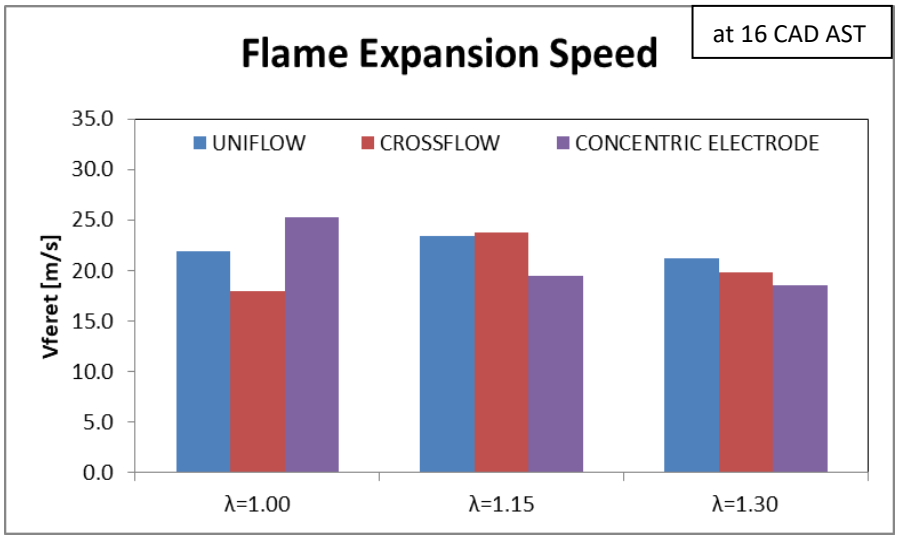


*Figure 4.31, Flame expansion speed values for the AFR sweep, SA 12 CAD*

### 4.4.2 Effect of Air-Fuel Ratio for SA 20 CAD

In order to further investigate the effect of blend composition on the combustion process, a second case with an ignition advance set at 20 CAD and λ varying between 1.15 and 1.30 was analysed. Once again, the study starts by comparing the average in-cylinder pressure cycles shown in the figures 4.32-4.33.

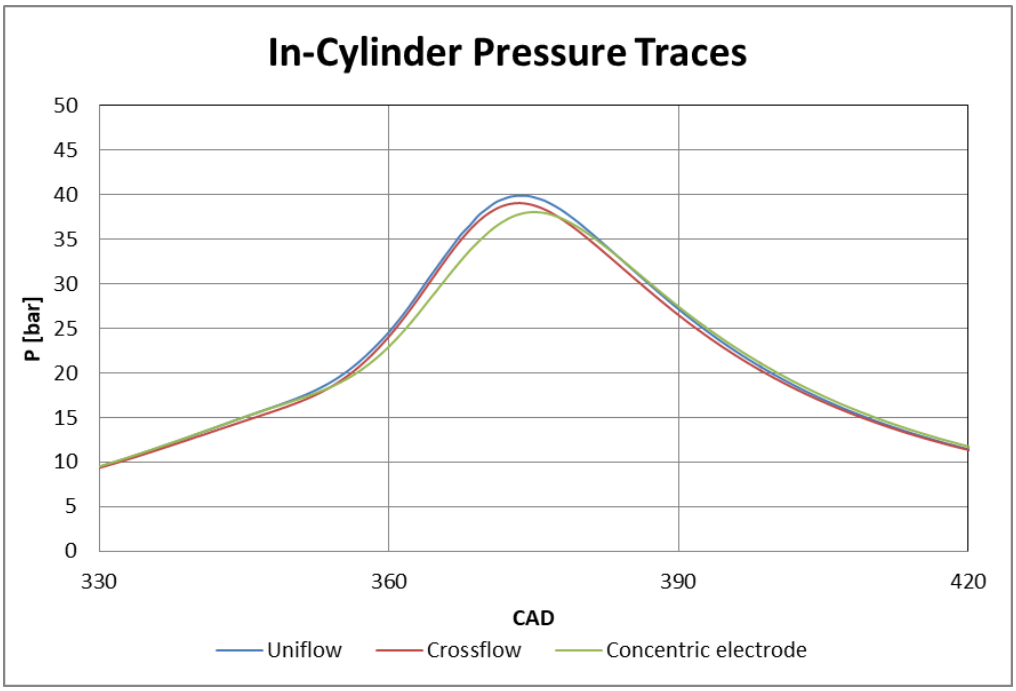


*Figure 4.32, In-cylinder Pressure traces for λ=1.15 and SA 20 CAD*

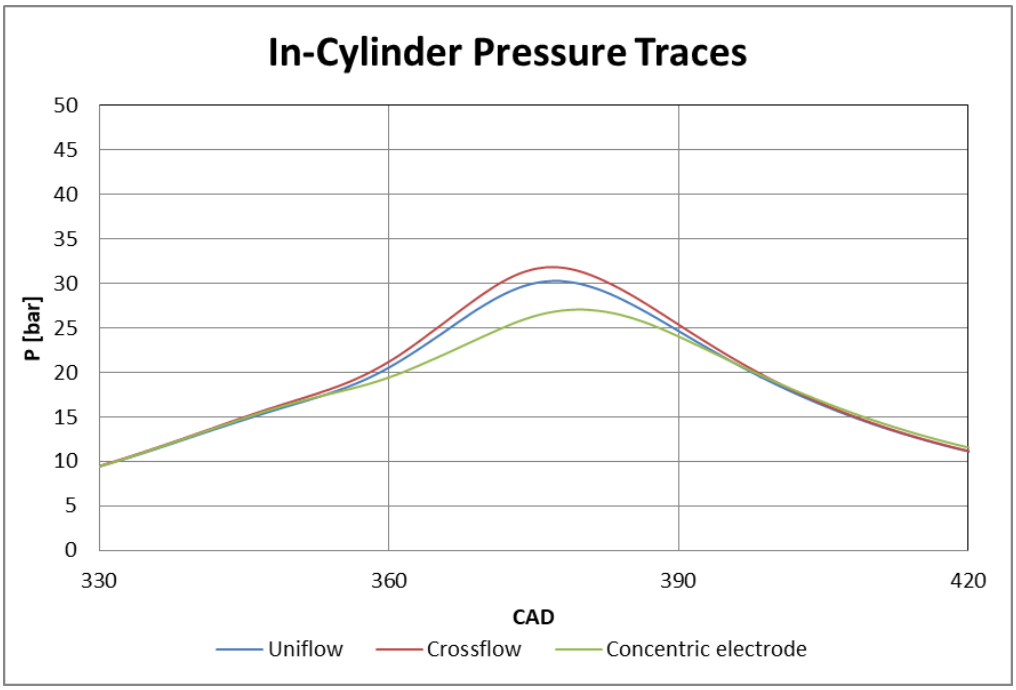


*Figure 4.33, In-cylinder Pressure traces for λ=1.30 and SA 20 CAD*

Observing the pressure traces, no well-defined trend was noted. Peak pressure values appear to be influenced in a contained way by the uniflow and crossflow configurations, alternating as the AFR increases; overall the concentric electrode configuration features lower peak pressure compared to the other two orientations, confirming the observations in the cases already seen. In terms of IMEP, the increase of the DOI from 30 to 34 CAD results in a moderate increment (from around 6.5 bar to slightly above 7 bar, as can be seen in figure 4.34) and the three geometries seem comparable as regards absolute values.

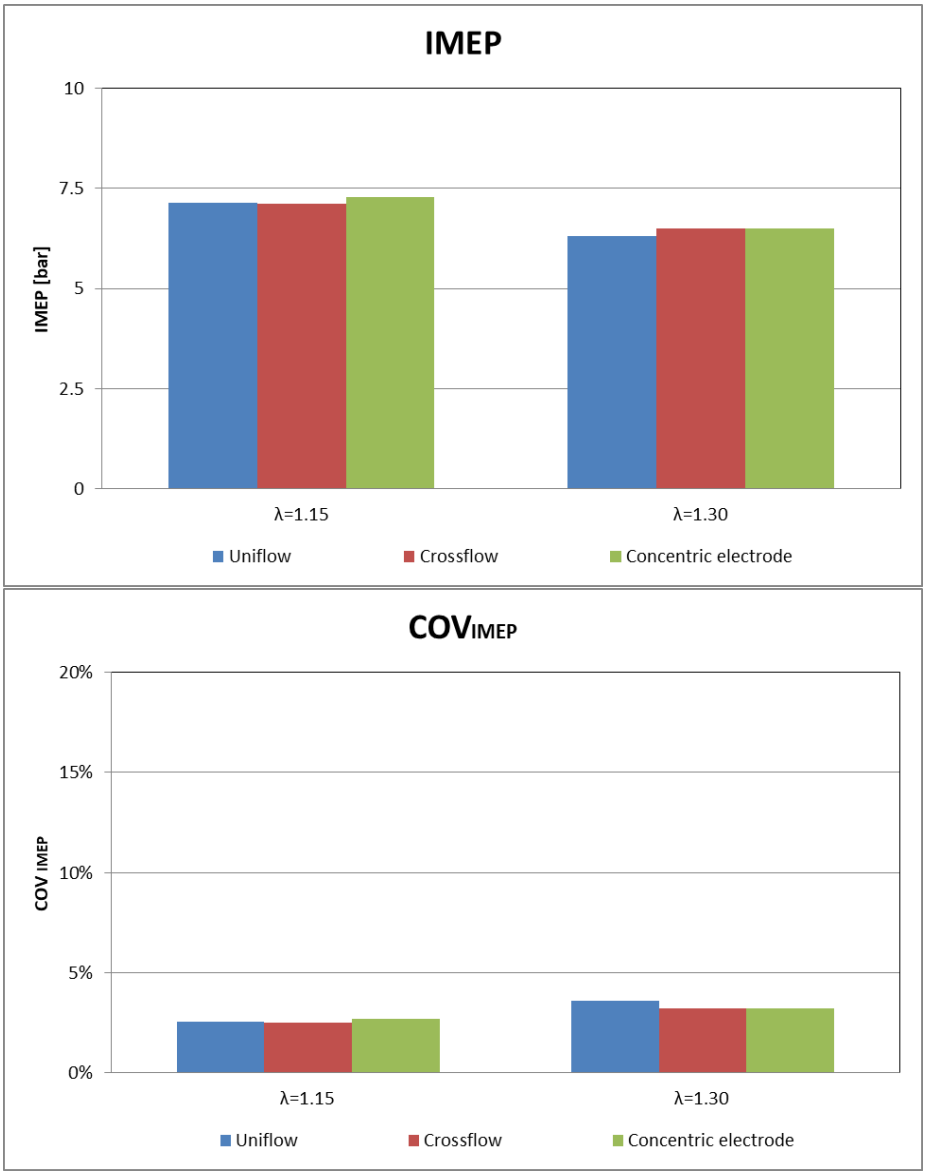


*Figure 4.34, IMEP and $COV_{IMEP}$ values for the AFR sweep, SA 20 CAD*

A comparable scenario can also be found in terms of $COV_{IMEP}$, which tends to slightly increase passing from λ=1.15 to λ=1.30 (from about 2.5% to 3.5%). The average maximum pressure obviously tends to increase enriching the mixture, as can be seen in the figure 4.35 and from the pressure cycles previously shown; in particular, the increment is more pronounced for the crossflow configuration where it rises from about 33 bar to 44 bar.

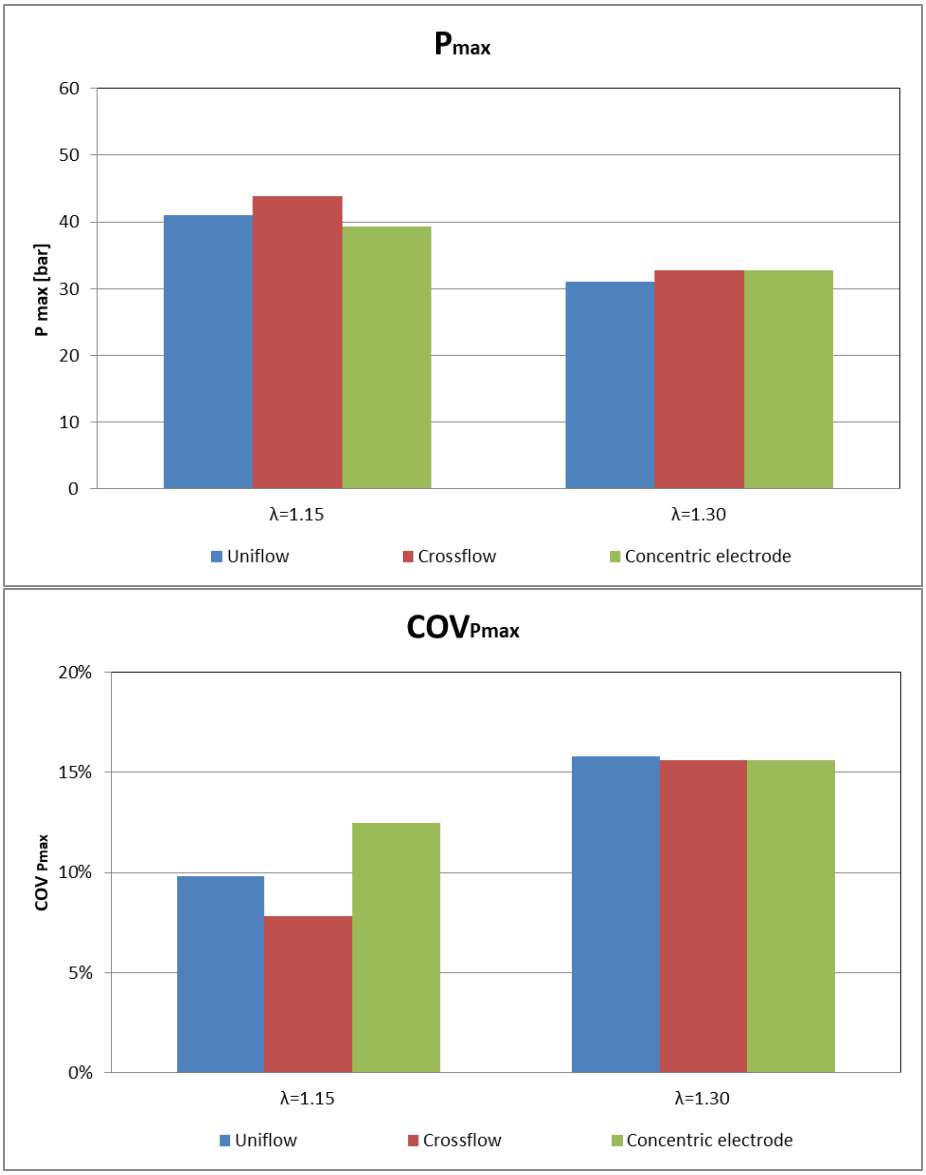


*Figure 4.35, Maximum pressure and $COV_{Pmax}$ values for the AFR sweep, SA 20 CAD*

Figure 4.35 shows that, as the AFR grows, there is an increasing trend in $COV_{Pmax}$ which for λ=1.30 tends to stabilise for the three configurations at around 16%, while for the most enriched mixture condition the concentric electrode spark plug shows an higher value compared with the remaining two orientations (respectively 12.5%, 9.8% and 7.8%).

Looking at the evolution of the combustion process, which can be deduced from the VFB trends shown in figures 4.36 and 4.37, it can be seen that there is no defined trend for injection duration of 34 CAD, where what stands out is exclusively a faster combustion for crossflow than uniflow and concentric electrode configurations. By increasing the Air-Fuel Ratio, the two different orientations of the J-type double electrode spark plug follow comparable trends reaching $VFB_{80\%}$ around 36 CAD AST with a positive gap of about 12 CAD compared to the concentric geometry.

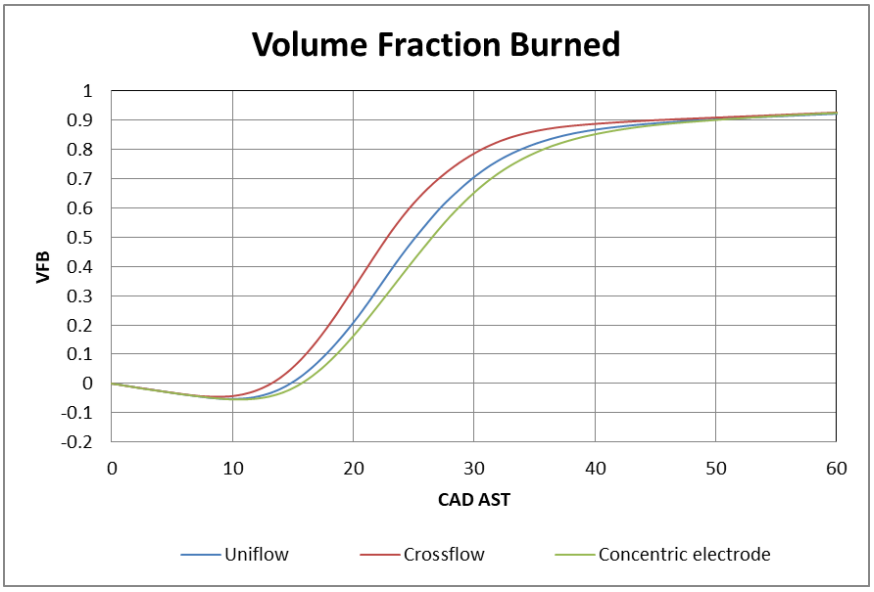


*Figure 4.36, VFB traces for λ=1.15 and SA 20 CAD*

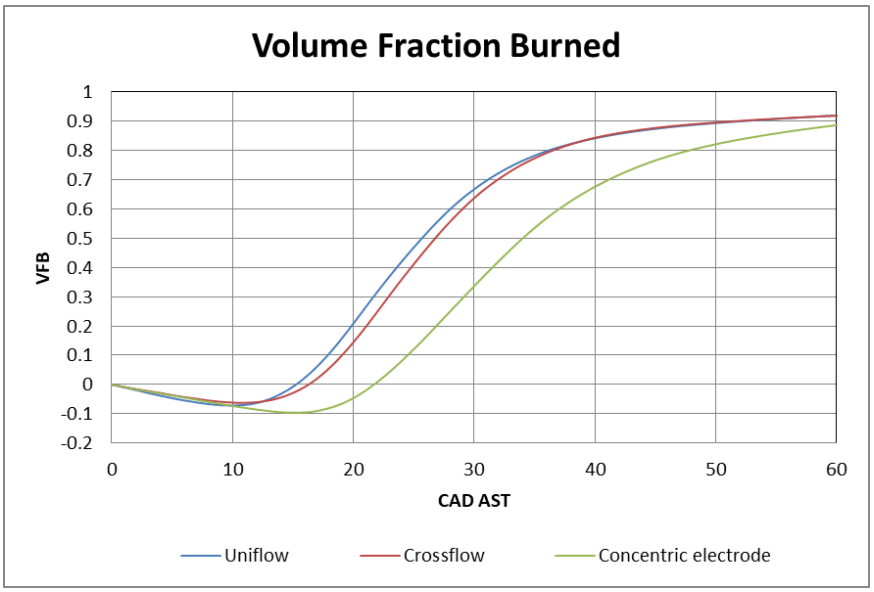


*Figure 4.37, VFB traces for λ=1.30 and SA 20 CAD*

Results from the optical analysis show increasing R trends (figure 4.38) for the crossflow and concentric electrode configurations, with the latter having a steeper slope. In contrast, uniflow presents declining but almost comparable values as the AFR varies. An increase in flame speed due to mixture enrichment is also recorded, but the levels achieved are comparable between the various configurations (aroud 20 m/s for DOI 30 and 30 m/s for DOI 34) as can be seen from figure 4.39.

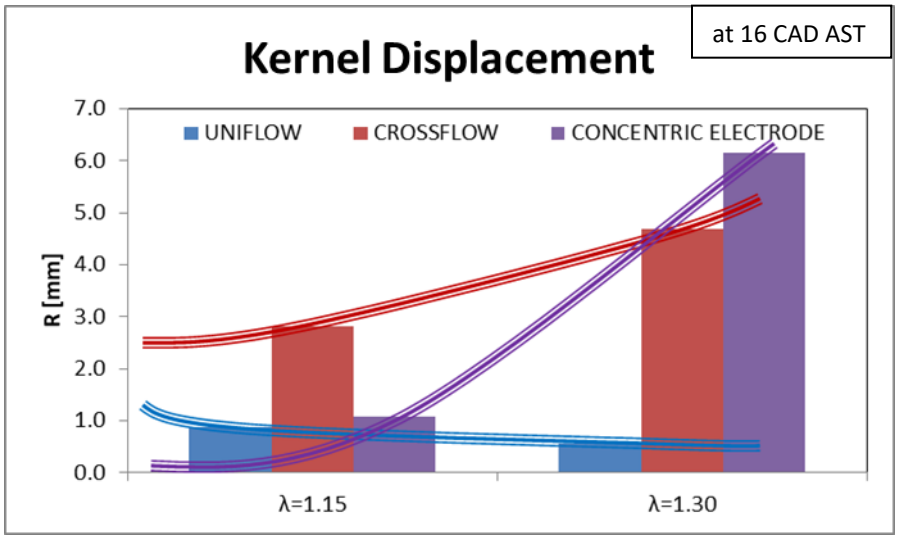


*Figure 4.38, Kernel displacement values for the AFR sweep, SA 20 CAD*

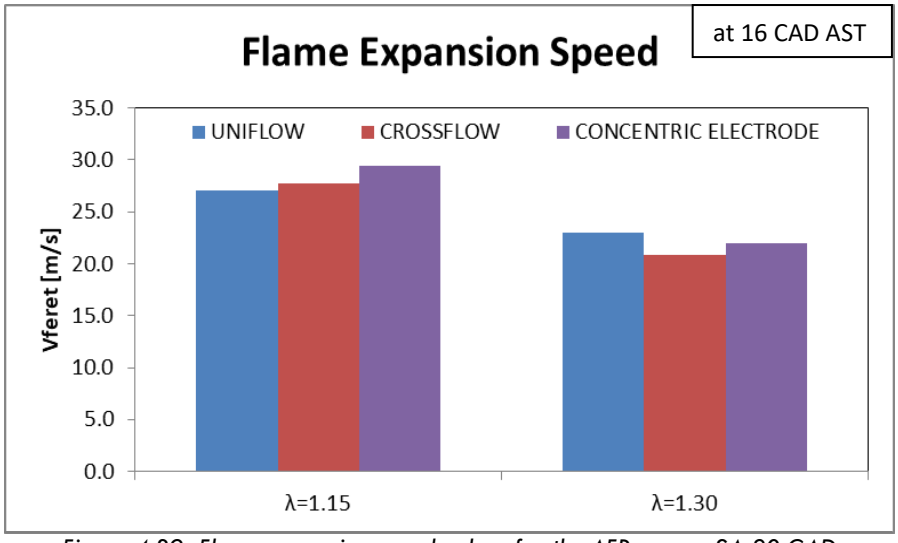


*Figure 4.39, Flame expansion speed values for the AFR sweep, SA 20 CAD*

## 4.5Effect of Engine Load

### 4.5.1 Effect of Engine Load for SA 12 CAD

Next step of the research activity was to analyse how partialized engine load levels affect the combustion process in terms of both cyclic variability and flame kernel formation and propagation for the different configuration and spark plug geometries examined in this study. Acting on the throttle valve opening level it was possible to set different intake pressures of 0.50, 0.75 and 1.00 bar (WOT); Spark Advance was fixed to 12 CAD while DOI has been varied from 18 to 30 and 39 CAD respectively to ensure to have a stoichiometric mixture in each case. The average pressure cycles compared for the three examined spark plug geometries are shown in figures 4.40-4.42.

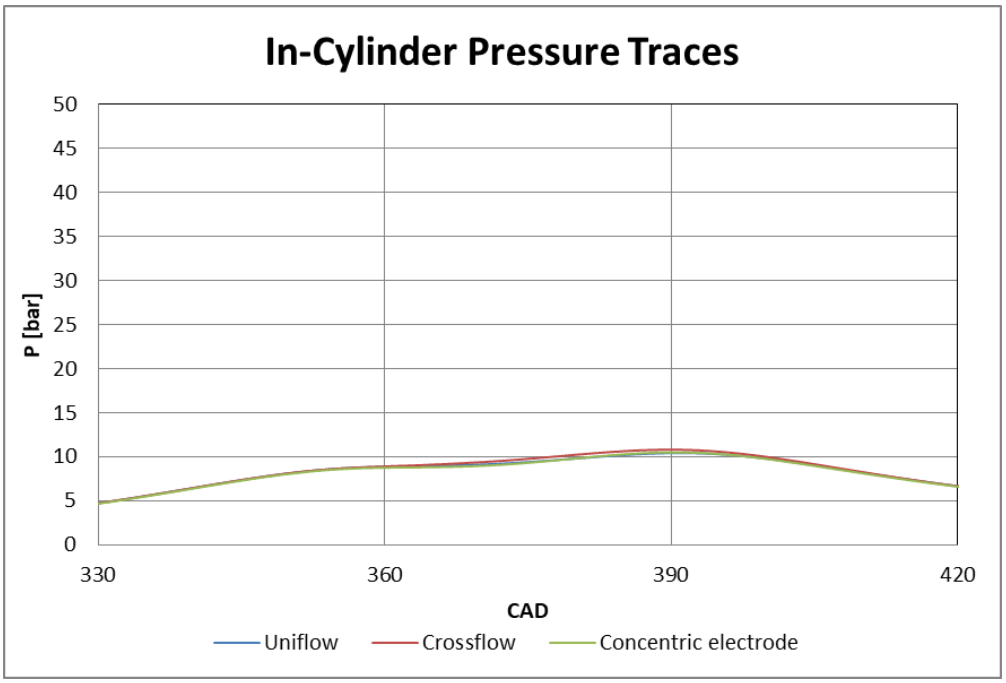


*Figure 4.40, In-cylinder Pressure traces for $P_{intake}$=0.50 bar and SA 12 CAD*

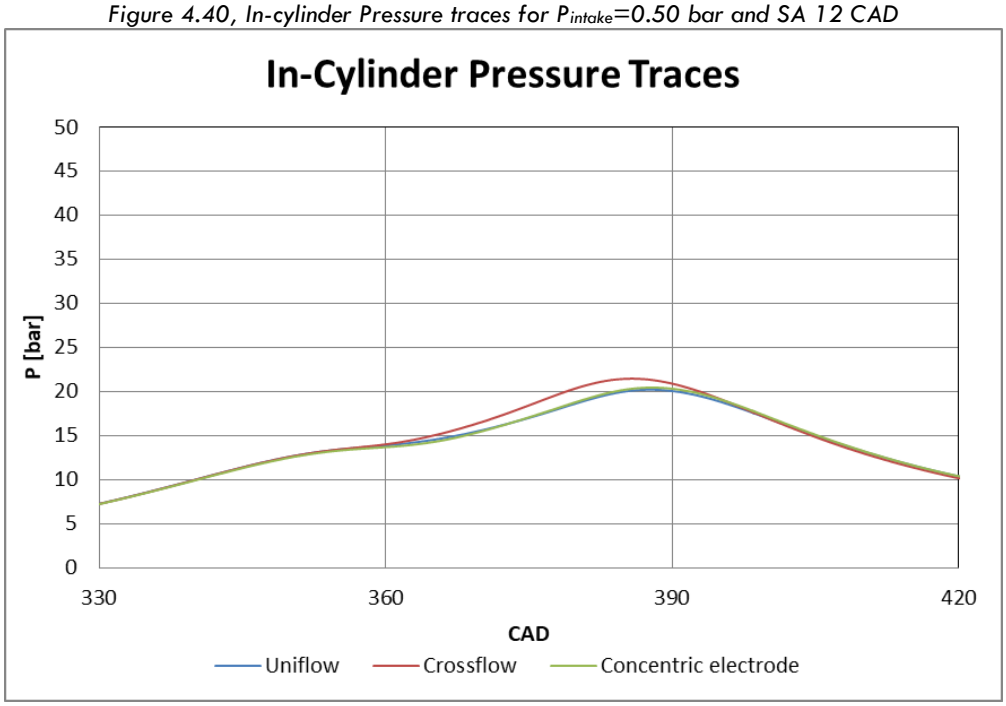


*Figure 4.41, In-cylinder Pressure traces for $P_{intake}$=0.75 bar and SA 12 CAD*

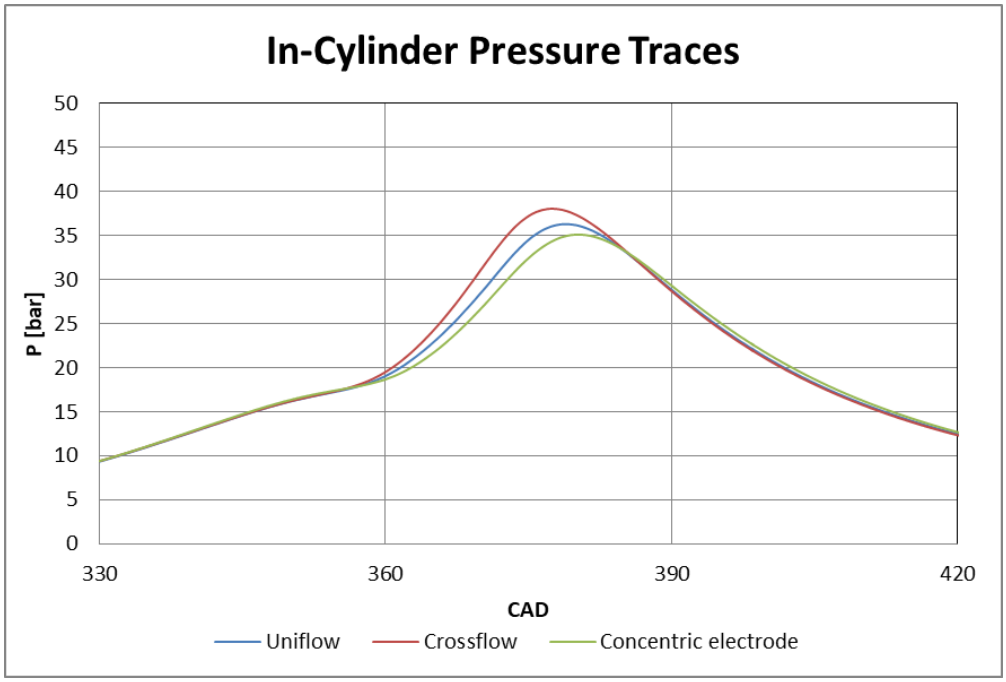


*Figure 4.42, In-cylinder Pressure traces for $P_{intake}$=1.00 bar and SA 12 CAD*

An increase of the gap among the three spark plug geometries as intake pressure grows is noted. Indeed, the reduction of engine load, in terms of $P_{intake}$, results in a combustion process characterised by more stable organized flow and consequently better repeatability. However, the crossflow orientation exhibits higher peak pressures than the remaining configurations under each loading condition. Observing the IMEP trends in Figure 4.42, it can be seen that the latter tends to increase with the load and, in each intake pressure operating condition, it settles at comparable values among the three ignition configurations (around 3 bar for $P_{intake}$=0.50 bar, 5.7 bar for $P_{intake}$=0.75 bar and 7.8 in WOT setting). From the same figure, it can be seen that $COV_{IMEP}$ tends to reduce as the engine inlet pressure increases; this reduction is particularly marked for the concentric electrode configuration passing from 0.50 to 0.75 bar (from 10.2% to 2.2%) and for the uniflow orientation from 0.75 to 1.00 bar (from 6.1% to 1.4%). In WOT operating condition, values stabilise at around 1.5% for each ignition geometry.

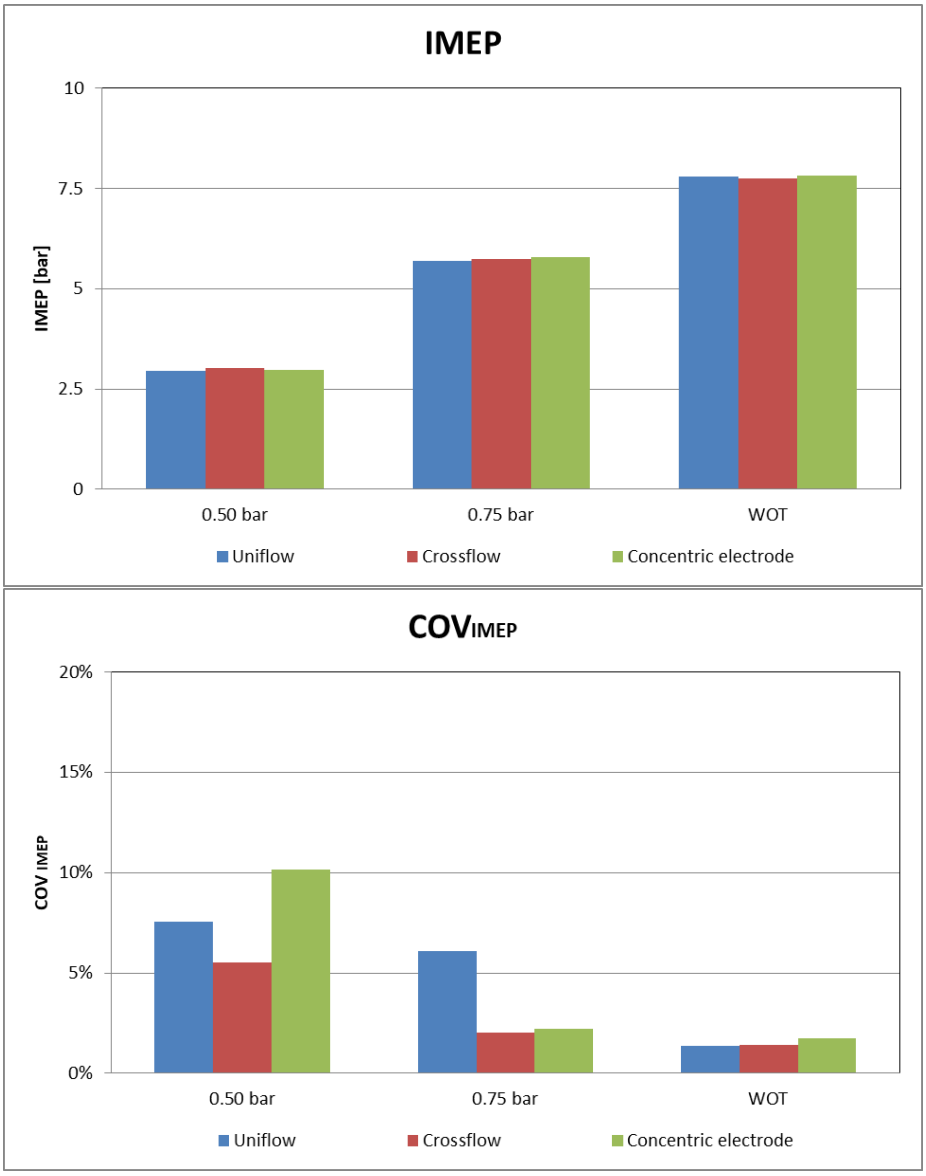


*Figure 4.42, IMEP and $COV_{IMEP}$ values for the $P_{intake}$ sweep, SA 12 CAD*

Obviously, load increasings also lead to average maximum pressure increments (figure 4.43), confirming higher peak values for the crossflow configuration among the three, as seen from in-cylinder pressure cycles. However, at equal $P_{intake}$, there is good comparability between the various spark plug settings. For each of the latter, $COV_{Pmax}$ decreases passing progressively towards increasing values of intake pressure, except for uniflow in the transition from 0.50 to 0.75 bar. In WOT condition, the concentric electrode spark plug exhibits higher values compared to the others (9.5% compared to about 7% for uniflow and crossflow).

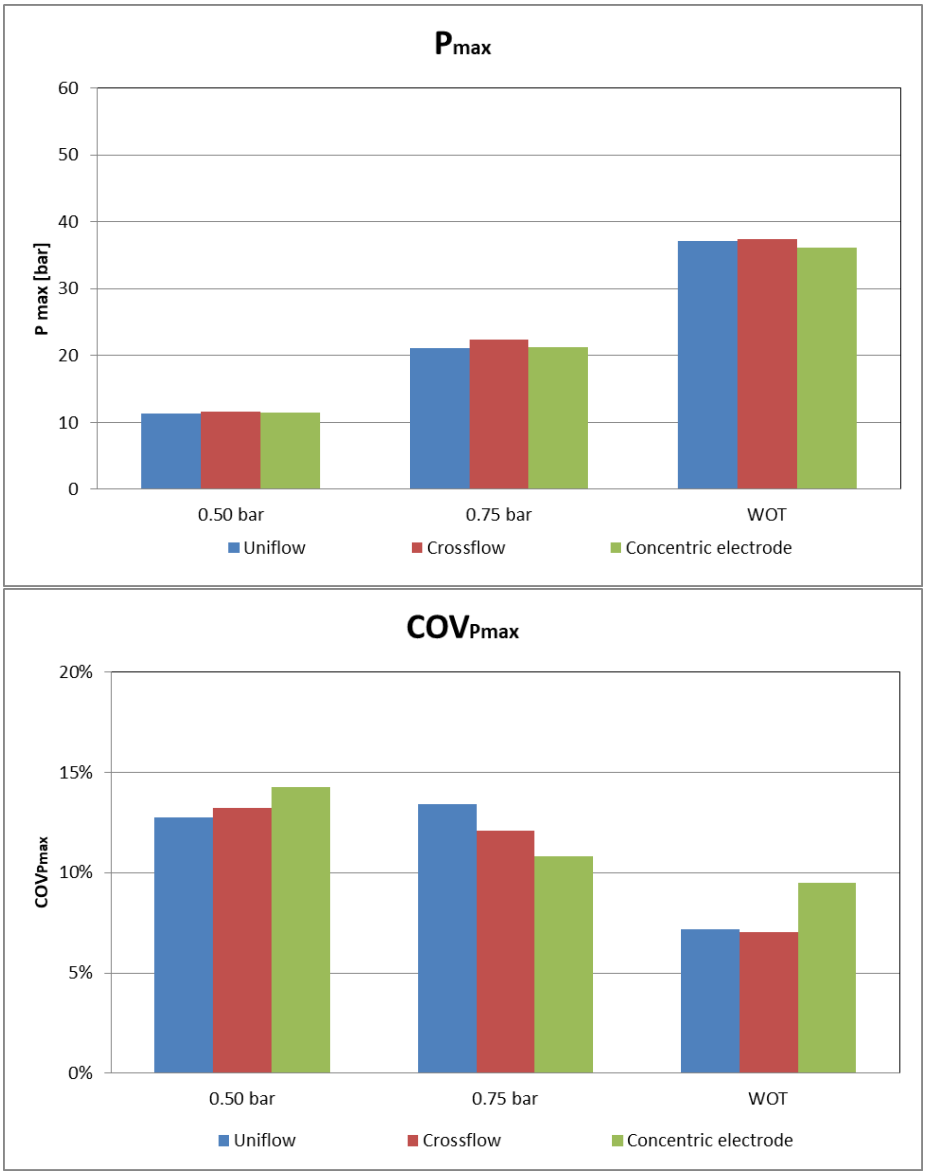


*Figure 4.43, Maximum pressure and $COV_{Pmax}$ values for the $P_{intake}$ sweep, SA 12 CAD*

Observing the Volume Fraction Burned trend reported in figures 4.44-4.46, no particularly defined trend can be noted; the concentric electrode configuration shows a faster burn with respect to the others for $P_{intake}$=0.50 bar ($VFB_{80\%}$ at around 47 CAD AST). Probably the presence of the J-type electrode hindering the air inlet flow, combined with a very low intake pressure leads to a less organised and stable motion for crossflow and uniflow orientations. For $P_{intake}$=0.75-1.00 bar, on the other hand, the most rapid evolution was recorded for crossflow configuration (followed by uniflow) with $VFB_{80\%}$ reached at about 41 and 28 CAD AST respectively. In this case, therefore, the spark plug geometry, combined with a higher engine load, promotes the development of tumble and swirl motions; these aforementioned reasons also motivate a gap between the three configurations that tends to be higher for minimum and maximum intake pressures.

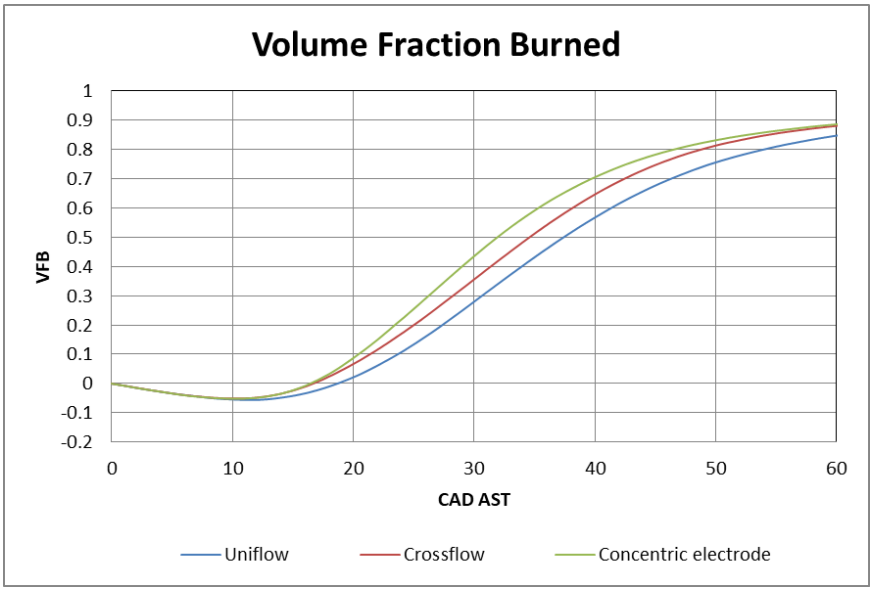


*Figure 4.44, VFB traces for $P_{intake}$=0.50 bar and SA 12 CAD*

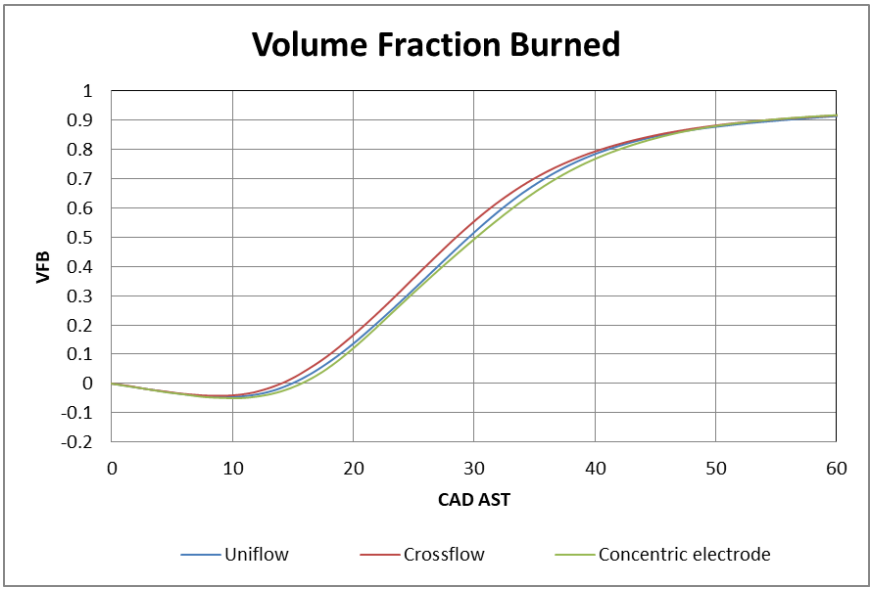


*Figure 4.45, VFB traces for $P_{intake}$=0.75 bar and SA 12 CAD*

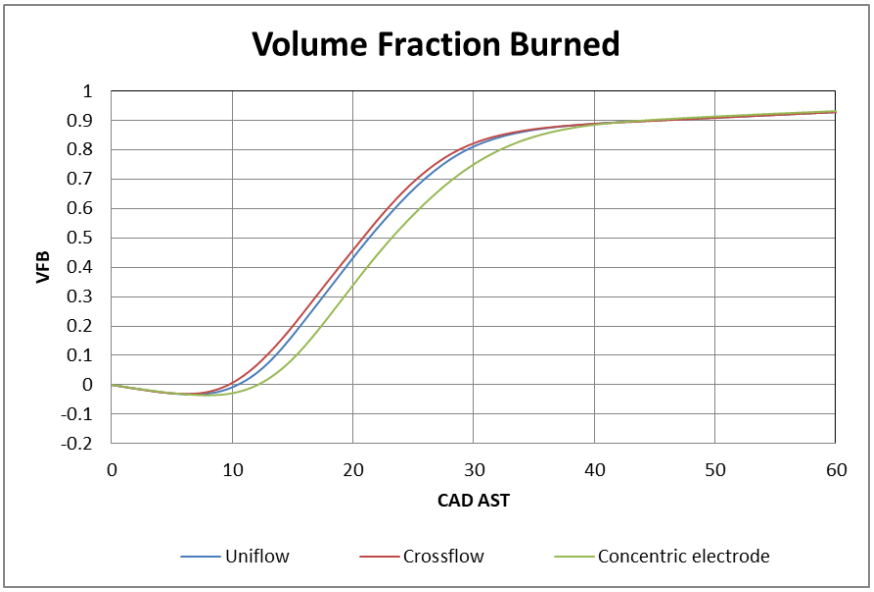


*Figure 4.46, VFB traces for $P_{intake}$=1.00 bar and SA 12 CAD*

Interesting results in terms of kernel displacement along the x and y axes are shown in the figures 4.47-4.48 respectively. Starting from the analysis of Dx, it can be seen that, for the uniflow configuration, the trend is decreasing as the intake pressure increases, unlike the crossflow and concentric electrode geometries, both of which show an almost constant trend in the passage from 0.50 to 0.75 bar (negative x-axis displacement values under these load conditions) and increasing in the subsequent rise of $P_{intake}$ to 1.00 bar. Regarding Dy, there are similar decreasing trends for uniflow and crossflow, the latter exhibiting higher and all positive values.

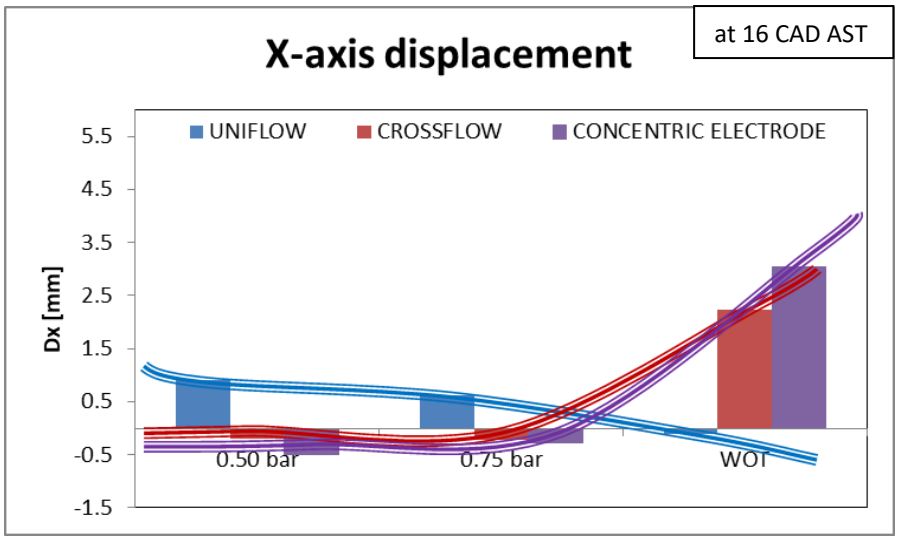


*Figure 4.47, X-axis displacement values for the $P_{intake}$ sweep, SA 12 CAD*

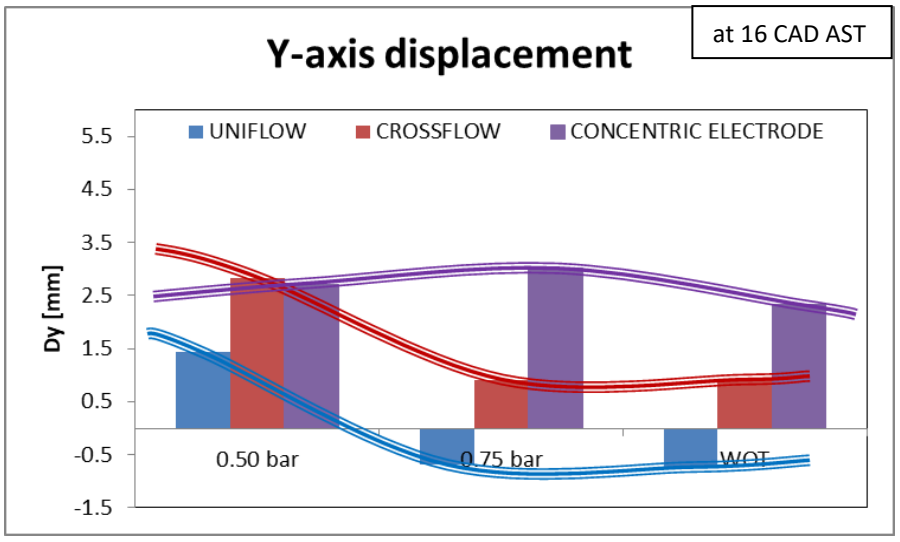


*Figure 4.48, Y-axis displacement values for the $P_{intake}$ sweep, SA 12 CAD*

Finally, in terms of flame expansion speed (figure 4.49), increasing trends can be seen for uniflow and concentric electrode spark plug as engine load increases, while crossflow shows a peak value at $P_{intake}$=0.75 bar.

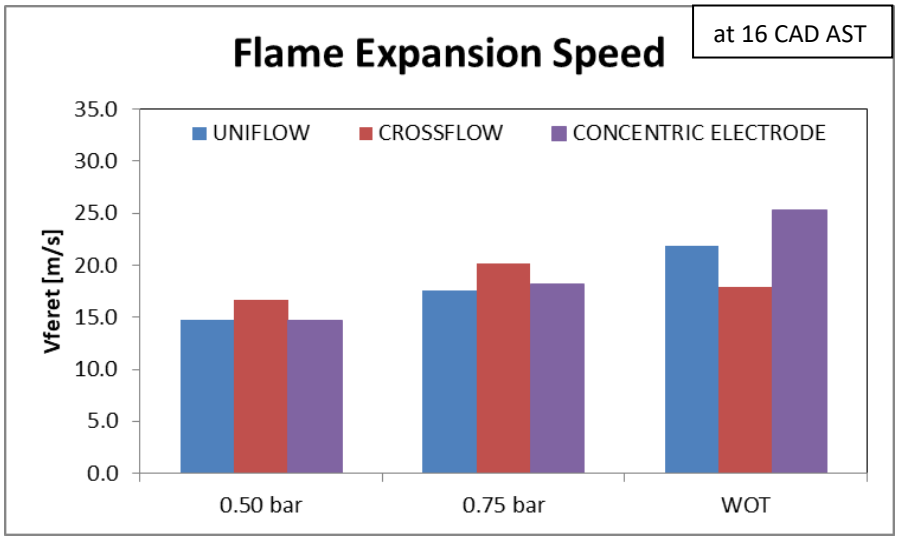


*Figure 4.49, Flame expansion speed values for the $P_{intake}$ sweep, SA 12 CAD*

### 4.5.2 Effect of Engine Load for Variable SA

In this part of the study, the combined effect of a reduced engine load ($P_{intake}$=0.50 bar) and Spark Advance, varied between 12 and 24 CAD, was analysed. Looking at the in-cylinder pressure cycles shown in the figures 4.49-4.50, what stands out is the peak pressure increase, characteristic of each configuration, which follows the ignition advance increment. Furthermore, an evident gap can be observed between the concentric electrode configuration and the other two (peak values of approximately 16.5 and 18 bar respectively) for the most anticipated spark ignition event condition.

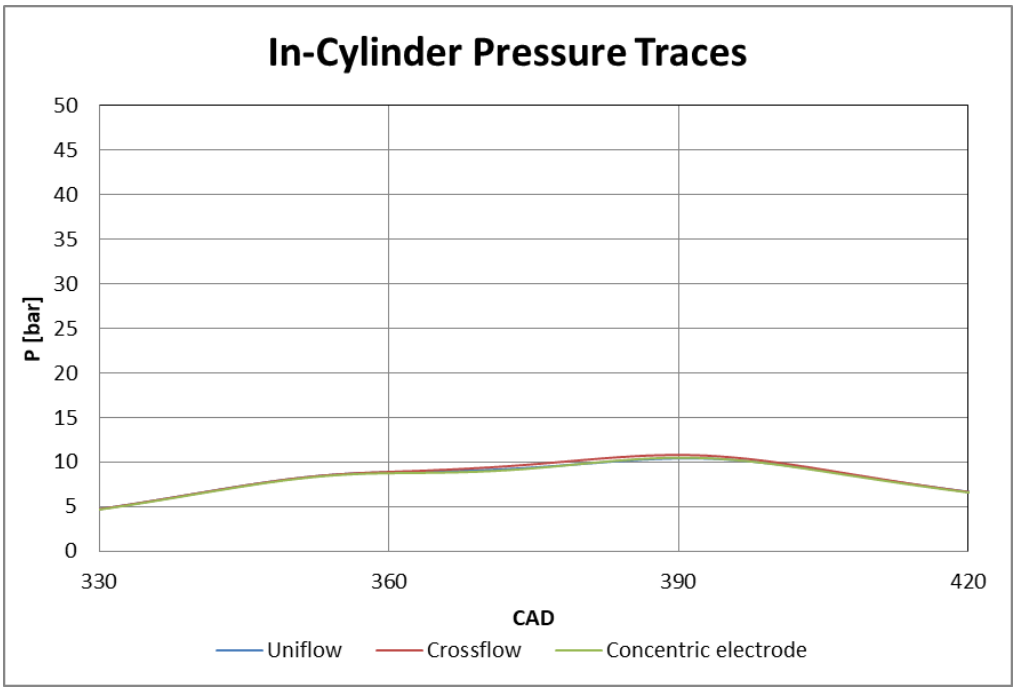


*Figure 4.49, In-cylinder Pressure traces for $P_{intake}$=0.50 bar and SA 12 CAD*

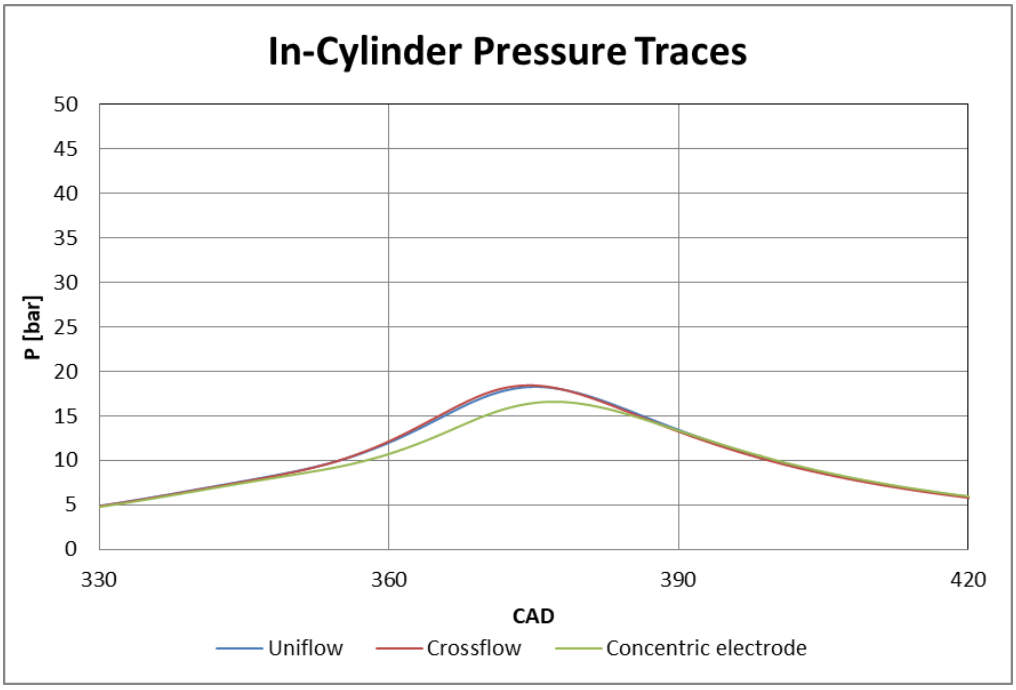


*Figure 4.50, In-cylinder Pressure traces for $P_{intake}$=0.50 bar and SA 24 CAD*

Observing the figure 4.51, comparable IMEP values both in terms of configuration and SA can be noted; indeed, in each analysed case indicated mean effective pressure levels around 3 bar are reported. A different situation occurs in terms of $COV_{IMEP}$, whereby a reduction is observed as the ignition advance increases. For SA 12 CAD, minimum and maximum values respectively for crossflow and concentric electrode configuration are noted (about 5.5% and 10%, correspondingly); by increasing advance of 12 CAD, the three geometries assume comparable $COV_{IMEP}$ values around 2.4%.

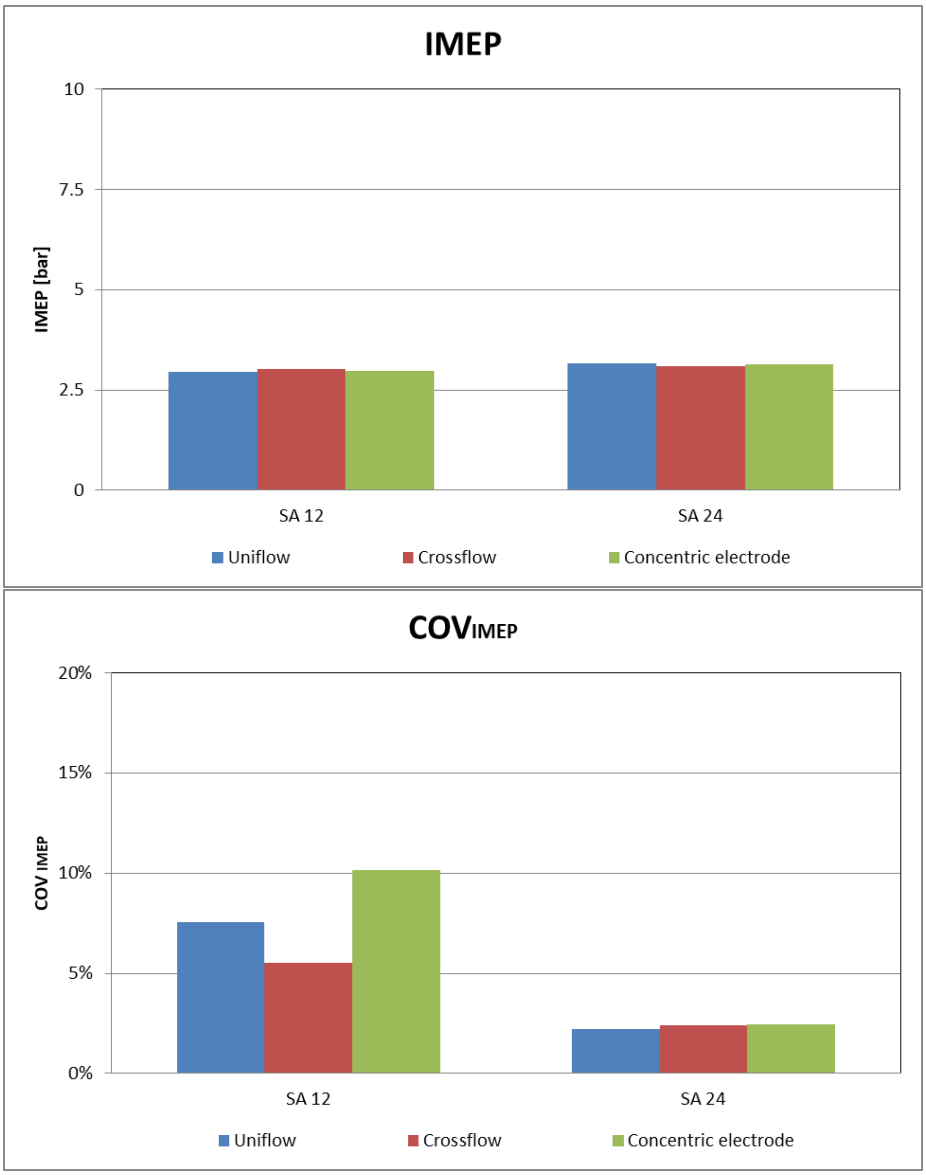


*Figure 4.51, IMEP and $COV_{IMEP}$ values for the Spark Advance sweep, $P_{intake}$=0.50 bar*

From the analysis of average maximum pressure and $COV_{Pmax}$ (figure 4.52), it is possible to understand the reasons leading to the above-mentioned gap between in-cylinder pressure cycles for SA 24 CAD. In fact, as can be seen, the concentric electrode configuration presents a reduced $P_{max}$ value compared with the other two ignition geometries (17.5 bar against about 19 bar) and a higher $COV_{Pmax}$ value (11% compared to around 8% for uniflow and crossflow). Conversely, for the less advanced ignition

condition, there is good comparability in these terms among the various spark plug settings, although concentric electrode one exhibits higher $COV_{Pmax}$.

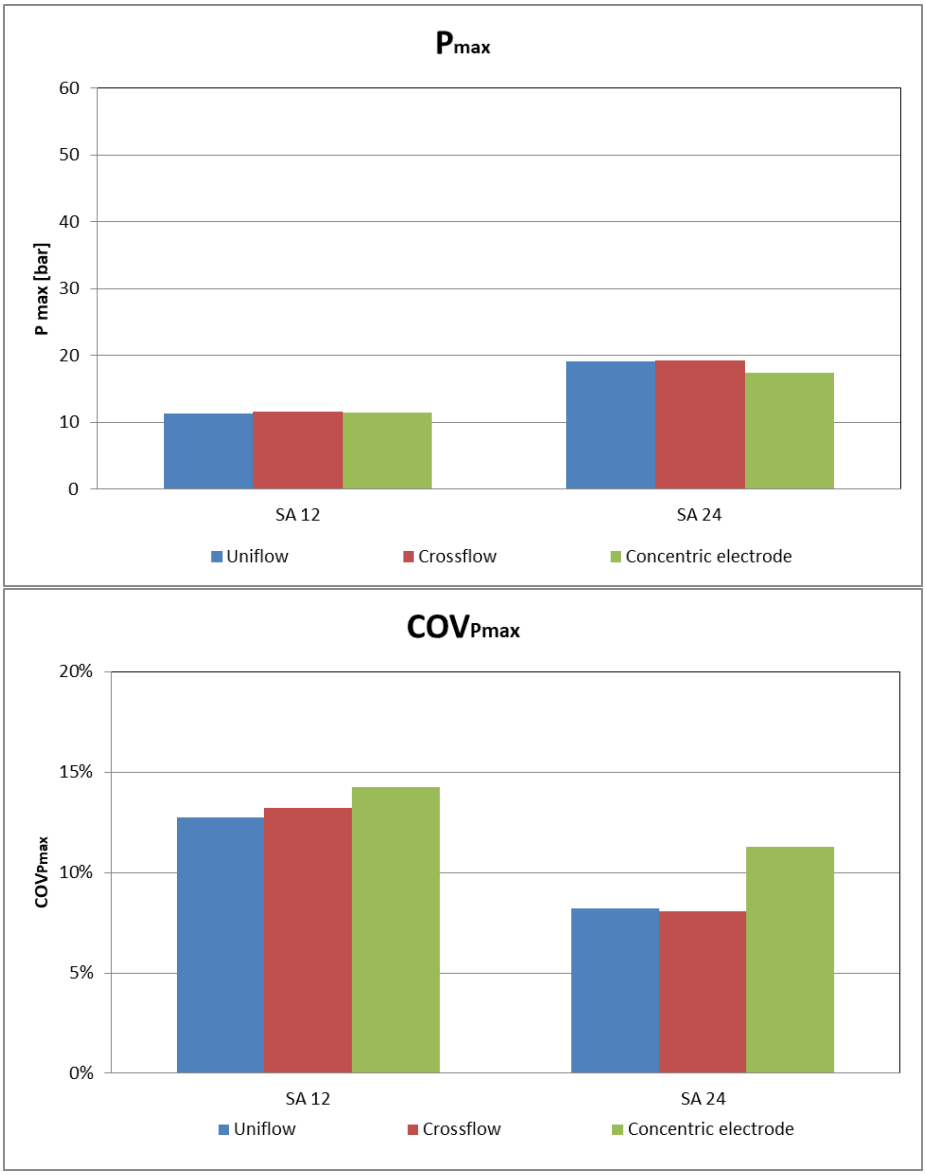


*Figure 4.52, Maximum pressure and $COV_{Pmax}$ values for the Spark Advance sweep, $P_{intake}$=0.50 bar*

As seen in the previous sub-section, the most rapid evolution in terms of VFB, for $P_{intake}$=0.50 bar and SA 12 CAD, is that characteristic of the concentric electrode spark plug. From figure 4.54 it is possible to see a reversed trend, with faster combustions for uniflow and crossflow orientations (with a gap of 3-4 CAD from the concentric configuration, concerning the achievement of $VFB_{80\%}$).

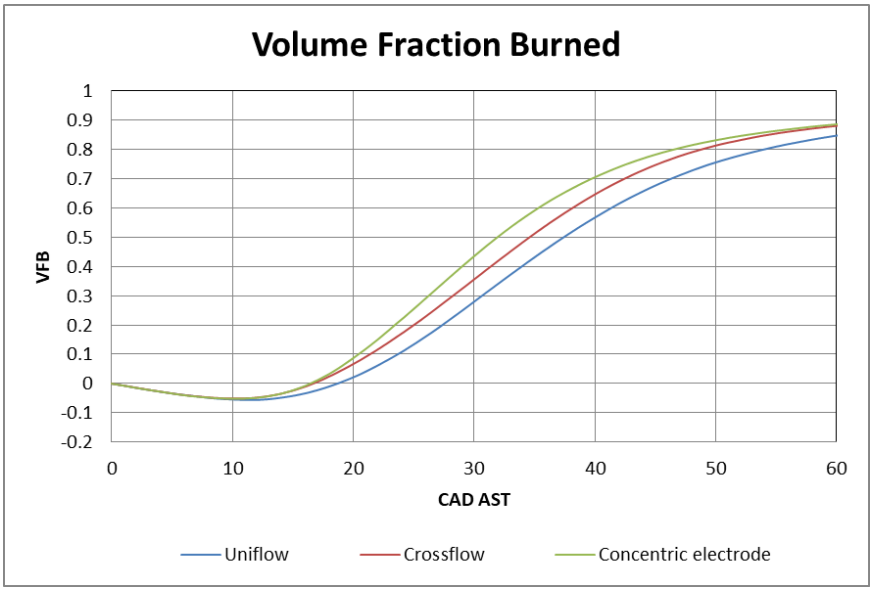


*Figure 4.53, VFB traces for $P_{intake}$=0.50 bar and SA 12 CAD*

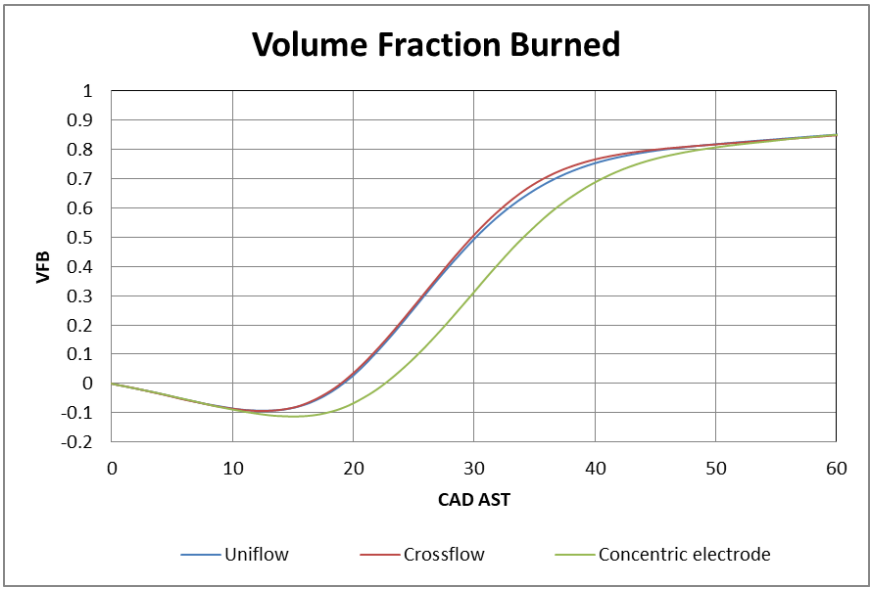


*Figure 4.54, VFB traces for $P_{intake}$=0.50 bar and SA 24 CAD*

In terms of flame kernel displacement, it can be seen from figure 4.55 that for each ignition configuration and as the Spark Advance increases, Dx shows a decreasing trend, unlike Dy which looks increasing and whose higher values have a greater influence on the kernel dislocation R (figure 4.56), giving the latter the same trend. Finally, $V_{Feret}$ analysed in figure 4.57 remains almost constant for the uniflow and concentric electrode configurations, while it tends to slightly increase for the crossflow, passing from SA 12 CAD to SA 24 CAD.

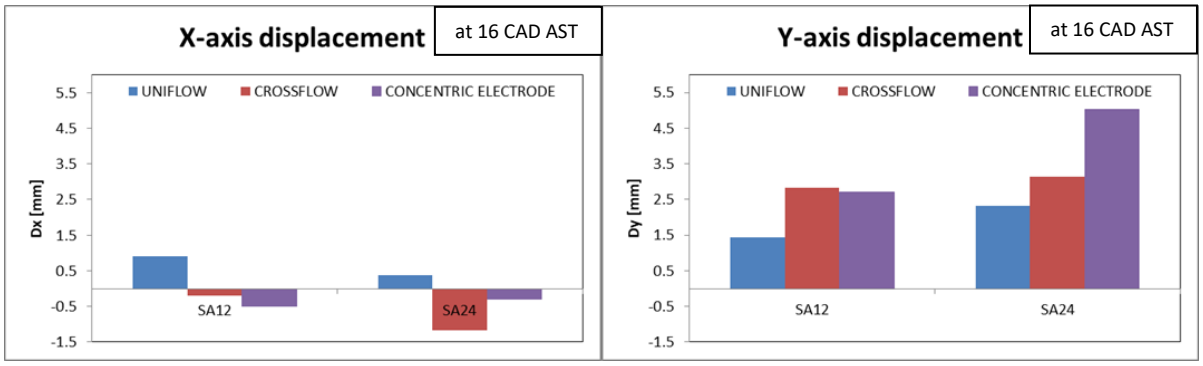


*Figure 4.55, X- and Y-axis displacements values for the Spark Advance sweep, $P_{intake}$=0.50 bar*

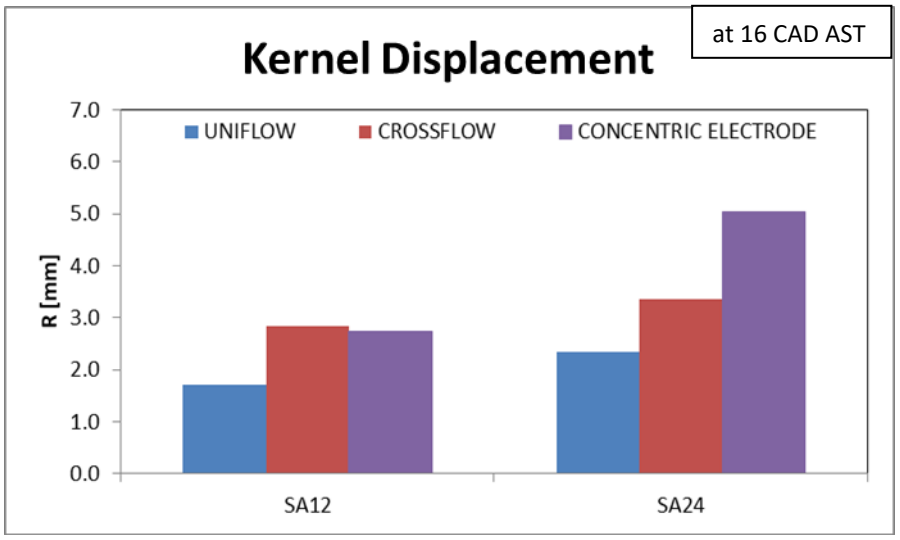


*Figure 4.56, Kernel displacement values for the Spark Advance sweep, $P_{intake}$=0.50 bar*

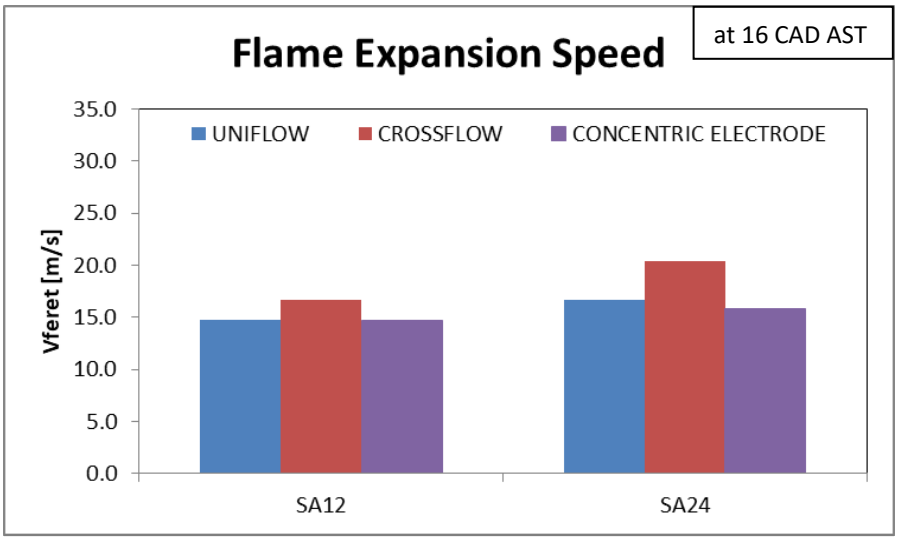


*Figure 4.57, Flame expansion speed values for the Spark Advance sweep, $P_{intake}$=0.50 bar*

## 4.6Effect of Engine Speed

The influence of engine speed is particularly important as this parameter tends to influence the levels of turbulence intensity in the combustion chamber and thus flame front propagation as well as residence time. Regulating the electrical motor speed with a feedback control loop capable of switching between motor – generator regimes, the rotation speed has been varied between two different levels of 1000 and 2000 rpm respectively. Stoichiometric AFR has been maintained by adjusting the DOI according to the duration of intake stroke and therefore the amount of suctioned air for each of the two analysed cases (DOI 19 for n=1000 rpm, DOI 39 for n=2000 rpm); finally, Spark Advance has been set at 12 CAD. Average pressure cycles are shown in the figures 4.58-4.59. A well-defined trend can be seen for the three ignition configurations as n varies: the crossflow and concentric electrode geometries exhibit the highest and lowest pressure levels and peaks, correspondingly. However, for each configuration, the increase in engine speed does not lead to significant variations in terms of maximum pressures (about 38 bar for crossflow, 37 bar for uniflow and 35 bar for concentric electrode spark plug) and gap (around 2-3 bar).

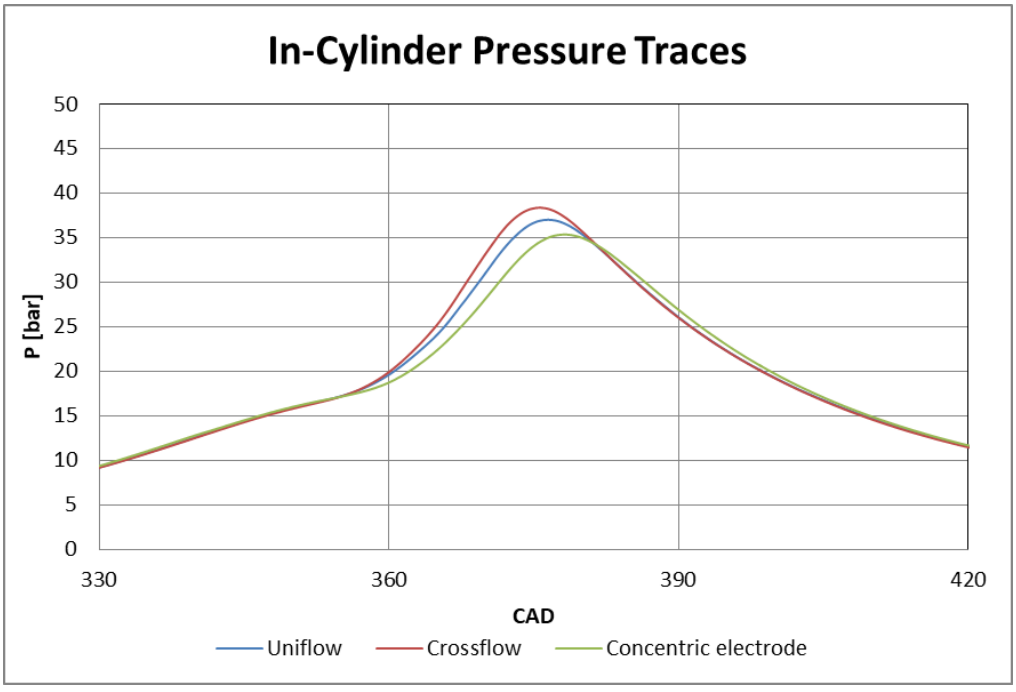


*Figure 4.58, In-cylinder Pressure traces for n=1000 rpm and SA 12 CAD*

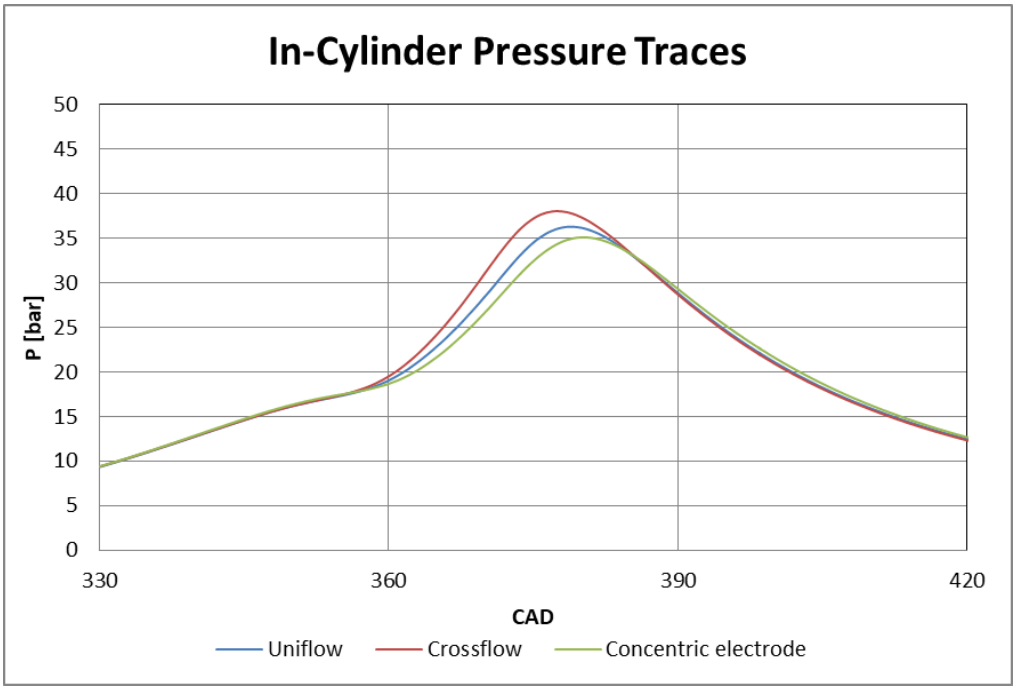


*Figure 4.59, In-cylinder Pressure traces for n=2000 rpm and SA 12 CAD*

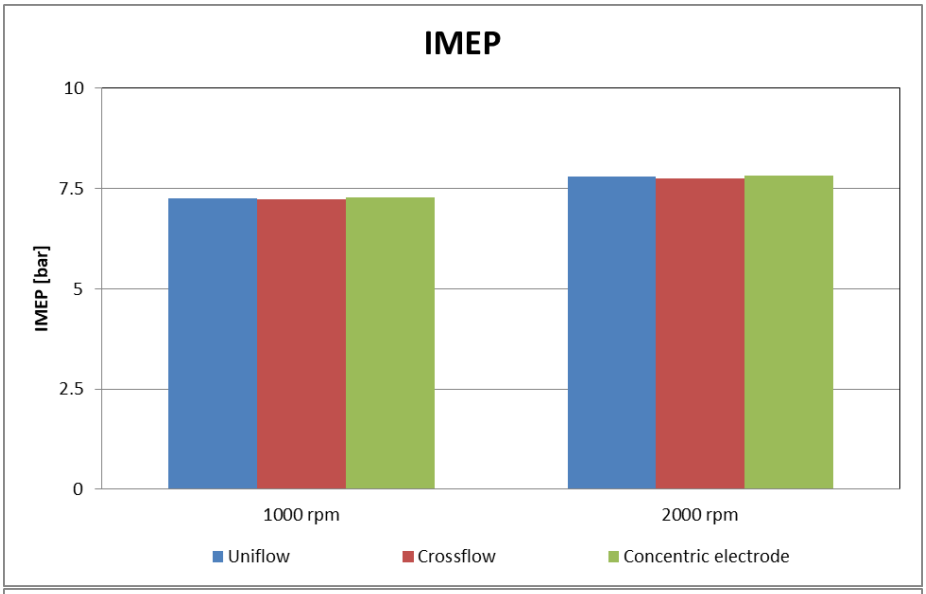


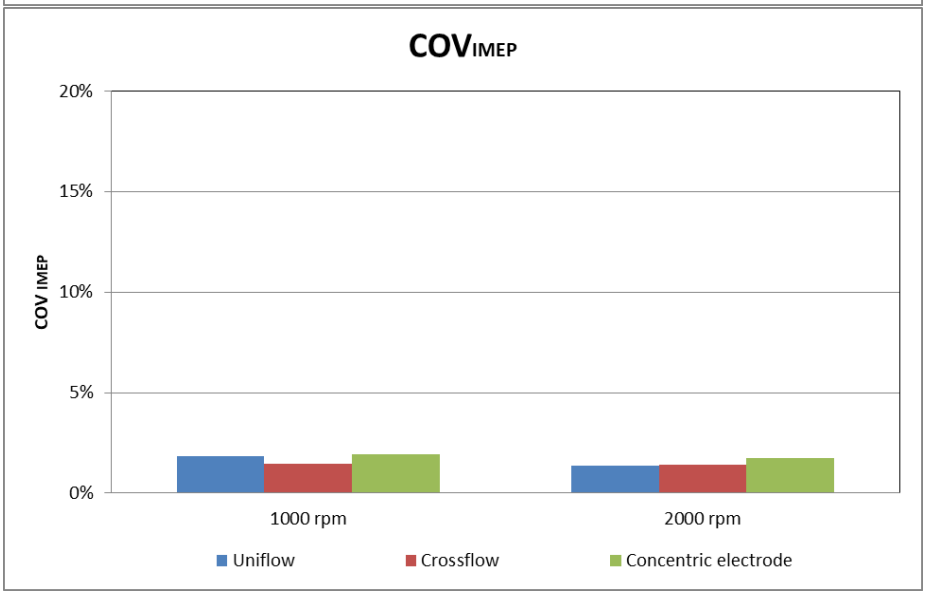


*Figure 4.60, IMEP and $COV_{IMEP}$ values for the engine speed sweep, SA 12 CAD*

The above findings are also confirmed by the figure 4.60, in which the IMEP and respective $COV_{IMEP}$ values are shown. First of all, it can be seen that the three spark plug geometries have comparable IMEP values for constant n, while the increase of this latter parameter leads to slight increments of about 0.5 bar. The cyclic variability percentage tends to reduce as the rotation speed increases, with values that are nevertheless comparable and contained (fewer than 2%) varying both spark plug and speed settings. Moving on to $P_{max}$ and $COV_{Pmax}$ analysis (figure 4.61), it can be seen that, doubling engine speed, the average maximum pressure remains, with good approximation, constant for each ignition configuration with the exception of crossflow orientation for which a slight decrease can be observed (from about 39 bar at 1000 rpm to 37.5 bar at 2000 rpm). This last configuration is however characterised by higher values compared to the others (around 37 and 36 bar for uniflow and concentric electrode configuration, respectively).

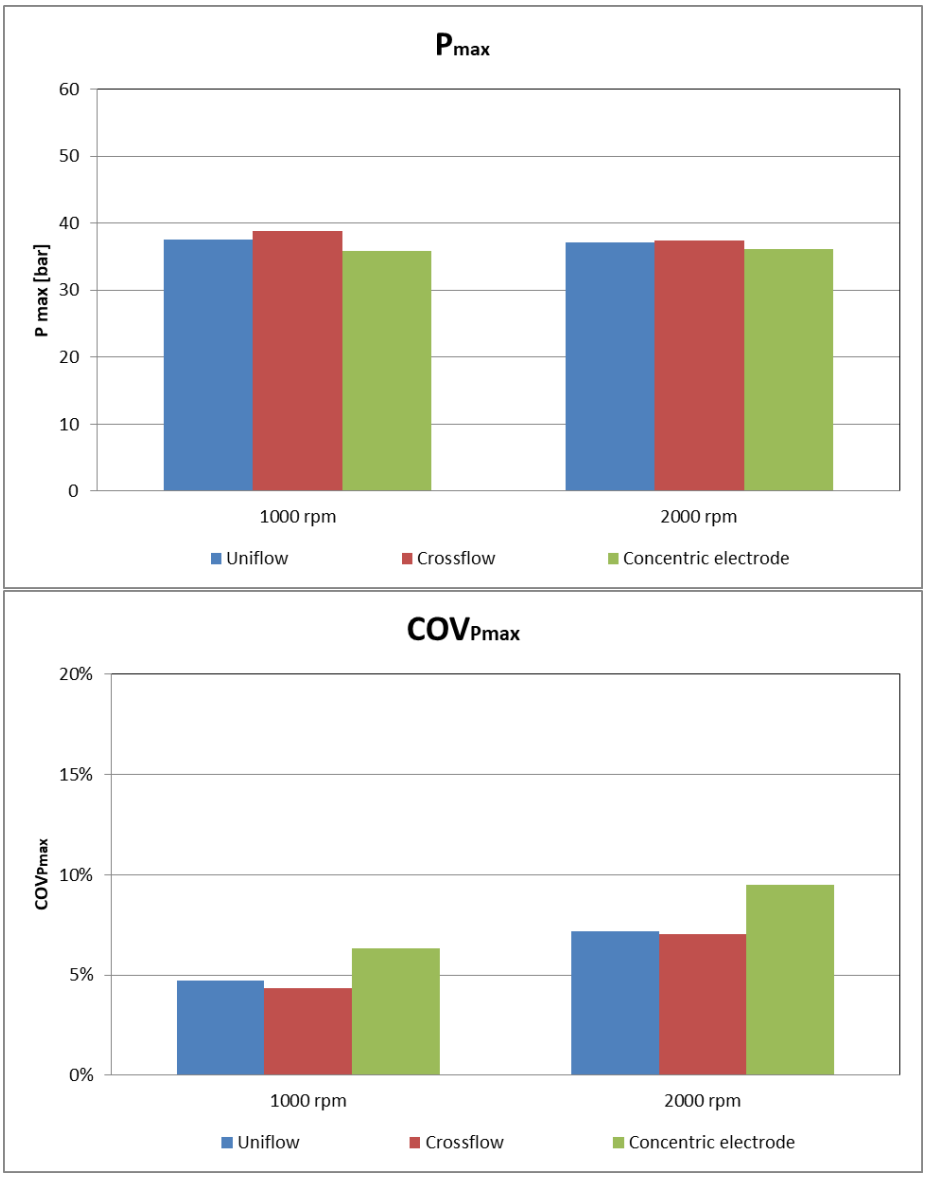


*Figure 4.61, Maximum pressure and $COV_{Pmax}$ values for the engine speed sweep, SA 12 CAD*

Unlike $COV_{IMEP}$, the coefficient of variation of $P_{max}$ tends to increase with rotation speed, with the concentric geometry exhibiting higher levels (from 6.3% to 9.5 %) than uniflow and crossflow. The latter look comparable, although the second one shows the lowest $COV_{Pmax}$ (4.3% and 7% correspondingly).

Looking at the VFB traces in the figures 4.62-4.63, it can be seen that the concentric electrode configuration is characterised by the slowest evolution of the combustion process, as n varies. In terms of $VFB_{80\%}$, uniflow and crossflow achieve this condition at around 26 and 29-30 CAD AST, for engine speeds of 1000 and 2000 rpm respectively, with the concentric electrode spark plug exhibiting a gap of approximately 2 CAD.

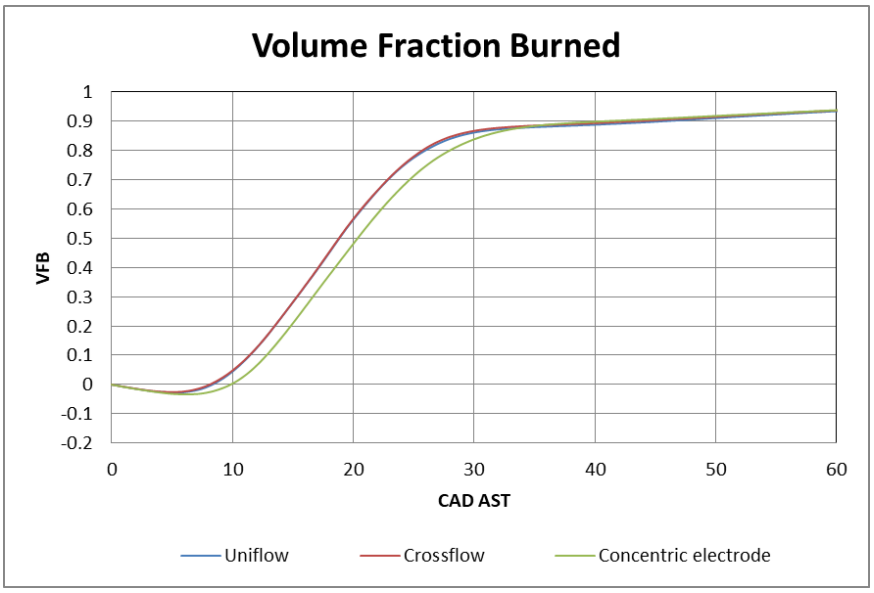


*Figure 4.62, VFB traces for n=1000 rpm and SA 12 CAD*

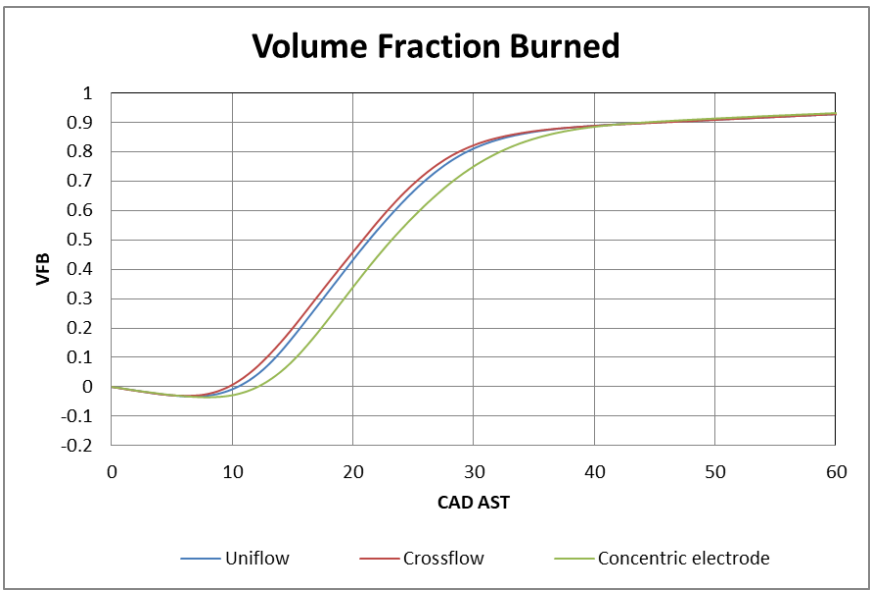


*Figure 4.63, VFB traces for n=2000 rpm and SA 12 CAD*

Observing the flame area displacement plots, from figure 4.64, opposite trends of Dx and Dy as n increases are noted for uniflow and crossflow orientations; this situation results in the same trend in terms of the resulting R (figure 4.65, slightly decreasing for uniflow and

increasing for crossflow). The concentric electrode configuration exhibits a more pronounced increasing trend in Dx, with a constant Dy; this leads to increasing kernel displacement trend and therefore more influenced by the dislocation along the x-axis. Finally, for the three different geometries, there is an increment in terms of flame expansion speed (figure 4.66). This latter seems to be more prominent for uniflow and concentric electrode configurations.

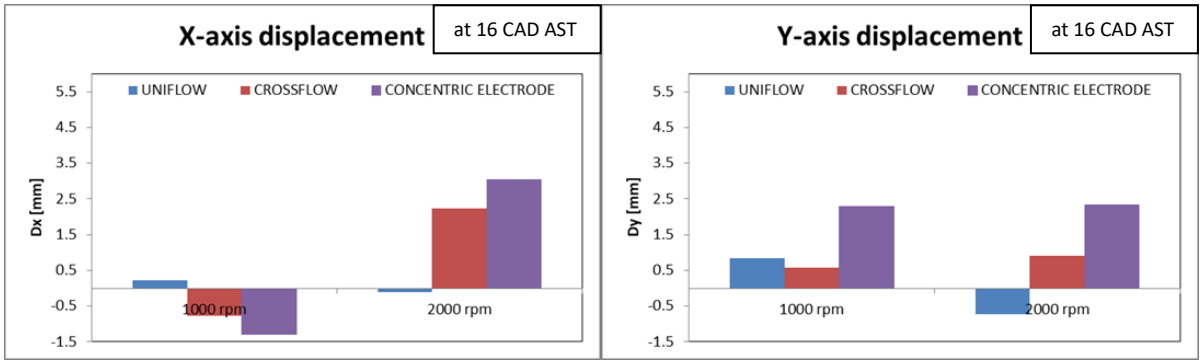


*Figure 4.64, X- and Y-axis displacements values for the engine speed sweep, SA 12 CAD*

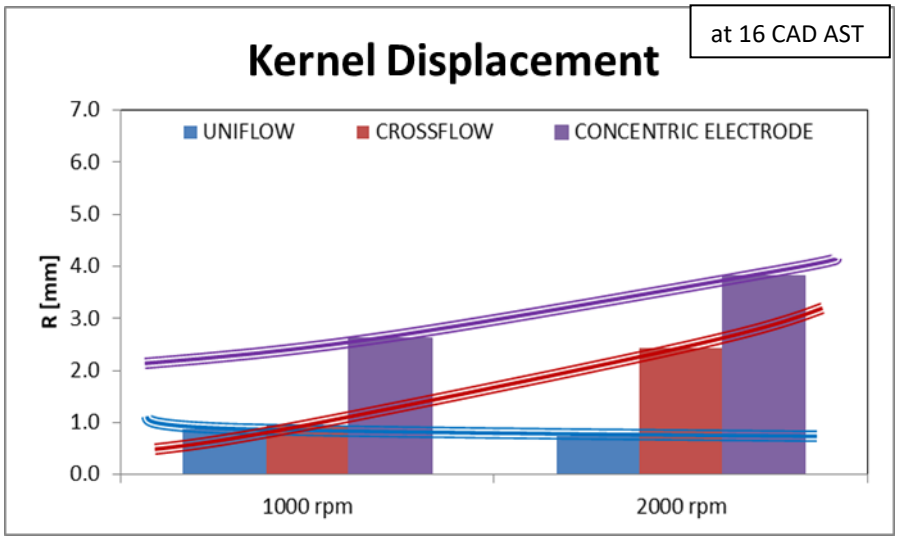


*Figure 4.65, Kernel displacement values for the engine speed sweep, SA 12 CAD*

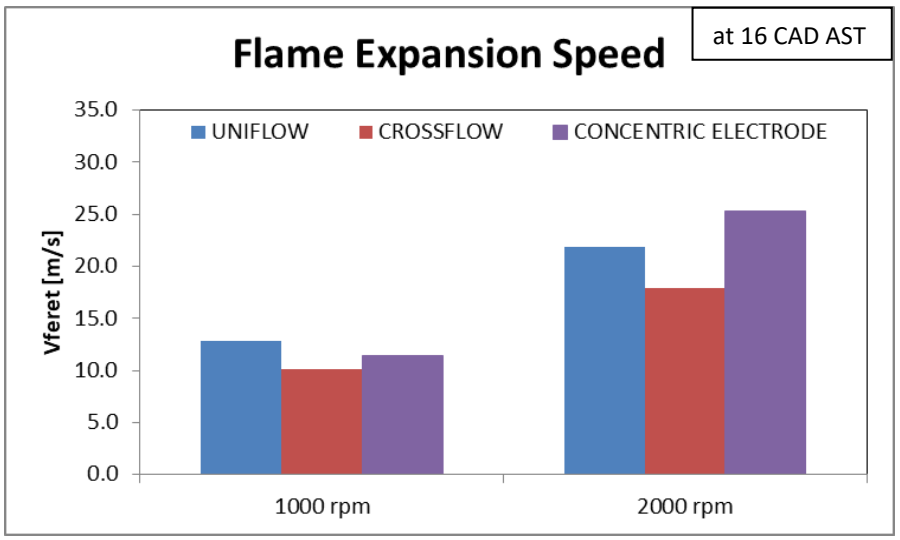


*Figure 4.66, Flame expansion speed values for the engine speed sweep, SA 12 CAD*

# Conclusive remarks

As previously mentioned, the target of the current thesis work was to examine the flame-fluid interaction during combustion process for different operating conditions and to provide a database with information on CCV phenomena, kernel dislocation and flame front propagation speed. The main conclusions are the following:

- For a fixed Air-Fuel Ratio set to λ=1.15 and variable SA, the concentric electrode geometry showed the slowest flame front propagation; in fact the latter achieves the MBT condition for a Spark Advance of 20 CAD, while for the other two configurations it is obtained for a SA of 16 CAD. Optical data show a spatial development of the flame kernel with opposite trends between uniflow and crossflow configurations, indicating an influence of orientation on flame-fluid interaction. Concentric configuration has registered the largest radial kernel displacement with respect to the spark plug center.
- For a fixed Air-Fuel Ratio at λ=1.30, the crossflow and concentric electrode configurations seem to show a peak in terms of engine performance (Higher value of IMEP and lower $COV_{IMEP}$) for ST 20 CAD BTDC. The optical analysis confirms an effect of spark plug geometry on combustion phenomena.
- For a fixed Spark Advance set to 12 CAD and variable AFR, the crossflow configuration seems to features, for each Air-Fuel Ratio, higher pressure peaks, followed by the uniflow orientation and finally the concentric electrode spark plug configuration, which achieves the most contained pressure levels and the slowest combustion evolution among the three ignition geometries. In optical terms, results again show a countertrend between uniflow and crossflow as regards flame kernel displacement.
- For a fixed Spark Advance at 20 CAD, the most efficient engine performance (Higher value of IMEP and Pmax with lower cycle-to-cycle variability) is exhibited by the crossflow configuration. Results from the optical analysis show increasing kernel dislocation trends for the crossflow and concentric electrode configurations, with the latter having a steeper slope. In contrast, uniflow presents declining but almost comparable values as the AFR varies. An increase in flame speed due to mixture enrichment is also recorded, but the levels achieved are comparable between the various configurations.
- For a fixed Spark Advance set to 12 CAD and variable $P_{intake}$, the crossflow orientation remains the most efficient in thermodynamic terms, while a strong influence of the engine load on the evolution of combustion is noted for the concentric electrode spark plug. Uniflow and crossflow show opposite trends in terms

of displacement along the horizontal axis (Dx) and concordant trends on the vertical axis (Dy).

- For a fixed $P_{intake}$ set to 0.50 bar and variable SA, the three ignition configurations achieve the MBT condition for SA 24 CAD with comparable values. However, in terms of $COV_{Pmax}$ and VFB, the concentric electrode geometry is slightly disadvantaged. In terms of flame displacement, for spark plug setting and as the Spark Advance increases, kernel dislocation R shows a decreasing trend strongly influenced by Dy. The flame expansion speed tends to grow for crossflow, varying SA from 12 to 24 CAD.
- For a fixed Spark Advance set to 12 CAD and variable n, the concentric electrode configuration is characterised by minimum pressure peaks among the three ignition geometries, unlike crossflow which exhibits higher in-cylinder pressure levels. However, in terms of IMEP and $COV_{IMEP}$, the values recorded are comparable varying both spark plug and speed settings. Opposite trends of Dx and Dy as n increases are noted for uniflow and crossflow orientations. The concentric electrode configuration exhibits a more pronounced increasing trend in Dx, with a constant Dy; this leads to increasing kernel displacement trend and therefore more influenced by the dislocation along the x-axis. Finally, there is an increment in terms of flame expansion speed, more noticeable for uniflow and concentric electrode configurations.

The results obtained are particularly interesting with regard to future analysis of flame-fluid interactions in a GDI engine. The crossflow and uniflow configurations always exhibited opposite behavior in terms of optical results, while the concentric electrode geometry shows similar but more pronounced trend than crossflow. This orientation certainly requires more in-depth studies to improve and validate the results just obtained.

# References


1. Soat R., ICE Bans Begin to Take Shape in the US, Forbes, 2020 https://www.forbes.com/sites/pikeresearch/2020/11/04/ice-bans-begin-to-take-shape-in-the-us/?sh=bd3b91c3e178.
2. British Petroleum, Statistical Review of World Energy 2021 | 70th edition, British Petroleum https://www.bp.com/content/dam/bp/business-sites/en/global/corporate/pdfs/energy-economics/statistical-review/bp-stats-review-2021-full-report.pdf.
3. IEA Oil - Fuels & Technologies, Global Oil Demand Shifts Lower After Historic Collapse, IEA, 2021
4. Automotive from UltimaMedia, Automotive Powertrain Forecast 2020-2030, Automotive from UltimaMedia, 2019 https://www.automotivelogistics.media/download?ac=283785.
5. European Environment Agency (online data code: env_air_gge).
6. Avery K., Electric Vehicles Drive Up Metals Demand, Visual Capitalist Charted: Electric Vehicles Drive up Metals Demand, 2021 visualcapitalist.com.
7. Yang J., Kenney T., Some Concepts of DISI Engine for High Fuel Efficiency and Low Emissions, SAE International, 2002
8. Midterm Evaluation of Light-Duty Vehicle Greenhouse Gas Emission Standards and Corporate Average Fuel Economy Standards for Model Year 2022-2025, Draft Technical Assessment Report, Office of Transportation and Air Quality, United States Environmental Protection Agency, 2016 https://nepis.epa.gov/Exe/ZyPDF.cgi/P100OXEO.PDF?Dockey=P100OXEO.PDF.
9. Lee Z. et al. , Review on Spray, Combustion, and Emission Characteristics of Recent Developed Direct-Injection Spark Ignition (DISI) Engine System with Multi-Hole Type Injector, Fuel, 2020.
10. Yang J., Anderson R.W., Fuel Injection Strategies to Increase Full-Load Torque Output of a Direct-Injection SI Engine, SAE International, 1998
11. Karmann S.B., Prager M., Wachtmeister G., Conceptual Investigations on Full Optical Accessibility to Large-Bore Medium-Speed Engines, SAE International, 2019
12. Miles P.C., The History and Evolution of Optically Accessible Research Engines, Sandia National Laboratories, 2014
13. Bowditch F.W., A New Tool for Combustion Research A Quartz Piston Engine, SAE International, 1961

14. Ozdor N., Dulger M., Sher E., Cyclic Variability in Spark Ignition Engines, SAE International, 1994
15. Heywood J.B., Internal Combustion Engine Fundamentals, McGraw Hill, 1988
16. Falkenstein T. et al., DNS Study of the Global Heat Release Rate During Early Flame Kernel Development Under Engine Conditions, Combustion and Flame, 2020
17. Sjeric M., Kozarac D., Tatschl R., Modelling of Early Flame Kernel Growth Towards a Better Understanding of Cyclic Combustion Variability in SI Engines, Energy Conversion and Management, 2015
18. Holmström K., Denbratt I., Cyclic Variation in an SI Engine due to the Random Motion of Flame Kernel, SAE International, 1996 http://dx.doi.org/10.4271/961152
19. Stone C.R., Brown A.G., Beckwith P., Cycle-by-cycle Variations in Spark Ignition Engine Combustion – Part II: Modelling of Flame Kernel Displacement as a Cause of Cycle-by-cycle Variations, SAE International, 1996 http://dx.doi.org/10.4271/960613
20. Wang Y. et al., Investigation of Impacts of Spark Plug Orientation on Early Flame Development and Combustion in a DI Optical Engine, SAE International, 2017
21. Schirru A. et al., Flame Kernel Growth and Related Effects of Spark Plug Electrodes – Fluid Motion Interaction in an Optically Accessible DISI Engine, World Academy of Science, Engineering and Technology International Journal of Mechanical and Mechatronics Engineering, 2020
22. Irimescu A., Merola S.S., Martinez S., Influence of Engine Speed and Injection Phasing on Lean Combustion for Different Dilution Rates in an Optically Accessible Wall-Guided Spark Ignition Engine, SAE International, 2018
23. Aleiferis P.G. et al., Flame Chemiluminescence Studies of Cyclic Combustion Variations and Air-to-Fuel Ratio of the Reacting Mixture in a Lean-Burn Stratified-Charge Spark Ignition Engine, Combustion and Flame, 2004
24. Johansson A.N., Hemdal S., Dahlander P., Experimental Investigation of Soot in a Spray-Guided Single Cylinder GDI Engine Operating in a Stratified Mode, SAE International, 2013
25. Serras-Pereira J. et al., Spray Development, Flow Interactions and Wall Impingement in a Direct-Injection Spark-Ignition Engine, SAE International, 2007
26. Han Z. et al. Effects of Injection Timing on Air-Fuel Mixing in a Direct-Injection Spark-Ignition Engine, SAE International, 1997
27. Serras-Pereira J., Aleiferis P., Richardson D., Imaging and Heat Flux Measurements of Wall Impinging Sprays of Hydrocarbons and Alcohols in a Direct-Injection Spark-Ignition Engine, Fuel, 2012
28. Celik M.B., Ozdalyan B., Gasoline direct injection, InTechOpen, 2010
29. Eni S.p.A., Refining & Marketing and Chemicals "Benzina RON 95 E10"

30. Irimescu A., Back-Pressure and Fuel Type Effects on Exhaust Gas Oxygen Sensor Readings for a Single Cylinder Spark Ignition Engine Running on Gasoline and Ethanol, SAE International, 2019
31. AVL DiTEST GmbH, User Manual AVL DITEST GAS 1000
32. Irimescu A., Vasiu G., Trif Tordai G., Performance and Emissions of a Small Scale Generator Powered by a Spark Ignition Engine with Adaptive Fuel Injection Control, Applied Energy, 2014
33. Martinez S., Merola S.S., Irimescu A., Flame Front and Burned Gas Characteristics for Different Split Injection Ratios and Phasing in an Optical GDI Engine, Applied Sciences, MDPI, 2019
34. Optronis GmbH, Optronis Hight-Speed Video Camera, Adept Electronic Solutions
35. Cecere G., Visualization of Flame-Fluid Interactions and Influence on Kernel Growth in a DISI Engine, Politecnico di Torino, 2021
36. Clasen K., Koopmans L., Investigation of Homogeneous Lean SI Combustion in High Load Operating Conditions, SAE International, 2020